# Dynamics in strongly interacting one-dimensional quantum systems

Rafael Emilio Barfknecht



Institute of Physics
Federal University of Rio Grande do Sul
Brazil

Institute of Physics and Astronomy
Aarhus University
Denmark

# Dynamics in strongly interacting one-dimensional quantum systems

A PhD Thesis presented at the Institute of Physics of the Federal University of Rio Grande de Sul in partial fulfillment of the requirements for the PhD degree in physics.
The work presented here has been performed in the period of June 2015 to February 2019 under the supervision of Angela Foerster at the Federal University of Rio Grande do Sul, and Nikolaj Thomas Zinner at Aarhus University.

by
Rafael Emilio Barfknecht

# Abstract

In this thesis we study the dynamics of one-dimensional strongly interacting few-body systems. We present the theory which allows us to describe such systems as a spin chain where the exchange coefficients are determined by the trapping geometry, and comment on the experimental feasibility of these models. We then proceed to apply our formalism to different dynamical problems, where the strength of the interactions between the atoms in the trap plays a fundamental role. We find that interesting effects - ranging from changes in magnetic correlations to impurity oscillations and spin-charge separation - arise in this context. Additionally, we perform studies of the static correlations and many-body dynamics of bosonic systems away from the strongly interacting limit.

# Resumo

Nesta tese estudamos a dinâmica de sistemas unidimensionais de poucas partículas com interações fortes. Apresentamos uma teoria que nos permite descrever esses sistemas como uma cadeia de spin, na qual os coeficientes de troca são determinados pela geometria de aprisionamento, e comentamos sobre a viabilidade experimental desses modelos. Então aplicamos este formalismo para diferentes problemas dinâmicos, onde a força das interações entre os átomos na armadilha tem um papel fundamental. Notamos que efeitos interessantes - desde mudanças nas correlações magnéticas até oscilações de impureza e separação de carga e spin - surgem nesse contexto. Adicionalmente, realizamos estudos de correlações estáticas e dinâmicas de muitos corpos de sistemas bosônicos fora do limite de interações fortes.

# Resumé

I denne afhandling studerer vi dynamikken af en-dimensionelle stærkt interagerende få-legeme systemer. Vi præsenterer teorien, som tillader os at beskrive sådant et system som en spinkæde, hvor vekselvirkningskoefficienterne er bestemt af fældens geometri, og vi kommenterer på den eksperimentelle gennemførlighed af disse modeller. Dernæst anvender vi vores formalisme på forskellige dynamiske problemer, hvor styrken af interaktionen mellem atomerne i fælden spiller en fundamental rolle. Vi finder at interessante effekter – som spænder fra ændringer i magnetiske korrelationer til urene svingninger og spin-ladning separation – opstår i denne kontekst. Derudover udfører vi studier af den statistiske korrelation og mange-legeme dynamikker af bosoniske systemer væk fra den stærkt interagerende grænse.

# Acknowledgments

When I signed up for the PhD program at UFRGS I did not expect that, at the end of four years, it would have accomplished as much as I have. This is not to say that I did not have any ambition as I started, but publishing papers in recognized scientific journals, establishing international collaborations and traveling to conferences around the world was a little beyond my expectations. And while I am sure I worked hard to achieve this, I only did it because of the great people that I had a chance to work with and learn from.

First of all, I want to thank my PhD advisers, prof. Angela Foerster and prof. Nikolaj Thomas Zinner. With Angela I learned how to do research when she first accepted me as a Master's student a while ago. Looking back, I can say this was definitely a turning point in my career. Without her guidance and experience, none of what came afterwards would have been possible. I feel extremely lucky to have had such a talented and understanding person as my supervisor in the last six years. Nikolaj, even as I was starting my PhD, offered me the great opportunity of working at Aarhus University, which to me truly meant an enormous step forward. He has always encouraged me to trust my own work, and from our interaction I learned a lot about what it means to be a researcher these days. To both of my supervisors I am extremely thankful.

Next I must acknowledge the people I have collaborated and learned from during this period, some of which have become true friends along the way. I had the pleasure of working with extremely capable researchers at Aarhus University, such as Amin Salami Dehkharghani and Stig Elkjaer Rasmussen, whose collaboration ended up with the production of papers. I also thank Jonathan Lindgren for sharing his work with me, and Marcos Pérez, David Carvalho and Karin Wilsmann at UFRGS for several interesting discussions (and for the good times in general).

A big thank-you goes to all of my friends at the Physics Intitute at UFRGS, some of which have followed different paths but are still very important to me: Lucas Secco, Felipe Selau, Mariana Timm, Amanda Azevedo, Vinícius Ferreira, Demétrius Lima and Matheus Heinemann. I extend this acknowledgment to the friends I made at the Department of Physics and Astronomy at Aarhus University during my time in Denmark, who made sure I had a nice time there: John Sandoval, Jacobus Swartz, Denis Hove and Felipe Bellotti.

I would not have made it this far without the unconditional support of my family: my sister Aline Barfknecht and my awesome nephew Augusto, and my parents Dilamar Barfknecht and Valdair Barfknecht. Their encouragement and patience throughout these years have allowed me to reach this goal, and this work is dedicated to them. I had also the invaluable support of Beatriz Camaño and Jorge Silvestrini, who have truly taken me in as part of their family. This also goes to Laura and Nahuel, who always welcomed me in our trips to Argentina!

Last but not least I want to thank my girlfriend Marion Lucia Silvestrini, whose love and kindness keep me going forward through good and bad times.

To all of you I am extremely thankful!

*Rafael Emilio Barfknecht,*
*Porto Alegre, May 30, 2019.*

# List of Publications

- **R. E. Barfknecht**, A. S. Dehkharghani, A. Foerster and N. T. Zinner, *"Correlation properties of a three-body bosonic mixture in a harmonic trap"*, J. Phys. B: Atomic, Molecular and Optical Physics, **49**, 135301 (2016); DOI: 10.1088/0953-4075/49/13/135301, URL: http://iopscience.iop.org/article/10.1088/0953-4075/49/13/135301

- **R. E. Barfknecht**, A. Foerster and N. T. Zinner, *"Dynamical realization of magnetic states in a strongly interacting Bose mixture"*, Phys. Rev. A, **95**, 023612 (2017); DOI: 10.1103/PhysRevA.95.023612, URL: https://journals.aps.org/pra/abstract/10.1103/PhysRevA.95.023612

- **R. E. Barfknecht**, A. Foerster and N. T. Zinner, *"Effects of interaction imbalance in a strongly repulsive one-dimensional Bose gas"*, Few-Body Systems, **59**, 3 (2018); DOI: 10.1007/s00601-018-1352-4, URL: https://link.springer.com/article/10.1007/s00601-018-1352-4

- **R. E. Barfknecht**, A. Foerster and N. T. Zinner, *"Emergence of junction dynamics in a strongly interacting Bose mixture"*, New J. Phys., **20**, 063014 (2018); DOI: 10.1088/1367-2630/aac718, URL: http://iopscience.iop.org/article/10.1088/1367-2630/aac718

- **R. E. Barfknecht**, S. A Rasmussen, A. Foerster and N. T. Zinner, *"Realizing time crystals in discrete quantum few-body systems"*, arXiv:1807.08688, URL: https://arxiv.org/abs/1807.08688

- **R. E. Barfknecht**, A. Foerster and N. T. Zinner, *"Spin-charge separation in strongly interacting multicomponent few-body systems"*, arXiv:1812.01976, URL: https://arxiv.org/abs/1812.01976

# Contents

# Part I

# Overview

# Chapter 1

# Introduction

The experimental realization of the first Bose-Einstein condensates (BECs) [1, 2] in the 90's paved the way for a whole new area of reasearch in physics. By employing techniques such as laser [3] and evaporative cooling [4], physicists were able to produce atomic ensembles at extremely low temperatures. Under such conditions, a bosonic system will have a large fraction of its atoms in the quantum state of lowest energy. This means that a simple theoretical approach can be used to describe a system which is in general composed of thousands of particles [5, 6].

These experiments were able to demonstrate in practice the validity of textbook theories belonging to diverse fields like statistical physics [7, 8] and quantum mechanics [9, 10]. However, the regime in which they take place was by no means easy to achieve. Besides the aforementioned cooling to temperatures close to zero, the atomic ensembles used in the experiments needed to be put in position and controlled so their properties could be measured with the required precision [11].

The answer to this challenge came in the form of the so-called magneto-optical traps (MOTs) [12, 13], where laser arrays and magnetic fields are applied in order to create potential minima, therefore trapping the atoms. The many ways in which these arrays can be arranged allow for the creation of traps with different shapes and sizes. Most importantly, different directions can be chosen to have distinct trapping lengths, creating systems with an effectively lower dimensionalty. For instance, by choosing a shorter trapping length in one direction as opposed to another, it became possible to "freeze" degrees of freedom and create systems of atoms which move and interact along a one-dimensional optical tube.

As an additional effect, the presence of magnetic fields and optical trapping can lead to two related phenomena of decisive importance for these experiments: Feshbach [14] and confinement induced resonances [15]. In the first case, the strength of external magnetic fields can determine the energy difference between scattering channels of a certain atomic species, leading to

the possiblity of tuning the scattering length (which in turn determines the strength of repulsive or attractive interactions between pairs of atoms). In the second case, the presence of tight confinement along some direction in the system is able to change the scattering length in an effectively lower dimensionality, which also reflects on the strength of the interactions between the atoms.

Suddenly, theories which seemed to be only toy models were now subject to experimental verification [16]. This is the case, for instance, of a class of one-dimensional models of particles with contact interactions, such as the Lieb-Liniger model [17, 18] of interacting bosons, Mcguire's fermionic impurity problem [19, 20] and the Gaudin-Yang model [21, 22] for two-component fermions. These models have the attractive property of being integrable [8], meaning that they have an exact solution in terms of the celebrated method known as the Bethe *ansatz* [23].

These advances gave rise to a number of experiments with one-dimensional systems in different trapping geometries and interaction regimes, ranging from the weakly interacting one-dimensional analogue of a BEC [24] (which is treated theoretically via the Gross-Pitaevskii theory [6]) to the infinitely repulsive system of bosons called the Tonks-Girardeau gas [25–27]. Even more refined techniques of atomic manipulation allowed for further control over the size of these systems in terms of particle number. Experiments consisting of no more than two or three atoms in a harmonic trap made possible the measurement of quantum properties of systems well away from the many-body regime [28, 29]. Moreover, by increasing the number of atoms one-by-one, the elusive regime where few- and many-body phenomena overlap was achieved [30].

A large number of theoretical studies followed in the trails of these practical advances. Many of these works deal with the fact that, in real experiments, atoms are usually trapped by an external potential [31], which, in general, renders the one-dimensional system non-integrable. Others additionally consider a regime of interactions beyond the realm of validity of most theories [32–34].

All of these developments have culminated in striking realizations that combine theory and experiment to achieve results that could only be dreamed of a few decades ago. Among these impressive accomplishments, we can highlight the measurement of a non-thermalizing system of bosons in a one-dimensional trap [35] (which captures the physics of an integrable system in the lab), the realization of 1D fermionic systems with several internal components [36] which leads to the exotic concept of synthetic dimensions [37, 38], the observation of the magnetic properties of a system composed of three $^6$Li atoms [39], among others. Recent works propose taking advantage os this high degree of control to explore cold atoms as platforms for quantum simulations [40, 41], and several experiments in this direction are being presently performed. In this scenario, the experimental setup would be able to mimic the properties of interesting physical systems (even beyond the standard mod-

els of condensed matter) and entirely replace the simulations performed with classical computers.

This thesis is the results of learning about all of these developments, and in turn trying to come up some contribution to the field. Most of the work presented here has been published in scientific journals, but the order of the presentation is not necessarily chronological. The next chapter, for instance, simply outlines the theoretical formalism that is applied to different problems throughout the thesis.

The second part of the thesis is dedicated to the application of this formalism to different problems in the dynamics of strongly interacting one-dimensional systems. Our main focus lies in the description of interesting dynamical effects, such as magnetic transitions, impurity oscillations, state transfer and spin-charge separation. An important feature troughout our studies is the role of interactions on these effects and the consequence of changing such parameters is a recurring theme in this work.

The third part deals with slightly different approaches, for regimes outside the limit of strong interactions, but also focusing on properties which can, in principle, be measured in the lab. We start with a description of the static properties of a few-body mixture with a variational approach to the wave function, and then present a study of the dynamics of a many-body Bose mixture governed by the Gross-Pitaevskii equation.

In each chapter, we provide a short introduction describing the goal of the sections contained in it and stating in detail the modifications made with respect to the published work, when that is the case. When necessary, we also provide a description of the system where we include the relevant definitions, before jumping into the actual calculations and results. We point out that, while in many cases the theoretical approach between different studies is equivalent, the notation may be conveniently adapted from one chapter to another.

# Chapter 2

# Strongly interacting one-dimensional systems

In this chapter we describe the theory that will be applied in several static and dynamic problems throughout this work. It can be generally described as a mapping of a one-dimensional strongly interacting two-component system of atoms to a spin chain Hamiltonian, where the exchange coefficients between neighboring spins are determined from the geometry of the trapping potential. Section 2.2 has been published, with minor modifications, as an appendix in Ref. [42].

As a first step, we describe a system of one-dimensional bosons with infinitely repulsive contact interactions, the so-called Tonks-Girardeau gas.

## 2.1 The Tonks-Girardeau gas

We consider initially a system of $N$ bosons in one dimension with contact interactions, as described by the following Hamiltonian:

$$H = \sum_{i=1}^{N} H_0(x_i) + g \sum_{i<j}^{N} \delta(x_i - x_j) \tag{2.1}$$

where

$$H_0(x) = -\frac{\hbar^2}{2m}\frac{\partial^2}{\partial x^2} + V(x) \tag{2.2}$$

is the single-particle Hamiltonian in a trapping potential $V(x)$, where $m$ denotes the mass of the particles (we always assume particles with equal masses). The interaction between the particles is given by the rightmost term in Eq. (2.1). The interaction strength $g$ is written in the energy units given by $\epsilon = \frac{\hbar^2}{mL}$, where $L$ is the characteristic length of the system and $\hbar$ is the reduced Planck's constant. Throughout the rest of this work, we will usually write the interaction parameters in this dimensionless form.

For the simple case of $g = 0$, the solutions are given simply by the single-particle eigenstates of Eq. (2.2). For the case of general $g$, the solution for this problem has been originally found by Elliott Lieb and Werner Liniger [17, 18], for a system with periodic boundary conditions (the so-called Lieb-Liniger model). The basic idea behind the method is to postulate a trial wave function and then impose conditions for its derivative at the contact point between two particles (where the interaction happens). These conditions are usually contemplated in the form of a set of Bethe *ansatz* equations, which is a general feature of integrable systems. This solution holds only in the absence of an external trapping potential ($V(x) = 0$ in Eq. (2.2)).

The case of infinite repulsion ($g = \infty$), however, has an exact solution found in 1960 by Marvin Girardeau, which holds even in the presence of a trapping geometry. In his work, Girardeau showed that the wave function for a gas of impenetrable particles has to satisfy two conditions: first, since the system is one-dimensional and the repulsion is infinite, the particles cannot cross each other. This means that the many-body wave function $\psi(x_1, x_2, ..., x_N)$ of the system can be written as a combination of the solutions in different sectors, by which we mean the possible different orderings of the coordinates. Second, the infinite interactions also require the wave function to vanish at the contact point between two particles, that is $\psi(x_1, ..., x_i, ..., x_j, ..., x_N)|_{x_i=x_j} = 0$. Girardeau showed that the bosonic wave function $\Phi_B(x_1, ..., x_N)$ that satisfies these conditions, while also preserving its symmetric nature, is simply written as

$$\Phi_B(x_1, ..., x_N) = |\Phi_F(x_1, ..., x_N)|, \tag{2.3}$$

where $\Phi_F(x_1, ..., x_N)$ denotes the wave function for a system of spinless fermions in the same geometry. The bosonic wave function in the limit of infinite repulsion can thus be interpreted simply as the symmetrized version of the wave function for identical fermions. Therefore, this correspondece is usually called Bose-Fermi mapping. This result is particularly interesting since the wave function for spinless fermions has a simple representation in terms of a Slater determinant for $N$ particles [43]:

$$\Phi_F(x) = \frac{1}{\sqrt{N!}} \begin{vmatrix} \phi_1(x_1) & \phi_2(x_1) & \dots & \phi_N(x_1) \\ \phi_1(x_2) & \phi_2(x_2) & \dots & \phi_N(x_2) \\ \dots & \dots & \ddots & \vdots \\ \phi_1(x_N) & \phi_2(x_N) & \dots & \phi_N(x_N) \end{vmatrix},$$

where $\phi_n(x)$ denotes the $n$-th eigenstate of the single-particle Hamiltonian (2.2). Therefore, by knowing these solutions in a given potential $V(x)$, it is possible to calculate the wave function for a many-body gas of impenetrable bosons. This analogy between the Tonks-Girardeau gas and the gas of spinless fermions also holds for the energy. In the fermionic case, each particle has to occupy a different energy level, due to the Pauli exclusion principle. In the

bosonic case, the infinite repulsion mimics that effect, the result being that the energy of both systems is simply the sum of the energy of each single-particle orbital.

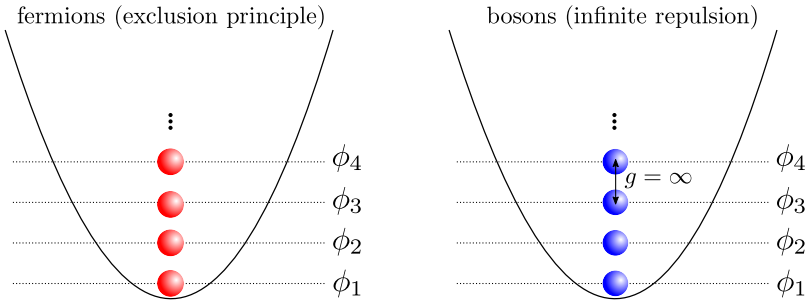


*Figure 2.1: A trapped system of spinless fermions is mapped into a system of infinitely repulsive bosons. The particles are placed one by one in each energy level (with a corresponding wave function given by $\phi_n$), in the fermionic case as a result of the exclusion principle, and in the bosonic case due to the interactions.*

As an example, we calculate now the wave function for the Tonks-Girardeau gas in the simple case of $N = 3$. Our choice of potential will be a harmonic trap, given by $V(x) = \frac{1}{2}m\omega^2 x^2$, with frequency $\omega = 1$. We also assume for simplicity that $\hbar = m = 1$. The Tonks-Girardeau wave function obtained by calculating the Slater determinant for the lowest $N = 3$ orbitals is given by

$$\Phi_B(x_1, x_2, x_3) = \frac{e^{-\frac{1}{2}(x_1^2+x_2^2+x_3^2)}}{3\pi^{3/4}}|(x_1 - x_2)(x_1 - x_3)(x_2 - x_3)|, \tag{2.4}$$

where we see that the bosonic symmetry is preserved, but the wave function still vanishes for $x_i = x_j$. A quantity of great importance in the following chapters will be the single-particle densities, which determine the spatial distributions of individual particles in the trap. It is defined as

$$\rho(x) = \int dx_1 \dots dx_N |\Phi(x_1, ..., x, ..., x_N)|^2, \tag{2.5}$$

where the integrals are performed in the entire domain of the trapping potential under consideration. Calculating these densities for the example above, we obtain the distribution shown in Fig. 2.2, where we consider the dimensionless units determined by the harmonic oscillator length scale $l = \sqrt{\hbar/(m\omega)}$.

Clearly, an important feature of the Bose-Fermi mapping is the correspondence between the energies and the spatial distributions of a system of impenetrable bosons and a system of spinless fermions. This is expected since the wave functions for these systems only differ by a symmetry factor. However, this correspondence is not extended to all quantities. A notable exception is the momentum distribution, a measurable quantity where the symmetry of the wave function is explicitly manifested [44, 45].

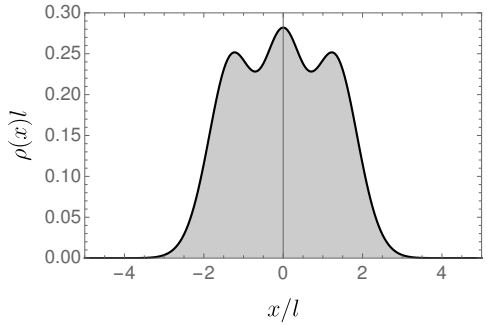


*Figure 2.2: One-body correlations for a Tonks-Girardeau gas with $N = 3$. Total density is normalized to 1.*

### 2.1.1 Spatially ordered densities

While Eq. (2.5) provides the single-particle distribution of a Tonks-Girardeau gas, it will be necessary in the next chapters to calculate the individual densities for particles in a given sector (that is, a particular ordering of the coordinates). To do so, we must calculate

$$\rho^i(x) = \int_\Gamma dx_1 \ldots dx_N \, \delta(x_i - x)|\Phi(x_1, ..., z, ..., x_N)|^2, \tag{2.6}$$

where the sector is defined by the integration domain (e.g $\Gamma = x_1 < x_2 < \ldots < x_N$) and the Dirac delta function picks out the distribution for a single particle. Some analytical results can be obtained for this quantity in few-body systems. Considering the case of $N = 3$ in a harmonic trap, for instance, we obtain

$$\begin{aligned}
\rho^1(x) &= A\, e^{-3x^2}\Big[ -8\sqrt{\pi}e^{x^2} x \left(x^2-1\right) \mathrm{erfc}(x) \\
&+ \pi e^{2x^2} \left(4x^4+3\right) \mathrm{erfc}(x)^2 + 4\left(x^2-2\right)\Big] \\
\rho^2(x) &= 2A\, e^{-3x^2}\Big\{ -8\sqrt{\pi}e^{x^2} \left(x^2-1\right) x\, \mathrm{erf}(x) \\
&- \pi e^{2x^2} \left(4x^4+3\right) [\mathrm{erfc}(x)-2]\, \mathrm{erfc}(x) - 4x^2 + 8\Big\} \\
\rho^3(x) &= A\, e^{-3x^2}\Big\{8\sqrt{\pi}e^{x^2} x \left(x^2-1\right) [\mathrm{erf}(x)+1] \\
&+ \pi e^{2x^2} \left(4x^4+3\right) [\mathrm{erf}(x)+1]^2 + 4\left(x^2-2\right)\Big\},
\end{aligned} \tag{2.7}$$

where $\mathrm{erf}(x) = \frac{1}{\pi}\int_{-x}^{x} e^{-y^2} dy$ is the error function, $\mathrm{erfc}(x) = 1 - \mathrm{erf}(x)$ is the complementary error function, and $A$ is a numeric constant theat assures that each distribution is normalized to unity. In Fig. 2.3 we plot the densities given by the expressions above, where it becomes clear that each expression provides the distribution of the particles in a given order.

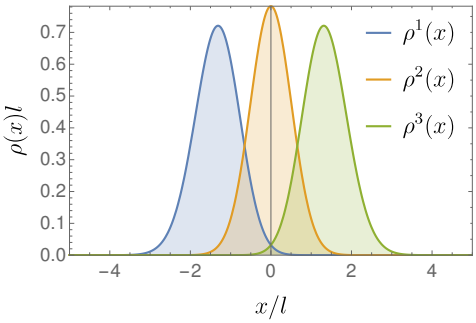


*Figure 2.3: Spatial densities for a harmonically trapped Tonks-Girardeau gas with $N = 3$, in the sector $\Gamma = x_1 < x_2 < x_3$.*

For larger $N$, the integrals defined in Eq. (2.6) become increasingly harder to calculate. However, by exploring the determinant form of $\Phi(x_1, ..., x > N)$, it is possible to rewrite this expression (as shown by F. Deuretzbacher in Ref. [32]) as

$$\rho^i(x) = \frac{\partial}{\partial x}\left(\sum_{j=0}^{N-1} c_j^i \frac{\partial^j}{\partial \lambda^j} \det\left[B(x) - 1\lambda\right]|_{\lambda=0}\right), \tag{2.8}$$

where

$$c_j^i = \frac{(-1)^{N-1}(N-j-1)!}{(i-1)!(N-j-i)!j!} \tag{2.9}$$

and the matrix $B(x)$ is composed by the single particle states superpositions $b_{mn}(x) = \int_{-\infty}^{x} dy\, \phi_m(y)\phi_n(y)$ (here $\phi(x)$ again denote the single particle orbitals which go up to the state corresponding to the $N$-th particle). In Fig. 2.4 we show the results obtained with this expression for $N = 10$. In the case of a symmetric potential, the calculations can be considerably reduced by obtaining the distributions up to $x = 0$ and then mirroring the results to get the positive values of $x$.

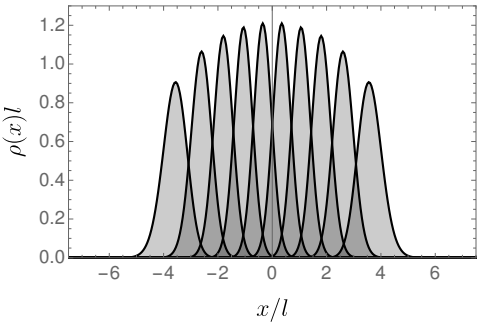


*Figure 2.4: Spatial densities for a harmonically trapped Tonks-Girardeau gas with $N = 10$, in the sector $\Gamma = x_1 < x_2 < ... < x_N$, calculated with expression (2.8).*

Throughout this thesis, we consider the density for each individual particle as given by Eq. (2.6) to be normalized to unity, unless stated otherwise. This means that the total density $\rho(x) = \sum_i^N \rho^i(x)$ is always normalized to the total number of particles $N$.

## 2.2 Mapping between a strongly interacting two-component system and a spin chain

We now present a derivation of the spin chain Hamiltonian as a model for strongly interacting two-component gases in one-dimension. Although different approaches can be employed to obtain this result, the content of this section follows the calculations presented in Ref. [46].

We start by considering a two component bosonic gas in one dimension with contact interactions. We label each component by its internal state (either $\uparrow$, or $\downarrow$). The numbers of particles of each component is then given by $N_\uparrow$ and $N_\downarrow$, an the total number of particles is written as $N = N_\uparrow + N_\downarrow$. We consider all particles with the same mass $m$, and the units of length and energy are given as $L$ and $\epsilon = \frac{\hbar^2}{mL}$. The Hamiltonian is then written as

$$\begin{aligned} H &= \sum_{i=1}^{N} H_0(x_i) + g\sum_{i}^{N_\uparrow}\sum_{j}^{N_\downarrow}\delta(x_{\uparrow i} - x_{\downarrow j}) \\ &+ \kappa g\sum_{i<i'}^{N_\uparrow}\delta(x_{\uparrow i} - x_{\uparrow i'}) + \kappa g\sum_{j<j'}^{N_\downarrow}\delta(x_{\downarrow j} - x_{\downarrow j'}), \end{aligned} \tag{2.10}$$

where $g$ denotes the interaction strength between different particles, and $\kappa g$ sets the interaction strength between identical particles (we focus only on repulsive interactions, so $g, \kappa > 0$).

In the limit of infinite interactions ($g \to \infty$), the eigenstates of Hamiltonian (2.10) can be described by

$$\Psi = \sum_{k=1}^{L(N_\uparrow, N_\downarrow)} a_k P_k \Phi(\{x_{\uparrow i}, x_{\downarrow j}\}), \tag{2.11}$$

where the sum runs over the $L(N_\uparrow, N_\downarrow) = \binom{N_\uparrow + N_\downarrow}{N_\uparrow}$ permutations of the coordinates, $P_k$ is the permutation operator (which exchanges the order of particles denoted by $k$) and $a_k$ is the coefficient that denotes the probability amplitude for a given order. In this expression, $\Phi$ is simply the wave function in the impenetrable limit, with coordinates ordered as $x_{\uparrow 1} < x_{\uparrow 2} < ... < x_{\uparrow N_\uparrow} < x_{\downarrow 1} < ... < x_{\downarrow N_\downarrow}$. We note that that permutations between indistinguishable particles are not taken into account in the wave function described above. These terms can be obtained by simply exchanging coordinates and considering the symmetry of the wave function $\Phi$. As detailed in Section 2.1, $\Phi$ must

be symmetric (antisymmetric) with respect to exchanges of identical particles for bosons (fermions).

To investigate the behavior of the energy at very strong (but finite) interactions, we use the Hellmann-Feynman theorem, which gives

$$\begin{aligned}\frac{\partial E}{\partial g} &= \sum_{i=1}^{N_\uparrow}\sum_{j=1}^{N_\downarrow}\langle\Psi|\delta(x_{\uparrow i}-x_{\downarrow j})|\Psi\rangle+\kappa\sum_{i<i'}^{N_\uparrow}\langle\Psi|\delta(x_{\uparrow i}-x_{\uparrow i'})|\Psi\rangle \\ &+ \kappa\sum_{j<j'}^{N_\downarrow}\langle\Psi|\delta(x_{\downarrow j}-x_{\downarrow j'})|\Psi\rangle, \end{aligned} \tag{2.12}$$

where the first term on the right-hand side accounts for interactions between different bosons, while the remaining terms arise from interactions between identical bosons. The Dirac brackets in this expression denote the integral over all coordinates.

Inspired by the Bethe *ansatz* approach, we can write the conditions for the derivatives of the wave function at the contact point between two particles as

$$\begin{aligned}\left(\frac{\partial\Psi}{\partial x_{\uparrow i}}-\frac{\partial\Psi}{\partial x_{\uparrow i'}}\right)\Bigg|_-^+ &= 2\kappa g\Psi(x_{\uparrow i}=x_{\uparrow i'}), \\ \left(\frac{\partial\Psi}{\partial x_{\downarrow j}}-\frac{\partial\Psi}{\partial x_{\downarrow j'}}\right)\Bigg|_-^+ &= 2\kappa g\Psi(x_{\downarrow j}=x_{\downarrow j'})\end{aligned} \tag{2.13}$$

for identical bosons and

$$\left(\frac{\partial\Psi}{\partial x_{\uparrow i}}-\frac{\partial\Psi}{\partial x_{\downarrow j}}\right)\Bigg|_-^+ = 2g\Psi(x_{\uparrow i}=x_{\downarrow j}), \tag{2.14}$$

for a distinguishable pair. In the expressions above we have $+\rightarrow x_m - x_n = 0^+$, while $-\rightarrow x_m - x_n = 0^-$.

Combining Eqs. (2.12), (2.13) and (2.14), we get

$$\frac{\partial E}{\partial g} = \frac{K_{\uparrow\downarrow}}{g^2}+\frac{K_{\uparrow\uparrow}}{\kappa g^2}+\frac{K_{\downarrow\downarrow}}{\kappa g^2}, \tag{2.15}$$

where

$$K_{\uparrow\downarrow} = \frac{\sum_{i=1,j=1}^{N_\uparrow,N_\downarrow} \int dx_{\uparrow 1},\cdots,dx_{\uparrow N_\uparrow} \int dx_{\downarrow 1},\cdots,dx_{\downarrow N_\downarrow} \left| \left( \frac{\partial\Psi}{\partial x_{\uparrow i}} - \frac{\partial\Psi}{\partial x_{\downarrow j}} \right) \right|_-^+{}^2 \delta(x_{\uparrow i} - x_{\downarrow j})}{4 \int dx_{\uparrow 1},\cdots,dx_{\uparrow N_\uparrow} \int dx_{\downarrow 1},\cdots,dx_{\downarrow N_\downarrow} |\Psi|^2},$$

$$K_{\uparrow\uparrow} = \frac{\sum_{i<i'}^{N_\uparrow} \int dx_{\uparrow 1},\cdots,dx_{\uparrow N_\uparrow} \int dx_{\downarrow 1},\cdots,dx_{\downarrow N_\downarrow} \left| \left( \frac{\partial\Psi}{\partial x_{\uparrow i}} - \frac{\partial\Psi}{\partial x_{\uparrow i'}} \right) \right|_-^+{}^2 \delta(x_{\uparrow i} - x_{\uparrow i'})}{4 \int dx_{\uparrow 1},\cdots,dx_{\uparrow N_\uparrow} \int dx_{\downarrow 1},\cdots,dx_{\downarrow N_\downarrow} |\Psi|^2},$$

$$K_{\downarrow\downarrow} = \frac{\sum_{j<j'}^{N_\downarrow} \int dx_{\uparrow 1},\cdots,dx_{\uparrow N_\uparrow} \int dx_{\downarrow 1},\cdots,dx_{\downarrow N_\downarrow} \left| \left( \frac{\partial\Psi}{\partial x_{\downarrow j}} - \frac{\partial\Psi}{\partial x_{\downarrow j'}} \right) \right|_-^+{}^2 \delta(x_{\downarrow j} - x_{\downarrow j'})}{4 \int dx_{\uparrow 1},\cdots,dx_{\uparrow N_\uparrow} \int dx_{\downarrow 1},\cdots,dx_{\downarrow N_\downarrow} |\Psi|^2},$$

and the denominator in each of these expressions introduces simply a normalization factor. Notice that, in the expressions above, we have restored the delta function on the right side to keep the integration over all coordinates. Integrating with respect to $g$ we obtain the following energy functional

$$E = E_0 - \left( \frac{K_{\uparrow\downarrow}}{g} + \frac{K_{\uparrow\uparrow}}{\kappa g} + \frac{K_{\downarrow\downarrow}}{\kappa g} \right), \tag{2.16}$$

where $E_0$ is the energy in the limit of infinite repulsion, and we neglect terms of higher order in ($1/g$ - we remember that, for strong interactions, $1/g^2 \ll 1$). By introducing the wave function described by Eq. (2.11) in the expression above, we obtain

$$E = E_0 - \frac{\sum_{i=1}^{N-1} \frac{\alpha_i}{g} \left( \sum_{k=1}^{L(N_\uparrow-1,N_\downarrow-1)} A_{ik}^{\uparrow\downarrow} + \frac{2}{\kappa} \sum_{k=1}^{L(N_\uparrow-2,N_\downarrow)} A_{ik}^{\uparrow\uparrow} + \frac{2}{\kappa} \sum_{k=1}^{L(N_\uparrow,N_\downarrow-2)} A_{ik}^{\downarrow\downarrow} \right)}{\sum_{k=1}^{L(N_\uparrow,N_\downarrow)} a_k^2} \tag{2.17}$$

with

$$A_{ik}^{\uparrow\downarrow} = (a_{ik}^{\uparrow\downarrow} - a_{ik}^{\downarrow\uparrow})^2, \qquad A_{ik}^{\uparrow\uparrow} = (a_{ik}^{\uparrow\uparrow})^2, \qquad A_{ik}^{\downarrow\downarrow} = (a_{ik}^{\downarrow\downarrow})^2, \tag{2.18}$$

where $a_{ik}^{\uparrow\downarrow}$ represents the coefficients in Eq. (2.11) multiplying terms with neighboring $\uparrow$ and $\downarrow$ particles at position $i$ and $i+1$, while the remainig terms have the same role, for $\downarrow\uparrow$, $\uparrow\uparrow$ and $\downarrow\downarrow$ pairs. The purpose of such terms is to account for the energy contribution of exchanging two neighboring particles with particular spin projections, while other particles remain in the same ordering determined by $k$. The coefficients $\alpha_i$ are now independent of spin [47], and can be written as

$$\alpha_i = \frac{\int_{x_1<x_2\cdots<x_N-1} dx_1 ... dx_{N-1} \left| \frac{\partial\Phi(x_1,\cdots,x_i,\cdots,x_N)}{\partial x_N} \right|_{x_N=x_i}^2}{\int_{x_1<x_2\cdots<x_N-1} dx_1 \cdots dx_N |\Phi(x_1,\cdots,x_i,\cdots,x_N)|^2}, \tag{2.19}$$

where $\Phi(x_1, \cdots, x_i, \cdots, x_N)$ is again the wave function present in Eq. (2.11) (where we have omitted the spin indices). Since this wave function is defined in the region determined by a particular order of the coordinates, it is enough to calculate the integrals in one particular sector, such as $x_1 < x_2 \cdots < x_N - 1$.

Now, let us consider a spin chain Hamiltonian defined as

$$H_s = E_0 - \sum_{i=1}^{N-1} J_i \left( \Pi_{\uparrow\downarrow}^{i,i+1} + \frac{1}{\kappa} \Pi_{\uparrow\uparrow}^{i,i+1} + \frac{1}{\kappa} \Pi_{\downarrow\downarrow}^{i,i+1} \right) \tag{2.20}$$

where $\Pi_{\uparrow\downarrow}^{i,i+1} = \frac{1}{2}(\mathbb{1} - \vec{\sigma}^i \cdot \vec{\sigma}^{i+1})$ is the operator that exchanges neighboring spins with different projections and $\Pi_{\uparrow\uparrow}^{i,i+1} = \Pi_{\downarrow\downarrow}^{i,i+1} = \frac{1}{2}(\mathbb{1} + \sigma_z^i \sigma_z^{i+1})$ have the same action, but for identical spins. A generic spin state can now be written as

$$|\chi\rangle = \sum_{k=1}^{L(N_\uparrow, N_\downarrow)} a_k P_k |\uparrow_1 \cdots \uparrow_{N_\uparrow} \downarrow_1 \cdots \downarrow_{N_\downarrow}\rangle, \tag{2.21}$$

where once again the sum runs over the permutations of the $N_\uparrow$ and $N_\downarrow$ spins. If we calculate the expected value of Hamiltonian (2.20) as $\langle\chi|H|\chi\rangle$, we obtain

$$\langle\chi|H|\chi\rangle = E_0 - \frac{\sum_{i=1}^{N-1} J_i \left( \sum_{k=1}^{L(N_\uparrow - 1, N_\downarrow - 1)} A_{ik}^{\uparrow\downarrow} + \frac{2}{\kappa} \sum_{k=1}^{L(N_\uparrow - 2, N_\downarrow)} A_{ik}^{\uparrow\uparrow} + \frac{2}{\kappa} \sum_{k=1}^{L(N_\uparrow, N_\downarrow - 2)} A_{ik}^{\downarrow\downarrow} \right)}{\sum_{k=1}^{L(N_\uparrow, N_\downarrow)} a_k^2} \tag{2.22}$$

where the coefficients $A_{ik}^{\uparrow\downarrow}$, $A_{ik}^{\uparrow\uparrow}$ and $A_{ik}^{\downarrow\downarrow}$ have the same meaning as in Eq. (2.18), and $\sum_{k=1}^{L(N_\uparrow, N_\downarrow)} a_k^2$ introduces a normalization factor. It becomes clear that the energy functionals given by Eqs. (2.17) and (2.22) are identical for $J_i = \alpha_i / g$. Furthermore, by rewriting Eq. (2.20) in terms of the Pauli matrices

$$\sigma_x = \begin{pmatrix} 0 & 1 \\ 1 & 0 \end{pmatrix}, \ \sigma_y = \begin{pmatrix} 0 & -i \\ i & 0 \end{pmatrix}, \ \sigma_z = \begin{pmatrix} 1 & 0 \\ 0 & -1 \end{pmatrix}. \tag{2.23}$$

we obtain

$$H_s = E_0 \mathbb{1} - \sum_{i=1}^{N-1} \frac{\alpha_i}{g} \left[ \frac{1}{2}(\mathbb{1} - \vec{\sigma}^i \cdot \vec{\sigma}^{i+1}) + \frac{1}{\kappa}(\mathbb{1} + \sigma_z^i \sigma_z^{i+1}) \right], \tag{2.24}$$

where $\mathbb{1}$ is the identity matrix. We conclude then that the eigenvalue problems defined with Eqs. (2.17) and (2.22) are identical, which validates, for a strongly interacting system, the mapping between Hamiltonians (2.10) and (2.24). From now on, we assume that the spin eigenstates in a strongly interacting system are described by the solution of Eq. (2.24).

## 2.3 Geometric coefficients

In this section we present some results for the geometric coefficients in a system with an increasingly larger number of particles. As stated previously, the geometric coefficients can be calculated using

$$\alpha_i = \frac{\int_{x_1<x_2\cdots<x_N-1} dx_1 ... dx_{N-1} \left| \frac{\partial \Phi(x_1,\cdots,x_i,\cdots,x_N)}{\partial x_N} \right|^2_{x_N=x_i}}{\int_{x_1<x_2\cdots<x_N-1} dx_1 \cdots dx_N |\Phi(x_1,\cdots,x_i,\cdots,x_N)|^2}. \tag{2.25}$$

In Table (2.1) we present the numerical values for these exchange coefficients for a system of up to $N = 6$ in the presence of a harmonic trap. Note that the sole function of these coefficients is to encode the geometry of the trapping potential; for instance, as the potential gets deeper, we find that the numerical values of the coefficients increase. Furthermore, if the potential is symmetric around the origin, this symmetry is also reflected in the coefficients and we must calculate at most $N/2$ coefficients for even $N$ and $(N-1)/2$ for odd $N$. An interesting way to visualize the magnitude of the geometrical coefficients is to think also in terms of the overlaps between particles in the trap - the larger the overlap, the greater the numerical value of $\alpha_i$ (see Fig. 2.4, for instance).

| $N$ | $\alpha_1/(\hbar^2\omega^2 l)$ | $\alpha_2/(\hbar^2\omega^2 l)$ | $\alpha_3/(\hbar^2\omega^2 l)$ |
|---|---|---|---|
| 2 | 0.7978 | | |
| 3 | 1.3464 | | |
| 4 | 1.7876 | 2.3465 | |
| 5 | 2.1661 | 3.1773 | |
| 6 | 2.5031 | 3.9054 | 4.3605 |

*Table 2.1: Numerical values of the geometric coefficients for N particles in a harmonic trap. Since the trapping potential is symmetric, it is enough to calculate at most $N/2$ coefficients for any system.*

For large $N$, the multidimensional integrals given by Eq. (2.25) become hard to calculate, as is the case for the individual particle densities. One way around this problem is to again explore the determinant form of the spinless fermion wave function $\Phi(x_1, x_2, ..., x_N)$. This leads to [48, 49]:

$$\begin{aligned} \alpha_i &= \sum_{j=1}^{N}\sum_{k=1}^{N}(-1)^{j+k}\int_{-\infty}^{+\infty} dx_i\, \phi_j'(x_i)\phi_k'(x_i) \sum_{l=0}^{N-1-i} \frac{(-1)^{N-1-i}}{l!}\binom{N-l-2}{i-1} \\ &\times \frac{d}{dx_i}\left[\frac{\partial}{\partial\lambda^l}\det\left(B(x_i)-1\lambda\right)_{jk}|_{\lambda=0}\right] \end{aligned} \tag{2.26}$$

where $\phi_j'(x_i)$ denotes the spatial derivative of a given single-particle orbital. Once again the matrix $B(x)$ is composed by the single-particle states superpositions $b_{mn}(x) = \int_{-\infty}^{x} dy\, \phi_m^*(y)\phi_n(y)$, and the subscript $jk$ on the right side

indicates that the $j$-th row and $k$-th column are removed. While we do not explicitly include the time parameter in these expressions, we could consider the orbitals $\phi_i(x)$ to be time-dependent.

In Fig. 2.5, we compare the values of Table (2.1) with results calculated with expression (2.26). In the next chapter, we use this expression to simplify the calculations for the case of time-dependent coefficients.

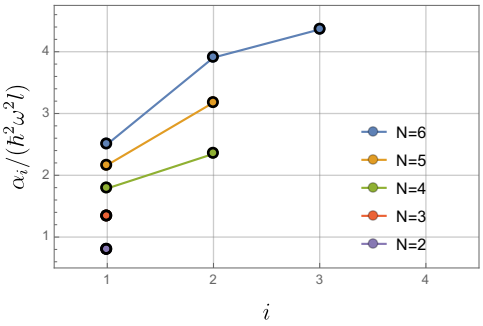


*Figure 2.5: Numerical values of the goemetric coefficients with increasing $N$. The colored solid lines connect the coefficients for a same number of particles, while the black circles show the numerical results obtained with Eq.* (2.26).

For larger systems, the open source package CONAN [48] is available and can calculate the geometrical coefficients for up to $N \approx 30$ in arbitrary potentials. This opens up the perspective of studying the static and dynamical properties of spin chains where the exchange coefficients are specially tailored to achieve interesting properties [47, 50].

## 2.4 Exact solutions in a fermionic 2+1 system

We now use the formalism presented in the last sections to calculate, as an example, the spin densities for a fermionic system with $N_\uparrow = 2$ and $N_\downarrow = 1$. We additionally compare the results with numerical calculations performed with the method of Matrix Product States (MPS) using the open package OpenMPS [51]. We begin by writing the Hamiltonian for the fermionic spin chain as

$$H_s = E_0 \mathbb{1} - \sum_{i=1}^{N-1} \frac{\alpha_i}{g} \left[ \frac{1}{2} (\mathbb{1} - \vec{\sigma}^i \cdot \vec{\sigma}^{i+1}) \right], \tag{2.27}$$

where the coefficients $\alpha$ are given by $N = 3$ in Table (2.1). Notice that, in comparison to Eq. (2.20), this Hamiltonian does not include the term of intraspecies interaction governed by $\kappa$. The reason for this is that any interaction between identical fermions is ruled out by the Pauli exclusion principle.

We then write our Hamiltonian in a truncated basis composed by $|\uparrow\uparrow\downarrow\rangle$, $|\uparrow\downarrow\uparrow\rangle$ and $|\downarrow\uparrow\uparrow\rangle$. We choose an interaction strength of $g = 25$, and diagonalize

the Hamiltonian to find the following eigenstates

$$\begin{aligned} |\psi_1\rangle &= -\frac{1}{\sqrt{6}}|\uparrow\uparrow\downarrow\rangle + \sqrt{\frac{2}{3}}|\uparrow\downarrow\uparrow\rangle - \frac{1}{\sqrt{6}}|\downarrow\uparrow\uparrow\rangle \\ |\psi_2\rangle &= -\frac{1}{\sqrt{2}}|\uparrow\uparrow\downarrow\rangle + \frac{1}{\sqrt{2}}|\downarrow\uparrow\uparrow\rangle \\ |\psi_3\rangle &= \frac{1}{\sqrt{3}}|\uparrow\uparrow\downarrow\rangle + \frac{1}{\sqrt{3}}|\uparrow\downarrow\uparrow\rangle + \frac{1}{\sqrt{3}}|\downarrow\uparrow\uparrow\rangle, \end{aligned} \tag{2.28}$$

with energies of $E_1 = 4.33843$, $E_2 = 4.44614$ and $E_3 = 4.5$, respectively (notice that the energy of the highest excited state is the same as that of an impenetrable system - simply the sum of the energy of each harmonic oscillator level up to $N$). We are now able to calculate spin densities by defining this quantity as

$$\rho_{\uparrow,\downarrow}(x) = \sum_{i=1}^{N} m^i_{\uparrow,\downarrow}\rho^i(x), \tag{2.29}$$

where $m^i_{\uparrow,\downarrow}$ is the probability of finding $\uparrow,\downarrow$ particles at the site $i$, as $\rho^i(x)$ is given by Eq. (2.6). In Fig. 2.6 we show the results for these densities in the ground state and the two excited states of the 2+1 system of fermions in a harmonic trap.

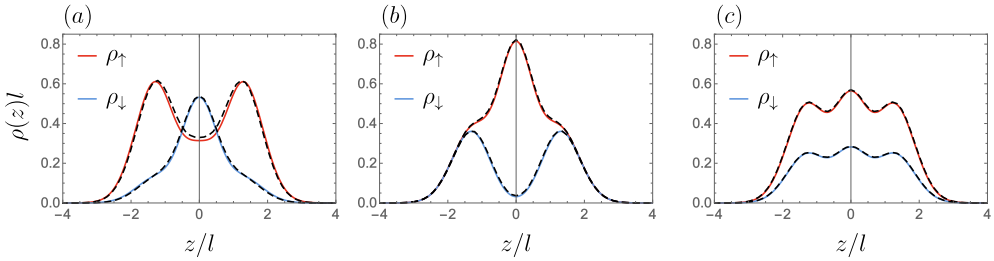


*Figure 2.6: Comparison between exact spin densities (solid colored curves) with numerical results obtained with OpenMPS (black dashed curves) for a) the ground state, b) the first excited state and c) the second excited state of a harmonically trapped 2+1 system.*

As expected (since the spin states are described by a Heisenberg chain), we see that the ground state has a dominating antiferromagnetic contribution, while in the first excited state the majority spins localize in the center of the trap. In the second excited state, we have a result that is frequently called a Heisenberg-type ferromagnetic state [52]. In this case, every spin has an equal probability of being at each site, and the densities are solely determined by the modulation of the spatial distributions. We also find good comparison between the exact results and the MPS results, specially in the excited states. We find an agreement of approximately 97% between exact and numerical approaches for the energies of each state. This is mainly due to an imprecision

in the approximation of the continuum with MPS, and can be improved by considering a larger number of sites in the Hubbard model (see Appendix A for details).

## 2.5 Experimental remarks

In this chapter and throughout the next sections, we assume that systems of strongly interacting cold atoms in effectively one-dimensional geometries can be produced in the lab, using a combination of sophisticated experimental techniques. In this section we comment on the technical details associated with these experimental procedures.

A first necessary feature of the systems we consider here is the low temperature. The methods involved in achieving the necessary temperature for experiments with cold atoms (tipically on the scale of 100 nK) date back to the creation of the first Bose-Einstein condensates [1, 2]. Usually, a combination of laser cooling [3] and evaporative cooling [4] is employed. In the first case, laser arrays with a frequency slightly below that of an atomic transition of the element are placed in opposite directions. Due to the Doppler effect, atoms moving towards the laser beams tend to absorb photons, since they experience a small increase in the laser frequency. If the recoil energy of reemission of these photons is below the initial kinetic energy of the atoms, the net effect of this process is a reduction of the total kinetic energy of a sample, which means the temperature is reduced. The basic idea behind evaporative cooling [11] is that the internal state of the atoms with larger kinetic energy is changed, such that the trapping potential no longer affects them. The atoms are then free to evaporate from the trap, leaving behind only atoms with a smaller kinetic energy, which also leads (after collisional processes) to a decrease in the sample's temperature.

Naturally, some of these methods already imply a detailed control over the confining potential. These traps are usually realized in terms of optical lattices, where counter-propagating laser beams create standing waves. The minima of these stading waves can then be used to create effective wells that confine the atoms. By combining counter-propagating waves in two or three directions, it is possible to create arrays of one-dimensional tubes or cigar-shaped traps - where the motion of the atoms is effectively one-dimensional - or even three-dimensional lattices (see Fig. 2.6 for a schematic depiction of these scenarios).

An additional factor which is decisive in the realization of experiments with trapped cold atoms is the control over interactions. A true interaction potential generally has a somewhat complicated form which is usually given by the Van der Waals force; at low energies, however, this interaction can be treated as an effective contact potential - described by a $\delta(\mathbf{r})$ function - with a strength that depends only on a parameter known as the three-

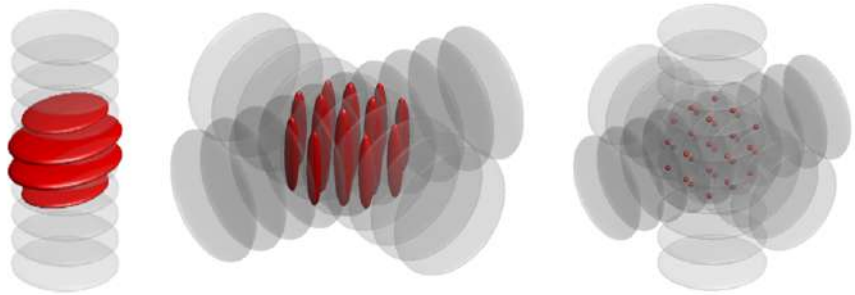

*Figure 2.7: Schematic depiction of the realization of a) two-dimensional pancake traps, b) effectively one-dimensional cigar-shaped traps and c) a lattice potential. Figure taken from Ref. [53].*

dimensional scattering length $a_{3D}$ [6]. This quantity can be controlled by exploring the phenomenon of Feshbach resonances [14]. These occur when the energy difference between a scattering channel and a bound state channel in a two-body interaction approaches zero. This effect can be manipulated with the action of magnetic fields, which leads to the possibility of changing the scattering length between atoms according to

$$a_{3D}(B) = a^0_{3D}\left(1 - \frac{\Delta}{B - B_0}\right) \tag{2.30}$$

where $B_0$ is the position of the Feshbach resonance, $\Delta$ is the energy separation between the open and closed channels and $a^0_{3D}$ is the scattering length in the abscence of magnetic fields. The relation between the coupling strength in three dimensions and the scattering length is given by

$$g_{3D} = \frac{2\pi\hbar^2 a_{3D}}{m}. \tag{2.31}$$

The application of a magnetic field thus allows for a tuning of the scattering length over a wide parameter space, resulting in different interactions in the attractive or repulsive regimes.

Another important development in the control of interactions between atoms trapped in optical lattices is the discovery of the so-called confinement-induced resonances (CIR). Let's assume a system that is trapped in a two-dimensional harmonic potential, where the longitudinal and transversal trapping frequencies are given by $\omega_\parallel$ and $\omega_\perp$, respectivelly. We also make $\omega_\parallel \ll \omega_\perp$, such that the motion of the atoms is effectively frozen in the transversal direction (this system is realized with the cigar-shaped traps in Fig. 2.7). We

then define the transversal oscillator length as $a_\perp = \sqrt{\hbar/m\omega_\perp}$, where $m$ is the atomic mass. It has been shown by Maxim Olshanii [15] that the one-dimensional coupling strength for this system is given by

$$g_{1\mathrm{D}} = \frac{2\hbar^2 a_{3\mathrm{D}}}{m a_\perp^2} \frac{1}{1 - \mathcal{C} a_{3\mathrm{D}}/a_\perp}, \tag{2.32}$$

where $\mathcal{C} = 1.0326$ is a constant which has been verified experimentally [54]. Notice that a resonance occurs for $a_\perp = \mathcal{C} a_{3\mathrm{D}}$, making the one-dimensional coupling infinitely large.

By combining the techniques described above, experimental physicists have been able to study a myriad of low-dimensional models in radically different interaction regimes. As examples, we have the Tonks-Girardeau [25, 26] and the Super Tonks-Girardeau [27] gases, which are obtained for infinitely strong repulsive and attractive interactions, respectively.

An ingredient which introduces an additional degree of complexity in these experimental realizations is the possibility of exploring the atomic hyperfine structure. Many of the early experiments realizing Bose-Einstein condensates employed single-component dilute vapors of alkali metals, such as Rubidium (Rb), Sodium (Na), Lithium (Li) and Potassium (K). Elements of this family are usually favored due to the simplicity of their electronic structure, where the outermost electron lies in a $s$- orbital.

The number of available internal states naturally depends on the choice of atomic element. In general, these states can be accessed and manipulated with radiofrequency or microwave pulses. As we have shown, when interactions between the atoms become really strong, we can treat our interactions in terms of spin permutations in one dimension, with the internal degrees of freedom now being interepreted as “pseoudospin" states. These hyperfine states are usually labelled as $|F, m_F\rangle$, where $F$ denotes the total spin (including the nuclear spin) and $m_F$ the spin projection on a chosen axis. An experiment with a two-component $^{87}$Rb gas, for instance, explores the $|F = 1, m_F = -1\rangle$ and $|F = 2, m_f = 1\rangle$ hyperfine states of this element [55]. Fermionic few-body experiments, on the other hand, tipically use $^6$Li fermions, with the hyperfine states defined by $|F = \frac{1}{2}, m_f = \frac{1}{2}\rangle$ and $|F = \frac{1}{2}, m_f = -\frac{1}{2}\rangle$ [28, 29]. The interactions between different components are usually tuned through Feshbach or confinement induced resonances, with the additional possibility of introducing imbalanced interactions is some particular cases [56].

Finally, recent experiments have been able to achieve multi-component 1D gases exploring the internal states of fermionic ytterbium ($^{173}$Yb) [36]. Here, the atoms have zero electronic spin, so the internal states are defined only by the nuclear spin. Since the interactions between atoms in different internal states are all equal, this fermionic system presents SU($N$) symmetry (with up to $N = 6$ is this particular realization). The possibility of exploring such a high number of interal states has led to the concept of “synthetic dimensions" [38], which has also been contemplated in experiments with $^{87}$Rb [37].

# Part II

# Dynamics in strongly interacting few-body systems

# Chapter 3

# Dynamical realization of magnetic states

Our first application of the formalism described in the previous part is the case of a few-body Bose gas, where the interactions can be dynamically tuned. Previous works have shown that a few-body one-dimensional Bose gas with two internal components can present the prototypical features of quantum magnetism [57]. Additionally, it has been shown that the intraspecies interactions have a decisive role in defining the magnetic properties of its ground state [52]. Here we focus on a system where the intraspecies interaction is slowly changed in time, and we calculate the dynamical spin densities of the system.

The following sections are based on the work published in Ref. [58]. With respect to the published paper, we have substantially modified this introduction and Sections 3.1 and 3.3 to remove redundant information regarding the definition of the system and general conclusions. Except for minor modifcations, Section 3.2 (including the figures) remains identical to the publication. The content of this chapter has also been presented as part of the Qualifying Exam.

## 3.1 Hamiltonian and initial state

We consider a trapped one-dimensional Bose gas with contact interactions and two different bosonic species $(\uparrow,\downarrow)$. The total number of particles is $N = N_\uparrow + N_\downarrow$ where $N_\uparrow$ and $N_\downarrow$ are the numbers of particles of species $\uparrow$ and $\downarrow$, respectively. The $N$-body Hamiltonian is given by Eq. (2.10), which, for convenience, we rewrite as

$$H = \sum_i^N H_0(x_i) + g\sum_{\uparrow\downarrow}\delta(x_i - x_j) + \kappa g\sum_{\uparrow\uparrow}\delta(x_i - x_j) + \kappa g\sum_{\downarrow\downarrow}\delta(x_i - x_j), \quad (3.1)$$

where we assume $\hbar = m = 1$ and

$$H_0(x) = -\frac{1}{2}\frac{\partial^2}{\partial x^2} + \frac{1}{2}\omega^2 x^2 \tag{3.2}$$

is the single particle Hamiltonian in a harmonic trap. The remaining terms of the Hamiltonian account for the contact interactions between particles of different species (with strength parameter $g$) and of the same species (with strength parameter $\kappa g$). We consider the length, time and energy units to be $l = \sqrt{\hbar/m\omega}$, $\tau = 1/\hbar\omega$ and $\hbar\omega$, respectively, where $\omega$ is the longitudinal harmonic confinement frequency. The units for the interaction parameter $g$ are given by $\hbar^2/(ml)$.

In the limit of infinite repulsion ($1/g = 0$), the solution of this system is given by the Bose-Fermi mapping, as shown previously. The energy of the system in this limit, $E_0$, is simply the sum of the energies of the lowest occupied energy levels of the potential $V(x)$. In the limit of strong interactions ($g \gg 1$), the Hamiltonian (3.1) can be mapped, up to linear order in $1/g$, to the spin chain given by Eq. (2.24). In the limit of $\kappa \to \infty$ and positive $g$ the identical bosons are infinitely repulsive, while for $\kappa = 1$, the interaction strength between all bosons is the same. In the particular case of $\kappa = 2$ we have an effective $XX$ model, as summarized in Ref. [46]. The spin model for bosons described in Ref. [59] can be obtained from Eq. (2.24) by performing a unitary transformation (see Supplemental Material of Ref. [50]). The coefficients $\alpha$ depend only on the geometry of the trap and are obtained from Eq. (2.19). We will mainly focus on the $N = 5$ problem, for which we obtain $\alpha_1 = \alpha_4 \approx 2.166$ and $\alpha_2 = \alpha_3 \approx 3.177$ (since the trap is symmetric, we have that $\alpha_i = \alpha_{N-i}$). Due to a factor of $1/2$ in the Hamiltonian, our geometric coefficients $\alpha_i$ are twice as large as the ones calculated in Ref. [52].

By taking Eq. (2.6) for the case of $N = 5$, we can calculate the spin densities for the imbalanced cases of three bosons of species $\uparrow$ and two bosons of species $\downarrow$ ($N_\uparrow = 3, N_\downarrow = 2$) and four bosons of species $\uparrow$ and one boson of species $\downarrow$ ($N_\uparrow = 4, N_\downarrow = 1$). To write the separate densities for components $\uparrow$ and $\downarrow$ we must combine the spatial and spinorial contributions; the density for component $\uparrow$, for instance, is given by $\rho_\uparrow(x) = \sum_{i=1}^{N} \rho_\uparrow^i(x)$ (Eq. (2.29)), where $\rho_\uparrow^i = m_\uparrow^i \rho^i(x)$. The value of $m^i$ for an eingenstate is found by exact diagonalization of Hamiltonian (2.24), where we consider $g = 100$. Since the total spin projection is conserved, we choose a truncated basis composed by $|\uparrow\uparrow\uparrow\downarrow\downarrow\rangle, ..., |\downarrow\downarrow\uparrow\uparrow\uparrow\rangle$ for the $N_\uparrow = 3, N_\downarrow = 2$ case and $|\uparrow\uparrow\uparrow\uparrow\downarrow\rangle, ..., |\downarrow\uparrow\uparrow\uparrow\uparrow\rangle$ for the $N_\uparrow = 4, N_\downarrow = 1$ case.

We now construct the initial states of the system by choosing the ground states in which the intraspecies interaction is smaller than the interspecies interaction ($\kappa = 0.1$). In Fig. 3.1 we show the spin densities for the imbalanced cases of $N_\uparrow = 3, N_\downarrow = 2$ and $N_\uparrow = 4, N_\downarrow = 1$. At this point, due to the difference in the interaction strengths, the species tend to separate in the trap. The densities profiles for $\kappa < 1$ show a ferromagnetic (FM) order [60] of the

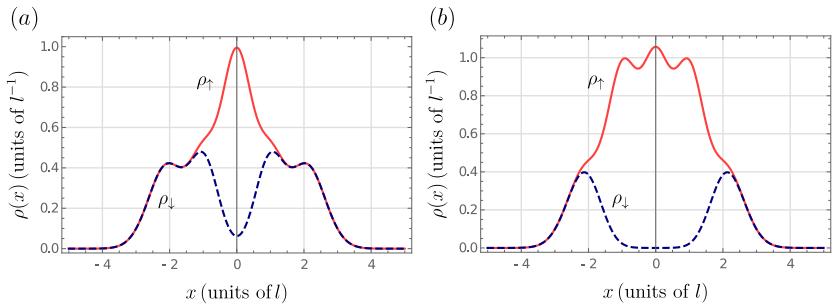


*Figure 3.1: Spin densities for the initial states, with $\kappa = 0.1$, for the (a) $N_\uparrow = 3, N_\downarrow = 2$ and (b) $N_\uparrow = 4, N_\downarrow = 1$ cases. The separation of different components in the trap indicates a FM behavior.*

Ising type (as opposed to the case where $\kappa = 1$, which will be addressed next). In panel $(b)$, we see a density that is similar to that of the Bose polaron [57], where a strongly interacting impurity is pushed to the edges of the system.

## 3.2 Dynamics

We now consider the time evolution of the system for a slow increase in the intraspecies interaction parameter $\kappa$. We take $\kappa$ varying in the interval $[0.1, 10.1]$. The eigenfunctions of the spin chain Hamiltonian thus evolve as

$$|\chi(t_f)\rangle = U(t_f, t_0)|\chi_0\rangle \tag{3.3}$$

where $U(t_f, t_0)$ is the time evolution operator and $|\chi_0\rangle$ is the initial state. Since the Hamiltonian is time dependent, we can break the time evolution in several steps

$$|\chi(t_f)\rangle = U(t_N, t_{N-1})...U(t_2, t_1)U(t_1, t_0)|\chi_0\rangle \tag{3.4}$$

increasing $\Delta\kappa = 10^{-5}$ and taking the Hamiltonian to be constant at each time step.

During the first steps of the time evolution ($\kappa \sim 0.1$) the change in energy at each step is larger than the energy gap $\Delta E$ between the ground state and the first excited state of Hamiltonian 2.24. This means that, initially, the evolution of the system is not adiabatic, although $\kappa$ is still slowly increasing. Therefore, the whole set of eigenvalues and eigenstates of the spin chain must be calculated for all times. The energy gap between the ground state and the first excited state of the spatial wave function, however, is given by $\hbar\omega \gg \Delta\kappa\hbar\omega$, so we can neglect the excited states of $\Phi(x_1, x_2, ..., x_N)$. The recursion formula for the time evolution of the spin wave function is then given by

$$|\chi_{i+1}\rangle = \sum_{i=1}^{\nu} c_n^{i+1} e^{-iE_n^{i+1}\Delta t}|\phi_n^{i+1}\rangle, \tag{3.5}$$

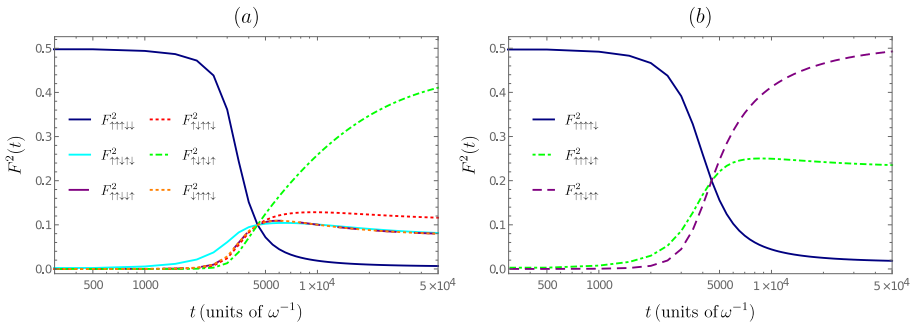


*Figure 3.2: Time evolution of the squared projection of the wave function over the initial state for (a) the $N_\uparrow = 3, N_\downarrow = 2$ and (b) the $N_\uparrow = 4, N_\downarrow = 1$ cases. In both figures, we disregard the projections over basis states that are symmetric and therefore show the same results. At $t = 0.45 \times 10^4\,[\tau]$, the system reaches the Heisenberg type FM state characterized by $\kappa = 1$, where the values for all the projections are the same.*

where $i$ denotes the time step, $E_n^{i+1}$ and $\phi_n^{i+1}$ are the eigenvalues and eigenvectors of the Hamiltonian 2.24 at step $i+1$, $c_n^{i+1} = \langle \phi_n^{i+1} | \chi_i \rangle$ and $\nu$ is the number of eigenstates (the total time evolution may be thought of as a succession of small quenches, with fixed $\Delta t = 0.05\,[\tau]$). In Fig. 3.2 we show the time evolution of the squared projection of the wave function over the initial state, $F_\xi^2(t)$, with $F_\xi(t) = |\langle \xi | \chi(t) \rangle|$, where $|\xi\rangle$ is some basis state (e.g. $|\xi\rangle = |\uparrow\uparrow\uparrow\downarrow\downarrow\rangle$ for the $N_\uparrow = 3, N_\downarrow = 2$ case).

In Fig. 3.3 we present the time evolution (up to $t = 1.5 \times 10^4\,[\tau]$) of the spin densities for the two imbalanced cases under consideration. We see that, for $0 < \kappa \leq 1$, the system evolves through a FM phase. This phase is characterized first by the separation of the two components in the trap and then (around $t = 0.45 \times 10^4\,[\tau]$ and $\kappa \sim 1$) by the typical densities of two-component bosonic systems with strong repulsive interactions [61]. For the particular case of $\kappa = 1$, all interactions are identical. The magnetic order is of the Heisenberg FM type with isotropic interactions, and the squared projections assume the same values for all basis states, as we can observe in Fig. 3.2. Notice the distinction between the profiles in this regime and in the Ising type FM regime of $\kappa < 1$. In Fig. 3.4 $(a)$ and $(b)$, we show the comparison between the slice at $t = 0.5 \times 10^4\,[\tau]$ (which corresponds to $\kappa = 1.1$), and the results obtained by exactly diagonalization of Hamiltonian 2.24 with $g = -100$ and $\kappa \to \infty$. In this limit, the densities reproduce the results expected for the strongly attractive two-component fermionic gas [52].

As the intraspecies interaction becomes stronger ($\kappa > 1$) an antiferromagnetic (AFM) profile starts to arise. This is seen in plots as the increase of the projections over the states $|\uparrow\downarrow\uparrow\downarrow\uparrow\rangle$ and $|\uparrow\uparrow\downarrow\uparrow\uparrow\rangle$ in Fig. 3.2. Finally, for $\kappa \gg 1$, the AFM profiles become more pronounced. In Fig. 3.4 $(c)$ and $(d)$, we compare the final densities at $\kappa = 10.1$ to the results obtained for $\kappa \to \infty$. The results in this case match the AFM states of strongly repulsive two-component

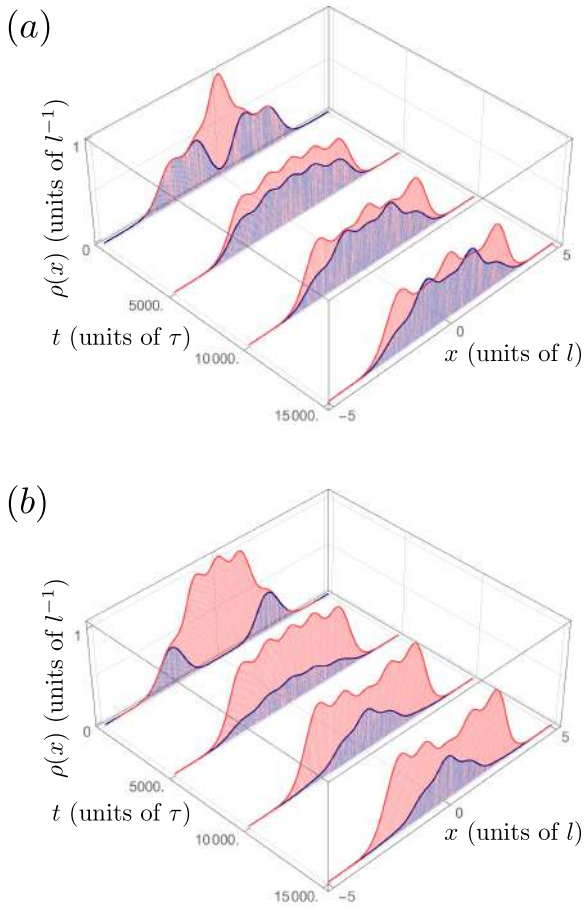


*Figure 3.3: Initial part of the time evolution ($t \leq 1.5 \times 10^4\,[\tau]$) of the spin densities for the cases of (a) $N_\uparrow = 3, N_\downarrow = 2$ and (b) $N_\uparrow = 4, N_\downarrow = 1$. Red and blue curves indicate $\uparrow$ and $\downarrow$ bosons, respectively. Initial profiles (up to $t = 0.5 \times 10^4\,[\tau]$) indicate FM states. At around $t = 10^4\,[\tau]$, AFM profiles start to arise.*

fermions. It is important to point out that while the spin densities may reproduce results of fermionic systems in certain limits, this may not be true for other correlations (e.g. the momentum distribution).

The total time evolution is given by $t_f = 0.5 \times 10^5\,[\tau]$. In current experimental setups, the inverse frequency $\tau$ is of the order of $100\mu$s [39]. This results in a total time of 5 seconds for the process we are considering, which is a relatively long time for experiments with ultracold atoms. We point out, however, that the transition from FM to AFM-like profiles is manifested early on in this time evolution. This means that these effects could conceivably be observed in smaller time intervals. Alternatively, increasing the trap frequency could lead to smaller time scales, where the increase in the interactions would take a shorter time.

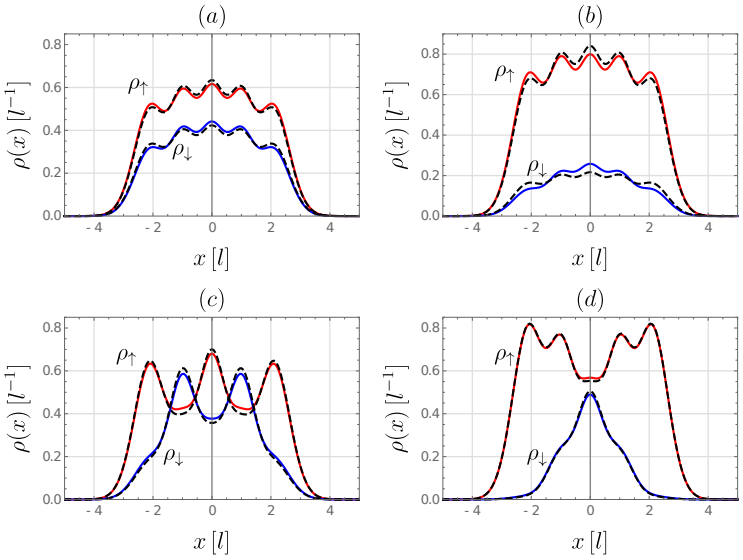


*Figure 3.4: Spin densities at $\kappa = 1.1$ compared to the results obtained with $g = -100$ and $\kappa \to \infty$ in the (a) $N_\uparrow = 3, N_\downarrow = 2$ and (b) $N_\uparrow = 4, N_\downarrow = 1$ cases. Final profiles ($t = 0.5 \times 10^5\,[\tau]$, $\kappa \sim 10$) of the bosonic system compared to the limiting case of $g = 100$ and $\kappa \to \infty$ for the (c) $N_\uparrow = 3, N_\downarrow = 2$ and (d) $N_\uparrow = 4, N_\downarrow = 1$ cases.*

### 3.2.1 Balanced System

We consider now a balanced system composed of $N_\uparrow = 2, N_\downarrow = 2$. Once again we choose an initial state where the intraspecies interaction is smaller than the interspecies interaction ($\kappa = 0.1$). In Fig. 3.5 (a), although a FM profile is still observed, there is no visible separation of components in the trap, due to the fact that the system is now balanced.

Since the probabilities of finding spin up and down bosons at each site are always the same, the spin densities do not change in time as $\kappa$ increases. However, the squared projections display a behavior analogous to that of the imbalanced cases, where the AFM states become dominant as $\kappa \to \infty$. Unlike the imbalanced cases, the AFM state for $N_\uparrow = 2, N_\downarrow = 2$ is composed by the linear combination of $|\uparrow\downarrow\uparrow\downarrow\rangle$ and $|\downarrow\uparrow\downarrow\uparrow\rangle$.

## 3.3 Conclusions

In this chapter we showed that different magnetic profiles can be obtained by dynamically changing the intraspecies interactions of a two-component strongly repulsive few-body bosonic gas. Due to the strong interactions, this model can be mapped to an effective spin chain with solutions that completely determine the state of the system. By slowly increasing the interactions between the identical bosons, we are able to keep the spatial densities fixed in the ground state, while the spin eigenstates evolve in time. The spin densities

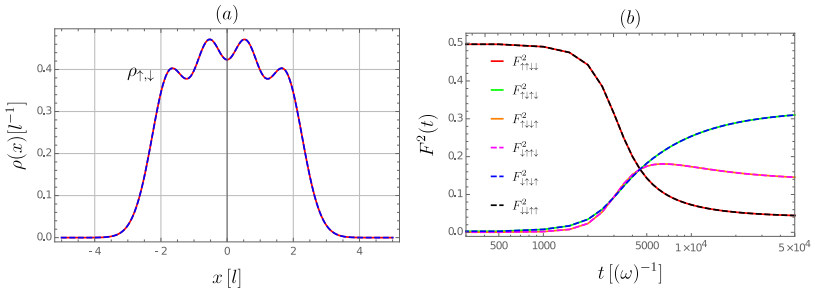


*Figure 3.5: (a) Spin densities for a balanced $N_\uparrow = 2, N_\downarrow = 2$ system. Due to the absence of imbalance in the number of atoms, there is no change in the spin densities as $\kappa$ is varied. (b) The squared projections display a transition from FM to AFM states similar to those observed in the imbalanced cases.*

then display a clear transition between ferromagnetic and antiferromagnetic profiles. In addition, during this evolution the system exhibits results that match the limiting cases of strong interspecies attraction or repulsion, depending only on the tuning of the parameter $\kappa$.

# Chapter 4

# Junction dynamics in a trapped system with an impurity

In this chapter we study a strongly interacting system composed of an impurity and a bosonic background in single- and double-well potentials. Different methods have been employed to study the many-body problem of bosons in a double-well, even outside the mean-field regime [62–66]. Addressing the subject from a few-body perspective [67–71], however, might lead to new insight on the properties of these systems. Here we show that, in the regime where the repulsion between the impurity and the background is dominant, the system can exhibit non-trivial dynamical effects: the impurity undergoes Josephson-like oscillations when initialized at the edge of the system, and can have its tunneling enhanced when a barrier is present. The persistent current oscilations that characterize a Josephson junction have been first predicted [72] and observed [73] in condensed matter systems with superconducting devices. Later, however, an analogous effects was shown to occur in ultracold bosonic systems in double-well geometries [74, 75]. The effects described here provide new perspectives in the study of spin state transfer and quantum transport in one-dimensional systems, and should be observable using current experimental techniques.

The content of this chapter has been published in Ref. [42]. With respect to the published paper, we have made substantial changes to the next two sections, where we have removed information that is already contained in Chapter 2. The last section, which was published as an Appendix in Ref. [42], was also been edited: with respect to the published material, we have kept only the relevant information on the single-particle solutions in the double-well. Except for minor modifications, the remaining part of the chapter and the figures have been kept identical to the original publication.

## 4.1 System description and Hamiltonian

We consider the problem of an impurity confined in the presence of a background of strongly interacting bosons. We assume the impurity is a boson in an internal state defined by $|\downarrow\rangle$, while the remaining identical bosons are described by $|\uparrow\rangle$. Consequently, all atoms have the same mass $m$. Two-component Bose gases can be realized experimentally using, for instance, $^{87}$Rb atoms in different hyperfine states, as described in Chapter 2. The number of identical bosons is given by $N_\uparrow$, while the total system size is $N = N_\uparrow + 1$. The Hamiltonian for this problem is given by Eq. (2.10), which we rewrite - to consider a single atom in the $|\downarrow\rangle$ state - as

$$H = \sum_{i=1}^{N} H_0(x_i) + g\sum_{i=1}^{N_\uparrow} \delta(x_\downarrow - x_{\uparrow i}) + \kappa g \sum_{i<j}^{N_\uparrow} \delta(x_{\uparrow i} - x_{\uparrow j}). \tag{4.1}$$

The coordinates are thus denoted by $x_\downarrow$ for the impurity and $x_{\uparrow i}$ for the remaining bosons. The interaction parameters are defined as in Chapters 2 and 3. The single-particle Hamiltonian in Eq. 4.1 is given by $H_0(x) = -\frac{\hbar^2}{2m}\frac{\partial^2}{\partial x^2} + V(x)$. Here, $V(x)$ is a double-well potential (see Fig. 4.1) expressed as $V(x) = \frac{1}{2}m\omega^2\left(|x| - \tilde{b}\right)^2$, where $\omega$ is the trapping frequency. The parameter $\tilde{b}$ denotes the displacement of the two minima of the wells with respect to the origin, and also defines the size of the barrier at this point as $V(0) = \frac{1}{2}m\omega^2\tilde{b}^2$. We then refer to $\tilde{b}$ as the "barrier parameter". By making $\tilde{b} = 0$ we naturally recover the harmonic single-well potential. Although this form of potential has analytical solutions in terms of parabolic cylinder functions [9], we obtain the single-particle wave functions and energies through numerical diagonalization (see 4.5).

We will focus on the behavior of the spatial distributions and the impurity dynamics in the repulsive case ($g, \kappa > 0$), for different choices of the intraspecies interaction parameter $\kappa$ and the barrier parameter $\tilde{b}$. While cases of attractive interactions ($g, \kappa < 0$) can in principle be explored, the properties of the system in this regime reproduce only highly excited states related to the so-called Super Tonks-Girardeau gas [27, 76]. Simulating the dynamics of systems with attractive interactions would likely require taking into account the formation of bound pairs, an effect which is beyond the scope of the formalism employed here. Throughout this chapter, we consider all quantities in harmonic oscillator units; therefore, length, energy and time are given in units of $l = \sqrt{\hbar/m\omega}$, $\hbar\omega$ and $\omega^{-1}$, respectively. While the intraspecies interaction parameter $\kappa$ is dimensionless, the parameter $g$ is considered in units of $\hbar^2/ml$. For simplicity, we also make the barrier parameter dimensionless by rescaling it as $b = \tilde{b}/l$. In our calculations, we set $g = 20$ and assume that $\hbar = \omega = m = 1$.

In the limit of strong interactions ($g \gg 1$), Hamiltonian 4.1 can be written, up to linear order in $1/g$, as the XXZ spin chain (2.24) with the appropriate

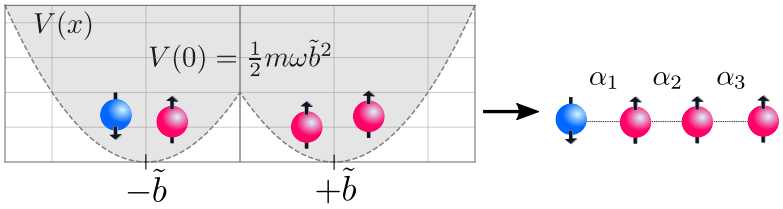


*Figure 4.1: Sketch of the 1D bosonic system with an impurity in the double-well potential. The parameter $\tilde{b}$ sets the position of the minimum of each well and also the size of the barrier between them at $x = 0$. In the limit of strong interactions, the system can be mapped to a spin chain where the coefficients $\alpha$ are determined by the shape of the trap.*

number of atoms in each species. The coefficients $\alpha_i$ are calculated using the wave function for a system of $N$ spinless fermions, which is constructed as the Slater determinant of the lowest occupied orbitals in the trap (see Section 4.5). The spatial part of the wave function for a bosonic system is obtained by means of the Fermi-Bose mapping. A comparative study of the spatial distributions for a strongly interacting few-body bosonic system in the double-well has been presented in Ref. [77].

## 4.2 Spin densities

To obtain the probability densities for each component in the system, we must combine the spatial distributions of the atoms in the trap with the probability of finding a given spin component at each site of the spin chain described by Eq. 2.24. The spin densities are calculated according to Eq.(2.29). The quantities $\rho_\downarrow(x)$ and $\rho_\uparrow(x)$ thus describe the spatial distributions of the impurity and the background bosons, respectively. In Fig. 4.2 a) we show the results for the spin densities of a 3+1 system for $b = 0$ (single-well) and $b = 2$ (double-well) at different values of the intraspecies parameter $\kappa$.

The cases where $b = 0$ correspond to the results expected for the harmonic trap, which have been broadly covered for bosonic and fermionic systems in previous works [33, 61, 78–80]. For $\kappa < 1$ the repulsion between the impurity and the background is larger than the background repulsion. This causes the impurity to be pushed to the edges of the system, which is an effect also found in the case of a weakly interacting background [60]. In this regime, the system exhibits Ising-type ferromagnetic correlations, and is characterized by a nearly degenerate ground state [52]. At $\kappa = 1$, all interactions are equal and the spin densities show the Heisenberg-type ferromagnetic profiles expected for isospin bosons [81]. In this case both distributions display the same characteristic Tonks-Girardeau spatial densities, but scaled to the number of particles in each species. When $\kappa > 1$, the repulsion between the background bosons dominates, and we observe predominantly antiferromag-

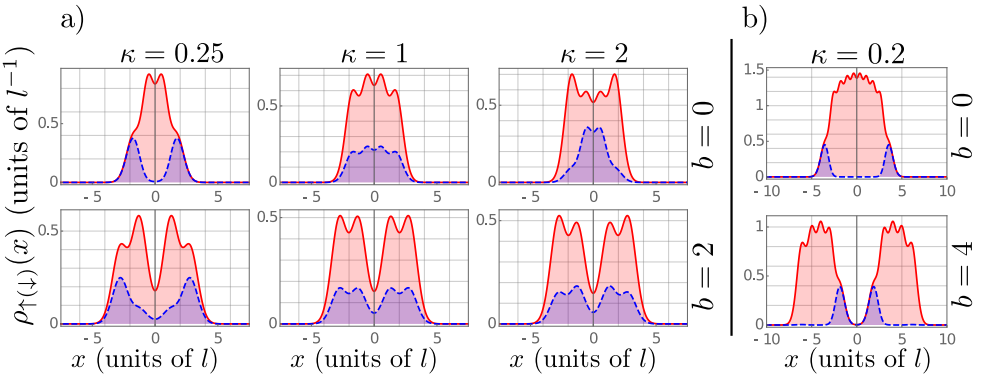


*Figure 4.2: a) Spin densities for the ground state of a 3+1 system at different values of the barrier parameter b and of the background interaction parameter $\kappa$ (the values for each panel are determined by the labels on the rows/columns). The red curve corresponds to the background density $\rho_\uparrow(x)$ while the blue curve corresponds to the impurity density $\rho_\downarrow(x)$. b) Spin densities for a 9+1 system at $\kappa = 0.2$ and two different choices of b. For a larger value of b, the impurity has a greater probability of being placed near the barrier, at the center of the system. The density for each component is normalized to its corresponding number of particles.*

netic correlations, where the impurity is placed near the center of the trap. These correlations for the system with a single impurity are in agreement with the results found for mixed systems in Chapter 3.

In the double-well potential, all densities are depleted in the center of the system, but this is not the only relevant effect. For the case of $\kappa < 1$ the impurity has now a larger probability of being near the center of the trap (as compared to the single-well case), since the background density is strongly reduced in this region. It is even possible to expect a configuration (specially for a larger number of background bosons) where the impurity is completely localized near the barrier between the wells (see Fig.4.2 b)). This effect is directly related to the imbalance in the numerical values of the geometrical coefficients at the edges and near the center of the system as $b$ is increased. For the cases of $\kappa = 1$ , again the impurity and the background densities have the same shape, aside from normalization. At $\kappa > 1$, we observe a similar configuration, with a small bias of the impurity toward the center of the trap.

## 4.3 Dynamics

We now turn to the dynamics of the impurity after being initialized at the left edge of the system. The corresponding spin state is therefore given by $|\downarrow\uparrow\uparrow\uparrow\rangle$. Since this is not an eigenstate of the spin chain, we can expect the spin state to evolve in time governed by Eq. (2.24), and we denote it by $|\chi(t)\rangle$. A thorough study of spin state transfer in traps of different shapes has been done by Volosniev *et. al.* in Ref. [46]. It has been shown [47, 82, 83] that

transfer is optimized by considering $\kappa = 2$ (which turns Eq. (2.24) into an XX Hamiltonian) with a set of exchange coefficients where $\alpha_j \propto \sqrt{j(N-j)}$. Here we focus on the tunneling times for the impurity between the wells (or between the left and right sides of the system in the case of a single well) when the background repulsion is smaller than the repulsion between the impurity and the background ($\kappa < 1$). We point out that, since we do not consider any other external perturbations, like trap or interaction quenches, we can assume that the spatial distributions remain in the ground state. This also allows us to consider only the manifold of Eq. 2.24 with lowest energy, as done in Chapter 3. To quantify the dynamics of the impurity, we calculate its average position as

$$\langle x_\downarrow(t)\rangle = \int \rho_\downarrow(x,t)\, x\, dx, \tag{4.2}$$

where $\rho_\downarrow(x,t)$ is the time dependent spin density calculated with the spin state $|\chi(t)\rangle$. When considering the regime of $\kappa < 1$, we observe that the projections of the initial wave function on the two-lowest eigenstates are dominant when compared to the case of higher excited states. This allows us to attempt a two-level description for the time evolution of the spin wave function; we thus write $|\psi(t)\rangle = c_g e^{-i\omega_J t}|g\rangle + c_e|e\rangle$, where $|g\rangle$ and $|e\rangle$ denote the two egeinstates of the spin chain with lower energy, and $c_g$ and $c_e$ are the projections of the initial wave function over these states. The frequency $\omega_J = E_e - E_g$ is given by the gap between the energies of the first excited state $E_e$ and the ground state $E_g$.

In Fig. 4.3, we present the results for $\langle x_\downarrow(t)\rangle$ in the single-well ($b = 0$) and double-well potentials ($b = 2$), with two choices of $\kappa < 1$, also showing a comparison with the two-level description in each of these cases. At $b = 0$, we notice that the motion of the impurity between the edges of the system is very well captured by the two-level approximation. This behavior clearly resembles the oscillations in population expected for a bosonic Josephson junction described as a many-body system in a double-well. In the present context, however, the barrier is composed by the repulsive background gas. We expect these results to hold even in the case of more than one impurity, provided that the system is imbalanced (that is, the background gas must have a larger number of particles). In this situation, an initial state decribed by the minority species completely localized at either side of the trap should have its time evolution governed mainly by the two lowest energy states. In the single-well case with weaker intraspecies interaction ($\kappa = 0.2$) the tunneling of the impurity is suppressed. Here, the the behavior of the background approaches that of an ideal Bose gas, where the atoms tend to “bunch up" in the center of the trap.

Now, comparing the single- and double-well cases, we see that, for $\kappa = 0.5$, the presence of the barrier slows down the tunneling of the impurity. Furthermore, we observe oscillations on a smaller scale, due to a larger overlap between the initial state and the excited states of the spin chain Hamiltonian.

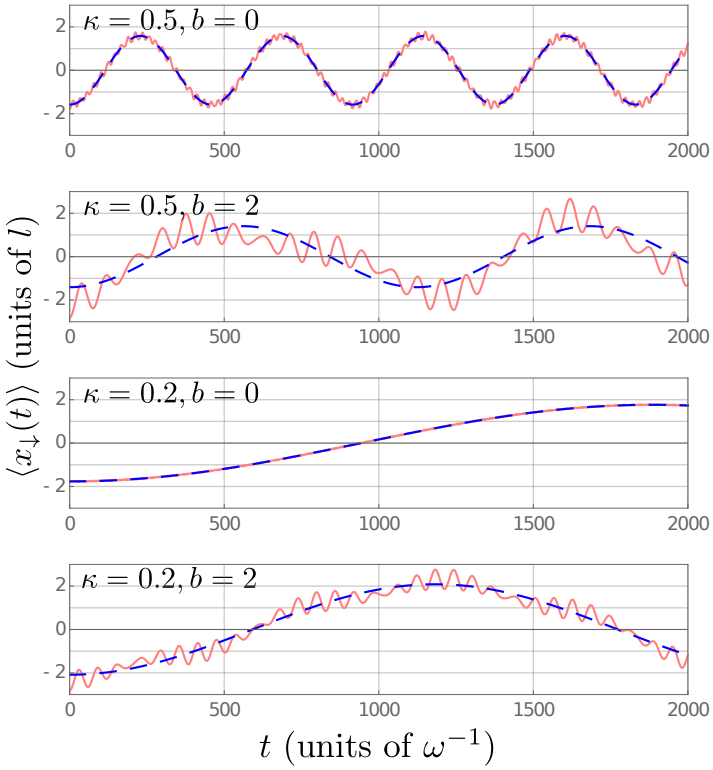


*Figure 4.3: Impurity average position as a function of time for different values of $\kappa$ and $b$. The solid red curves show the exact results, while the blue dashed curves are obtained with the two-level description (see text).*

At $\kappa = 0.2$, however, we get an enhanced tunneling of the impurity when considering a double-well as opposed to the single-well case. This effect has been also found with a different choice of double-well potential [46]. One might interpret it as a splitting of the background gas by the barrier in such a way that the impurity is able to tunnel through faster than it would in the absence of the barrier. However, if we consider a single-particle problem where an atom is initialized in the left well, it is clear that increasing the barrier size would only lead to exponential suppression in the tunneling frequencies. We therefore conclude that the accelerated tunneling observed in the regimes we consider is only possible due to the presence of the bosonic background, and thus constitutes a many-body effect.

To get an understanding of this behavior over a larger parameter space, we plot in Fig. 4.4 the energy gap between the ground state and the first excited state for several values of $\kappa$ and $b$. The non-monotonic behavior of the gap as a function of $b$ indicates that, for small $\kappa$, there is some choice of barrier size that increases that energy gap, and therefore enables a higher tunneling frequency between the wells. As $\kappa$ increases, however, we see that this behavior disappears and the presence of the barrier only reduces the gap,

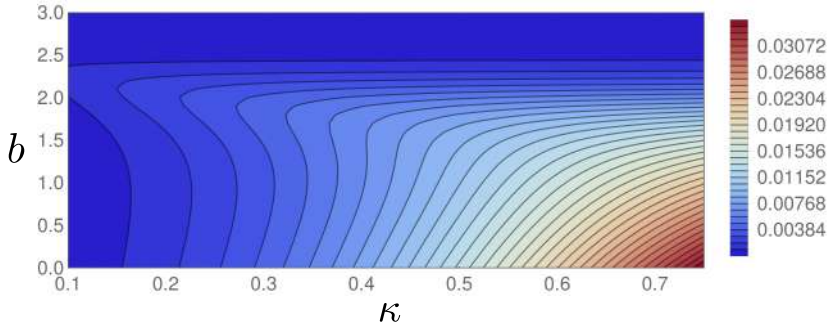


*Figure 4.4: Energy gap between the two lowest states of the spin chain for different values of the barrier parameter b and background interaction $\kappa$ for the 3+1 case.*

thus making the tunneling slower.

## 4.4 Increasing $N_\uparrow$

As a final example, we consider a case where we increase the number of background bosons to $N_\uparrow = 5$ (to observe similar effects as in the case of $N_\uparrow = 3$, we choose to maintain an even total number of atoms). The initial state is once again defined by the impurity placed at the left edge of the system, that is, $|\downarrow\uparrow\uparrow\uparrow\uparrow\uparrow\rangle$. We keep the intraspecies repulsion parameter fixed at $\kappa = 0.25$.

In Fig. 4.5 a) we once again show the results for the average position of the impurity as a function of time. For the single-well, the tunneling times are so long that the impurity is effectively frozen at the left edge of the system. In this case, an analogy can be drawn to the self-trapped regime in a few-body system as presented in Ref. [67]. For $b = 3$, however, we again notice that a faster motion of the impurity from the left to the right well is induced. The difference in the results with and without the barrier is even clearer than in the case of $N_\uparrow = 3$. This can also be seen in the energy gap between the two lowest states, as presented in Fig. 4.5 b): a very pronounced curve shows the increase in this quantity for small $\kappa$ and $b > 1$. We point out that the final time ($t = 10^4$ in units of $\omega^{-1}$) considered in the present case is five times larger than in the case of $N_\uparrow = 3$.

## 4.5 Single-particle solutions

In this section we present the solutions obtained with numerical diagonalization for the single-particle problem in a double-wel. The eigenvalues and eigenstates of a particle in a double-well were obtained through numerical diagonalization of the Hamiltonian $H_0$ using the 50 lowest states of the harmonic oscillator trap ($b = 0$) as basis. In Fig. 4.6 we present these solutions for different values of the barrier parameter $b$. In panel a), we show the the

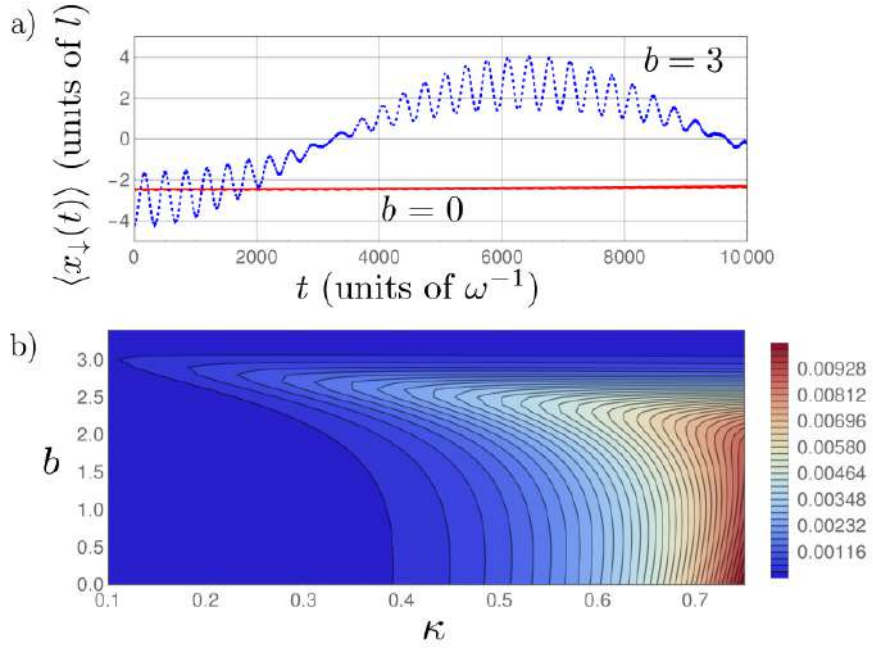


*Figure 4.5: a) Average position of the impurity as a function of time for the 5+1 case, in the single- ($b = 0$, red solid curve) and double-well ($b = 3$, blue dashed curve). The background interaction parameter is set as $\kappa = 0.25$. b) Energy gap between the two lowest states of the spin chain for different values of the barrier parameter $b$ and background interaction $\kappa$.*

eigenvalues obtained from numerical diagonalization and compare to results obtained from the open-source code CONAN [48] (we also use this tool to obtain the numerical values of the exchange coefficients $\alpha$ as the barrier parameter is increased). Notice how each pair of states becomes degenerate as the barrier size is increased. This is reflected in the eigenstates shown in panel b): at larger values of $b$, the ground state and the first excited state have the same probability distribution, differing only in parity.

## 4.6 Conclusions

In this chapter we have studied the static and dynamic properties of an impurity in the presence of a background of bosons in single-well and double-well geometries. The ground state spin densities are described by a combination of the spatial distributions in the limit of infinite repulsion and the eigenstates of a spin chain. We have shown that the dynamics of an impurity initialized at the left edge of the system displays oscillations similar to the ones observed in Josephson junctions. Additionally, for weaker background interactions, the tunneling of the impurity can in fact be enhanced by the introduction of a bar-

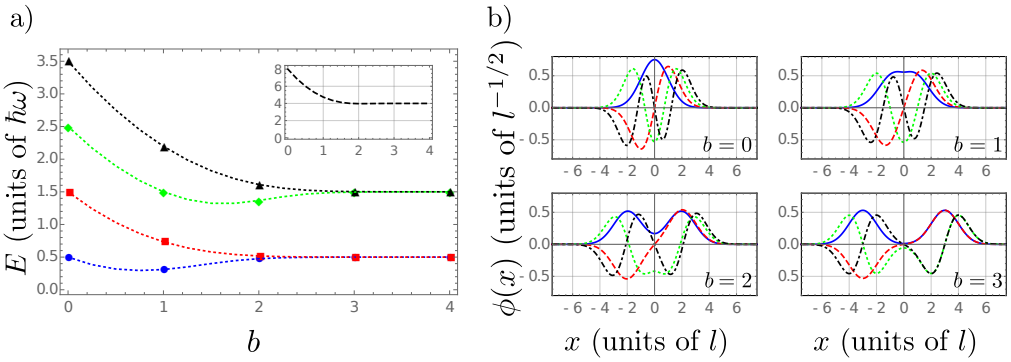


*Figure 4.6: a) Single-particle energies of the 4 lowest eigenstates of the double-well potential as a function of the barrier parameter b. The dotted curves show the results calculated with CONAN (see text), while the symbols are the values obtained by numerical diagonalization. The inset shows the energy $E_0$ of the spinless fermion wave function as a function of b for $N = 4$. b) The four lowest single-particle eigenstates for different values of the barrier parameter b. Solid blue, dashed red, dotted green and dot-dashed black curves correspond to ground state, 1st, 2nd and 3rd excited states, respectively.*

rier. This many-body effect is only possible in the presence of a background. We interpret it as the increase of the gap between the two lowest energy states, which governs the low-frequency dynamics of the system. Our results open new perspectives on the study of quantum transport in one-dimensional systems, hinting at the possibility of realizing a bosonic Josephson junction in the complete absence of an artificial barrier. Moreover, the inclusion and manipulation of double-well potentials and even lattices may allow for the optimized transfer of spin states.

# Chapter 5

# Effects of interacting imbalance in a Bose mixture

In this chapter, we focus on a yet unexplored regime of interactions in a one-dimensional strongly interacting Bose mixture. We show that, assuming an imbalance in the interaction between the two species it is possible to obtain radically different spatial correlations in a few-body system. Furthermore, we describe the dynamics of a mixture with imbalanced populations in this interaction regime. We observe that, for a certain combination of interactions, the minority species can travel through the system as an effective spin wave packet.

The content of this chapter has been published in Ref. [84]. With respect to the original publication, much of the Introduction has been removed to avoid redundance with the information provided in Chapter 2. Some of the definitions in the next two sections have also been replaced by references to equations described in Chapter 2. The interpretation of the results, the conclusions and the figures have been kept identical to the publication, except for minor modifications.

## 5.1 Hamiltonian

We consider the problem of a two-component Bose gas with population and interaction imbalance in an effective one-dimensional trapping geometry. We assume that the two different components consist of atoms of a same element, but in different hyperfine states. Therefore, the two bosonic species we take into account have the same mass $m$, but are defined by the states $|\uparrow\rangle$ or $|\downarrow\rangle$; the number of atoms in each species is respectively given by $N_\uparrow$ and $N_\downarrow$, with the total number of atoms written as $N = N_\uparrow + N_\downarrow$, as considered in Chapter 3. We are interested in the spatial distributions and the dynamics of an imbalanced mixture where a minority species with $N_\downarrow$ atoms interacts with the remaining $N_\uparrow$ majority atoms. The general Hamiltonian for this system,

considering contact interactions, is given by Eq. (2.10). Here, we conveniently rewrite it as

$$\begin{aligned} H = \sum_{i=1}^{N} H_0(x_i) \quad &+ \quad g_{\uparrow\uparrow} \sum_{i<j}^{N_\uparrow} \delta(x_{\uparrow i} - x_{\uparrow j}) \\ + g_{\downarrow\downarrow} \sum_{i<j}^{N_\downarrow} \delta(x_{\downarrow i} - x_{\downarrow j}) \quad &+ \quad g_{\uparrow\downarrow} \sum_{i}^{N_\uparrow} \sum_{j}^{N_\downarrow} \delta(x_{\uparrow i} - x_{\downarrow j}), \end{aligned} \tag{5.1}$$

where $H_0(x) = -\frac{\hbar^2}{2m}\frac{\partial}{\partial x} + V(x)$ is the single particle Hamiltonian with a trapping potential given by $V(x)$. In the following we consider energy units of $\epsilon = \hbar^2/(mL^2)$, where $L$ is the length of the trapping potential, and assume that $\hbar = m = 1$. We consider the general case of different intraspecies and interspecies interactions, that is $g_{\uparrow\uparrow} \neq g_{\downarrow\downarrow} \neq g_{\uparrow\downarrow}$. The particular case of $g_{\uparrow\uparrow} = g_{\downarrow\downarrow} = g_{\uparrow\downarrow}$ can be solved (for a homogeneous case) with the Bethe ansatz. In the limit of strong interactions ($g \gg 1$), the Hamiltonian (5.1) can be mapped (up to linear order in $1/g$) to an effective spin chain. Here, we write that expression in the most general case of different interactions between the components as [59]

$$H_s = E_0 - \sum_{i=1}^{N-1} \alpha_i \left( \frac{1}{g_{\uparrow\uparrow}} P_{1,1}^{i,i+1} + \frac{1}{g_{\downarrow\downarrow}} P_{1,-1}^{i,i+1} + \frac{1}{g_{\uparrow\downarrow}} P_{1,0}^{i,i+1} \right), \tag{5.2}$$

where $P_{S,M}$ denotes the projection operator on the two-particle eigenstates with total spin $S$ and magnetization $M$, while $E_0$ is the energy in the limit of infinite repulsion (see below). The exchange coefficients $\alpha_i$ are again determined by the trapping potential. Contrary to the previous chapters, in the next sections we will focus on a system trapped in an infinite square well of length $L$, where all coefficients $\alpha_i$ have the same constant value. We point out that the results for the spatial distributions shown in the next section also hold for the case of a harmonic trap. Since we consider the bosonic case where no interaction between atoms is forbidden by the Pauli principle, the two-body scattering happens in the triplet channel [59]

$$|1,1\rangle = |\uparrow\uparrow\rangle; \quad |1,-1\rangle = |\downarrow\downarrow\rangle; \quad |1,0\rangle = \frac{|\uparrow\downarrow\rangle + |\downarrow\uparrow\rangle}{\sqrt{2}}, \tag{5.3}$$

from which the projectors in Eq.(5.2) can be built as

$$P_{1,1} = \begin{pmatrix} 1 & 0 & 0 & 0 \\ 0 & 0 & 0 & 0 \\ 0 & 0 & 0 & 0 \\ 0 & 0 & 0 & 0 \end{pmatrix}, \; P_{1,-1} = \begin{pmatrix} 0 & 0 & 0 & 0 \\ 0 & 0 & 0 & 0 \\ 0 & 0 & 0 & 0 \\ 0 & 0 & 0 & 1 \end{pmatrix}, \; P_{1,0} = \frac{1}{2} \begin{pmatrix} 0 & 0 & 0 & 0 \\ 0 & 1 & 1 & 0 \\ 0 & 1 & 1 & 0 \\ 0 & 0 & 0 & 0 \end{pmatrix}. \tag{5.4}$$

Following the same reasoning, spin chains for bosons or fermions with a higher number of internal components can be constructed [85, 86]. By expanding

the projection operators in terms of the Pauli matrices [59], it is possible to reproduce a XXZ Hamiltonian (for $g_{\uparrow\uparrow} = g_{\downarrow\downarrow} \neq g_{\uparrow\downarrow}$) and the Heisenberg Hamiltonian with ferromagnetic correlations (for $g_{\uparrow\uparrow} = g_{\downarrow\downarrow} = g_{\uparrow\downarrow}$) [81].

## 5.2 Spatial distributions

We now focus on calculating the spatial distributions of a two-component bosonic system with population imbalance and arbitrary combinations of the interactions $g_{\uparrow\uparrow}, g_{\downarrow\downarrow}$ and $g_{\uparrow\downarrow}$. We point out that, while the interactions may be different, the spin chain approach only remains valid as long as we have $(g_{\uparrow\uparrow}, g_{\downarrow\downarrow}, g_{\uparrow\downarrow}) \gg 1$. Here, we calculate the densities for individual atoms in the trap and combine those results with the spin orderings obtained from the eigenstates of Eq. (5.2). Thus the spin densities are again defined by Eq. (2.29). We stress that this quantity depends on the spinless fermion wave function $\Phi_0(x_1, ..., x_i, ..., x_N)$, which is constructed as the Slater determinant of $N$ particles in the potential $V(x)$. In our case, those are simply the $N$ lowest eigenstates of the infinite square-well (the energy $E_0$, present in Eq. (5.2), is the sum of the energies of these orbitals). Since in these calculations we want to address a system that is slightly larger than in the previous chapters, and to avoid having to calculate multidimensional integrals, we obtain the single-particle densities from Eq. (2.8).

In Fig. 5.1 we show the results for the spin densities calculated for $N = 7$ atoms and different population imbalances: $N_\uparrow = 4, N_\downarrow = 3$, $N_\uparrow = 5, N_\downarrow = 2$, and $N_\uparrow = 6, N_\downarrow = 1$. We also consider different interaction regimes, which we define as: the Heisenberg ferromagnetic (HFM) regime ($g_{\uparrow\uparrow} = g_{\downarrow\downarrow} = g_{\uparrow\downarrow}$), the Ising ferromagnetic (IFM) regime ($g_{\uparrow\uparrow} = g_{\downarrow\downarrow} < g_{\uparrow\downarrow}$), the antifferomagnetic regime (AFM) ($g_{\uparrow\uparrow} = g_{\downarrow\downarrow} > g_{\uparrow\downarrow}$) and the completely imbalanced (IMB) regime ($g_{\downarrow\downarrow} < g_{\uparrow\downarrow} < g_{\uparrow\uparrow}$). Each of these cases corresponds to a column in Fig. 5.1: in the column defined by panels $(a), (e)$ and $(i)$, we observe the results for the HFM regime of identical interactions, where the distributions are the same, only scaled to the number of particles in the specific component. The profiles show ferromagnetic correlations of the Heisenberg type, which are expected for isospin bosons [81]. Column $(b), (f), (j)$ show the IFM case where the intraspecies interaction is smaller than the interspecies interactions. This regime is characterized by a phase separated distribution, typical of an Ising ferromagnet. In column $(c), (g), (k)$ we present the AFM case where the intraspecies interactions are larger than the interspecies interactions. Here, we observe that antiferromagnetic correlations arise, being particularly visible in the slightly imbalanced case of panel $(c)$. Finally, we consider in column $(d), (h), (l)$ a completely imbalanced regime (IMB), where $g_{\downarrow\downarrow} < g_{\uparrow\downarrow} < g_{\uparrow\uparrow}$. Here, we see that we again obtain phase-separated profiles, except that now the minority atoms sit in the center of the trap. This happens because the minority intraspecies interactions are smaller and the net result is an effec-

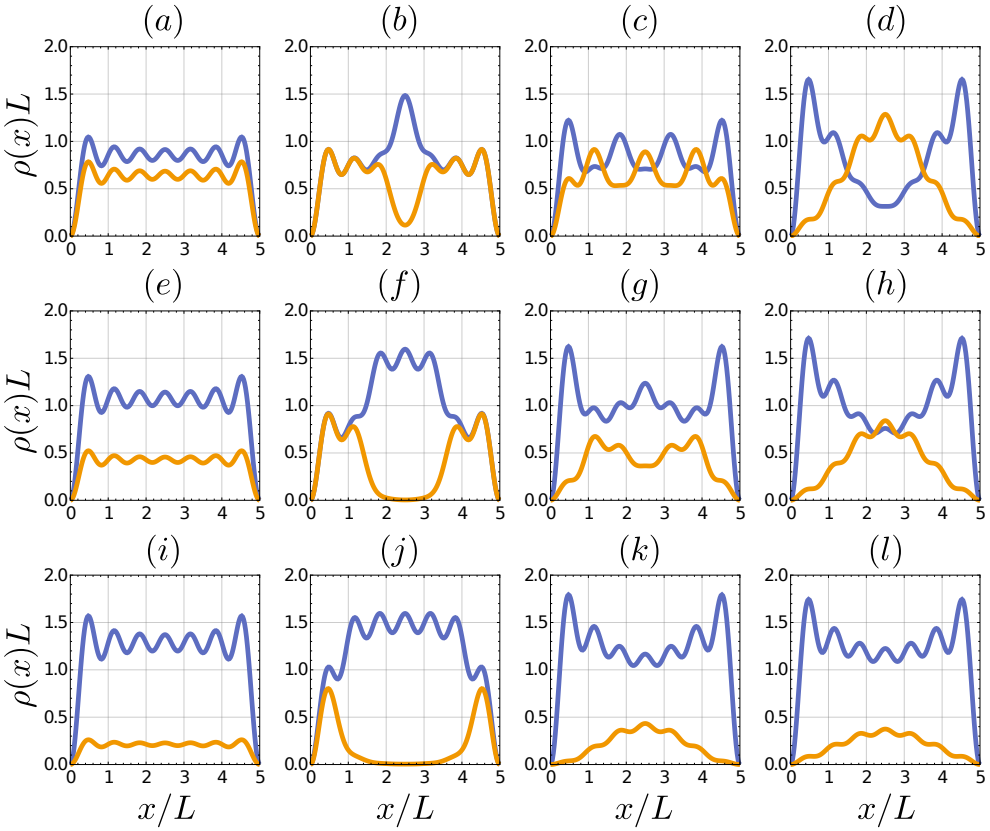


*Figure 5.1: Spin densities for a system with $N = 7$ and (a)-(d) $N_\uparrow = 4, N_\downarrow = 3$, (e)-(h) $N_\uparrow = 5, N_\downarrow = 2$, (i)-(l) $N_\uparrow = 6, N_\downarrow = 1$. The blue curves show the densities $\rho_\uparrow(x)$, while the yellow curves show $\rho_\downarrow(x)$. Each column describes an interaction regime (see text): $(a), (e), (i)$ HFM ($g_{\uparrow\uparrow} = g_{\downarrow\downarrow} = g_{\uparrow\downarrow}$); $(b), (f), (j)$ IFM ($g_{\uparrow\uparrow} = g_{\downarrow\downarrow} < g_{\uparrow\downarrow}$); $(c), (g), (k)$ AFM ($g_{\uparrow\uparrow} = g_{\downarrow\downarrow} > g_{\uparrow\downarrow}$) and $(d), (h), (l)$ IMB ($g_{\downarrow\downarrow} < g_{\uparrow\downarrow} < g_{\uparrow\uparrow}$). The density for each component is normalized to the number of particles.*

tively attractive regime for this component. We note that these distributions resemble the $XY$ phase described in a Bose-Fermi mixture [87]. The evident similarity between the last two panels $(k)$ and $(l)$ stems from the fact that in both cases there is only one minority particle. Therefore, the intraspecies interaction in this case has no effect on the minority spin density.

## 5.3 Dynamics

We now turn to the dynamics of the system in the case of population and interaction imbalance. We choose to analyze the two cases of $N_\uparrow = 5, N_\downarrow = 2$ and $N_\uparrow = 4, N_\downarrow = 3$, with interactions strength ratios set as $g_{\uparrow\downarrow} = 3g_{\downarrow\downarrow}$ and $g_{\uparrow\uparrow} = 5g_{\downarrow\downarrow}$. The case of a single minority spin in different interaction regimes and trapping potentials has been studied in Ref. [46, 47]. We will show that,

in the imbalanced regime, non-trivial effects for the dynamics of the minority species can arise. The system is initialized in the state where the minority species is placed at the left side, that is $|\psi(0)\rangle = |\downarrow_1 \ldots \downarrow_{N_\downarrow} \uparrow_1 \ldots \uparrow_{N\uparrow}\rangle$. We disregard any external excitations to the system, such that the dynamics can be described completely by Eq. (5.2). The time unit of the system is related to the energy scale as $\tau = \hbar/\epsilon$. We calculate the time-dependent overlap of the wave function with a state $|s\rangle$ defined by a given spin ordering as

$$F_s(t) = |\langle s|e^{-iH_S t}|\psi(0)\rangle|^2. \tag{5.5}$$

In Fig. 5.2 we show the results for the cases of $(a)$ $N_\uparrow = 5, N_\downarrow = 2$ and $(b)$ $N_\uparrow = 4, N_\downarrow = 3$. We focus only in the cases where $|s\rangle$ denotes a state where the minority spins are "bunched up" the system, e.g. $|\downarrow\downarrow\uparrow\uparrow\uparrow\uparrow\uparrow\rangle$, $|\uparrow\downarrow\downarrow\uparrow\uparrow\uparrow\uparrow\rangle$, and so on.

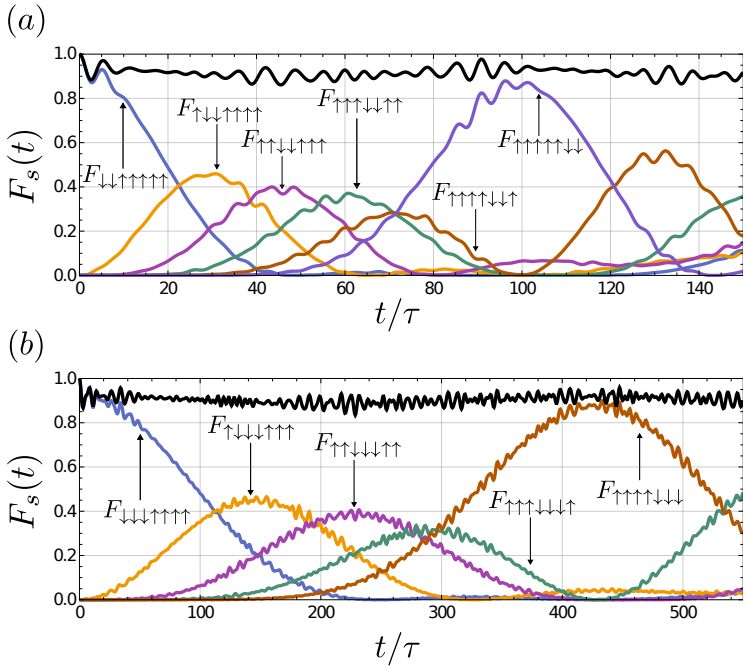


*Figure 5.2: Time evolution of the overlap probabilities $F_s(t)$ for the population imbalances $(a)$ $N_\uparrow = 5, N_\downarrow = 2$ and $(b)$ $N_\uparrow = 4, N_\downarrow = 3$, in the regime where $g_{\downarrow\downarrow} = g_{\uparrow\uparrow}/5 = g_{\uparrow\downarrow}/3$. Each curve shows the projection over a state with a different spin ordering, as indicated by the arrows. The black curves show the sum of the projections over all states $|s\rangle$.*

We clearly observe in both imbalanced cases that the minority spins, initialized in the left, travel through the system together, with higher amplitudes for the projections over the states with the minority at the edges. We also show the sum of the projections over all states $|s\rangle$, which nearly amounts to unity at all times, indicating that other spin orderings have little influence on

the dynamics. The physical interpretations for this phenomenon comes from the fact that the majority interactions are dominating with respect to the remaining two parameters. This leads to a regime where the minority atoms behave as if under the effect of an attractive force. While this combination of strongly imbalanced interactions may be hard to achieve in practice, it is possible to devise a scenario where the majority strongly repulsive bosons are replaced by a Fermi gas. Bose-Fermi mixures have been studied under the same formalism applied here [87], and could present similar dynamical effects.

## 5.4 Conclusions

We have studied the effects of imbalance in the spatial correlations and dynamics of a strongly interacting two-component Bose gas. The results for spin densities reproduce the expected behavior in the known regimes of ferromagnetic and antiferromagnetic correlations. Furthermore, the completely imbalanced case can present non-trivial spatial distributions that are not found in other regimes. The dynamics of the system is also affected by the population and interaction imbalance. We demonstrated that, given a certain choice of interaction parameters, a minority population initialized at the edge of the system can move around as if bound by an effectively attractive force.

Our work suggests that setups where the interactions can be tuned between different species may be ideal for studying the transfer of spin packets. Such a realization could provide knowledge of quantum transport in spin chains beyond the case of a single impurity. By generalizing the spin chain approach to a higher number of internal components, it is also possible to consider cases of mixed multicomponent systems with different interactions in several scattering channels.

# Chapter 6

# Dynamics in a few-body spin chain with external driving

In the previous chapters, we have worked with Hamiltonians which are static or slowly changing in time. However, from an experimental point of view, out-of-equilibrium systems, which respond in certain ways under the action of external driving, can be a source of interesting new physical effects. To be able to treat systems with time-dependence, we can employ different tools, such as the Crank-Nicolson method for the time evolution of discretized wave functions [88] (see Appendix A) and Floquet theory [89] for periodic Hamiltonians.

This chapter is dedicated to using these tools to describe the time evolution of the wave function in a spin chain under the action of external driving. This study is mostly dedicated to comparing methods and understanding how they relate to each other. The physical system under consideration is a small spin chain with a periodic driving in one of the exchange coefficients. We analyze the behavior of the response frequencies of the system for different interactions using both the numerical approach and a treatment based on the Floquet quasienergies of the periodic Hamiltonian. Generalizing our results for a wide range of driving frequencies, we are able to understand how subharmonic frequencies arise as a response to the external driving.

The proposal for the system considered in this chapter and the interpretation of the results were done in collaboration with O. V. Marchukov and A. G. Volosniev.

## 6.1 System description

We consider a spin-1/2 XXZ Hamiltonian described by

$$H(t) = -\sum_{i=1}^{N-1} J_i(t) \left[ \frac{1}{2}(1 - \vec{\sigma}^i \cdot \vec{\sigma}^{i+1}) + \Delta(1 + \sigma_z^i \sigma_z^{i+1}) \right], \tag{6.1}$$

where $\sigma_x, \sigma_y, \sigma_z$ are the Pauli matrices, $J_i(t)$ are the exchange coefficients for each pair of first neighbors, which can have a general time-dependence, and $\Delta$ is a dimensionless anisotrpy parameter that sets the imbalance in the interactions between spins with the same orientation. We choose to explore this spin Hamiltonian due to the similarities with the physical systems we have described so far. The number of spins in each component is given by $N_\uparrow$ and $N_\downarrow$, with the total number of spins being $N = N_\uparrow + N_\downarrow$. We consider a few-body system composed of $N_\uparrow = 3$ and $N_\downarrow = 1$, with different choices of $\Delta$. Generally speaking, for $\Delta \ll 1$, we approach a Heisenberg Hamiltonian, where antiferromagnetic correlations are dominating in the ground state of a homogeneous systems ($J_1 = J_2 = J_3$). The most probable configurations is then given by the down spin placed near the center of the chain. In the case of $\Delta > 1$, the interaction between spins with different orientations dominates, and the ground state is similar to that of an Ising ferromagnet, where the down spin is pushed to the edges of the system. This regime is additionally characterized by a quasidegeneracy between the ground and first excited states [52], a feature that plays an important role in the dynamics of these systems.

In the next calculations, the units for frequency and time are $J_0/\hbar$ and $(\hbar J_0)^{-1}$. Additionally, we make $\hbar = 1$ for simplicity.

## 6.2 Dynamics in the presence of periodic driving

We now explore the dynamics of a system governed by the Hamiltonian described above, when one of the exchange coefficients $J_i(t)$ has a periodic behavior in time. We first describe the basic elements of Floquet theory that we apply to the problem, and then compare the results with a numerical approach.

### 6.2.1 Floquet analysis

The Floquet theorem [89] states that, for a periodic Hamiltonian $H(t) = H(t+T)$, where $T$ is the period, solutions of the form

$$|\Psi_n(t)\rangle = \exp\left(-i\epsilon_n t/\hbar\right)|u_n(t)\rangle \tag{6.2}$$

exist, where $|u_n(t)\rangle = |u_n(t+T)\rangle$ are time-periodic functions called Floquet modes, and $\epsilon_n$ the corresponding Floquet quasienergies. The Floquet modes can be obtained by solving the following eigenvalue equation

$$\mathcal{H}(t)|u_n(t)\rangle = \epsilon_n|u_n(t)\rangle, \tag{6.3}$$

where $\mathcal{H}(t) = H(t) - i\hbar\partial/\partial t$. Alternatively, we can consider the action of the time evolution operator on the wave function over one period [90, 91]

$$U(t+T)|\Psi(t)\rangle = |\Psi(t+T)\rangle, \tag{6.4}$$

and inserting the decomposition on the Floquet modes in the expression above we obtain

$$U(t+T)|u_n(t)\rangle = \exp\left(-i\epsilon_n T/\hbar\right)|u_n(t)\rangle, \tag{6.5}$$

since $u(t+T) = u(t)$. This shows that the Floquet modes are eigenstates of the time evolution operator over one period. By diagonalizing $U(T,0)$, we can obtain the quasienergies and Floquet modes at $t = 0$, and then calculate them at time $t$ as

$$|u_n(t)\rangle = \exp\left(i\epsilon_n t/\hbar\right)U(t,0)|u_n(0)\rangle. \tag{6.6}$$

To obtain $U(t,0)$, we numerically solve

$$i\hbar\frac{\partial}{\partial t}U(t,0) = H(t)U(t,0) \tag{6.7}$$

with initial condition $U(0) = \mathbf{1}$. The time evolution of the wave function, for an initial state $|\Psi(0)\rangle$, is then given by

$$|\Psi(t)\rangle = \sum_n c_n \exp\left(-i\epsilon_n t/\hbar\right)|u_n(t)\rangle, \tag{6.8}$$

where $c_n = \langle u_n(0)|\Psi(0)\rangle$.

### 6.2.2 Comparison to numerical results

Upon initializing the system in the corresponding ground state of each regime (with a given value of $\Delta$ and $J_2(0) = 1$), we obtain the dynamics for a periodic driving of the central coefficent given by $J_2(t) = \frac{1+\cos(\omega_D t)}{2}$, where $\omega_D$ is the driving frequency. This makes $J_2$ oscillate between 1 and 0 with period $T = 2\pi/\omega_D$, while the remaining exchange coefficients are fixed as $J_0 = 1$. The Schrödinger equation is numerically integrated using the Crank-Nicolson method (see Appendix A). We choose as a suitable observable the probability of finding the down spin at the edges of the system, that is $P(t) = |\langle\downarrow\uparrow\uparrow\uparrow|\Psi(t)\rangle|^2 + |\langle\uparrow\uparrow\uparrow\downarrow|\Psi(t)\rangle|^2$. In Fig. 6.1 we show the time evolution of this quantity for driving frequencies of $\omega_D = 2$ and $\omega_D = 5$, with different choices of the anisotropy parameter $\Delta$.

As we see, in all cases the time evolution obtained with the numerical method agrees well with the results from Floquet theory. The initial values of $P(t)$ depend heavily on the choice of $\Delta$: for $\Delta < 1$, the down spin is initially localized near the center of the system, and moves outwards as the central exchange coefficient is reduced. The opposite is true for $\Delta > 1$. For a lower driving frequency (left column) the oscillations in $P(t)$ tend to have a larger amplitude at smaller values of $\Delta$, which is not possible for larger $\omega_D$ (right column). More interestingly, for larger values of $\omega_D$ and $\Delta$ it is possible to see the emergence of a response frequency on $P(t)$ which is smaller than the driving frequency (this is made clear by comparing the colored curves to the grey shaded area in the background). To find the relationship between the

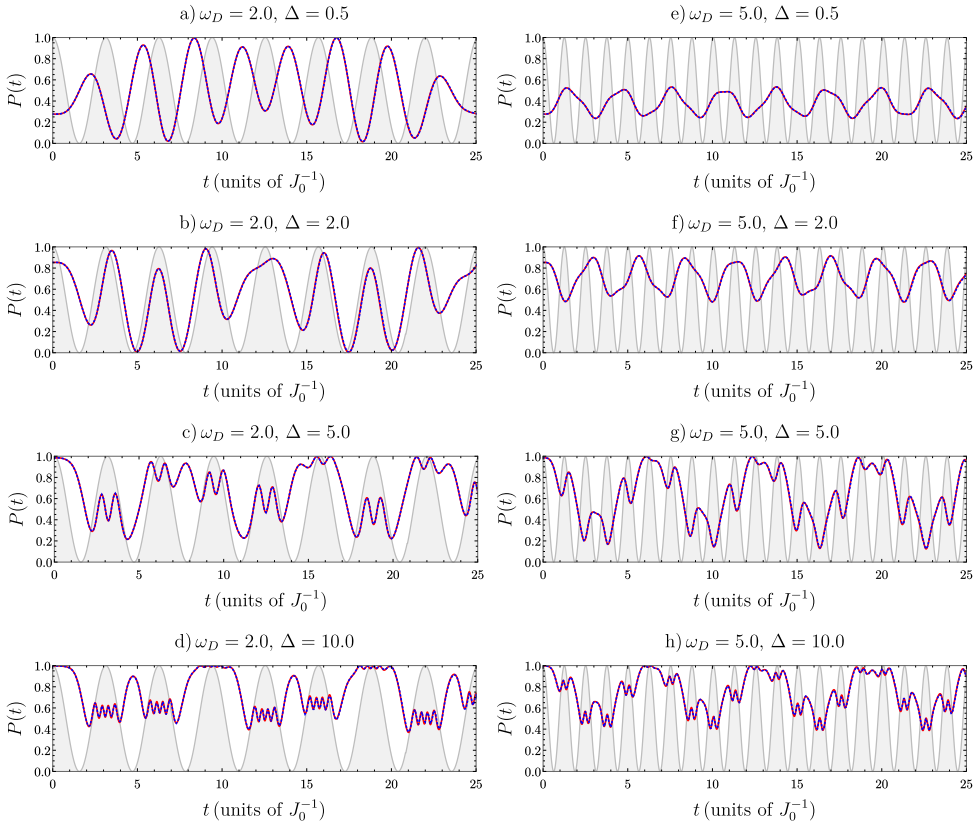


*Figure 6.1: Time evolution of $P(t)$ for different choices of the interaction anisotropy parameter: a)-d) show the cases where $\omega_D = 2$ and e)-h) with $\omega_D = 5$. The values of $\Delta$ are indicated in each panel. Red solid lines show the results obtained with the Floquet mode decomposition, while the blue dashed curves present the numerical results. The grey shaded curvex show the variation of $J_2(t)$ for the same interval of time.*

response and the driving over a larger frequency interval, we calculate the power spectrum for $P(t)$, defined as

$$S(\omega_R) = \Big| \int P(t) e^{-i\omega_R t} dt \Big|^2, \tag{6.9}$$

where $\omega_R$ is the response frequency, which is also considered in units of $J_0/\hbar$. In Fig. 6.2 we show the results for $S(\omega_R)$ with $\omega_D$ given by the interval $(0, 5)$, with increments in the driving frequency of $\delta\omega_D = 0.1$.

The two top panels show results for a) $\Delta = 0.5$ and b) $\Delta = 2.0$, while the bottom panels correspond to $\Delta = 5.0$ and $\Delta = 10.0$. In the top two, we see that the response frequency for slow driving is linear, which we could expect by considering the result from an adiabatic variation of the coefficients. However, in both cases the response quickly saturates to a fixed value, which can be predicted by considering the time evolution of $P(t)$ for a quench of the central

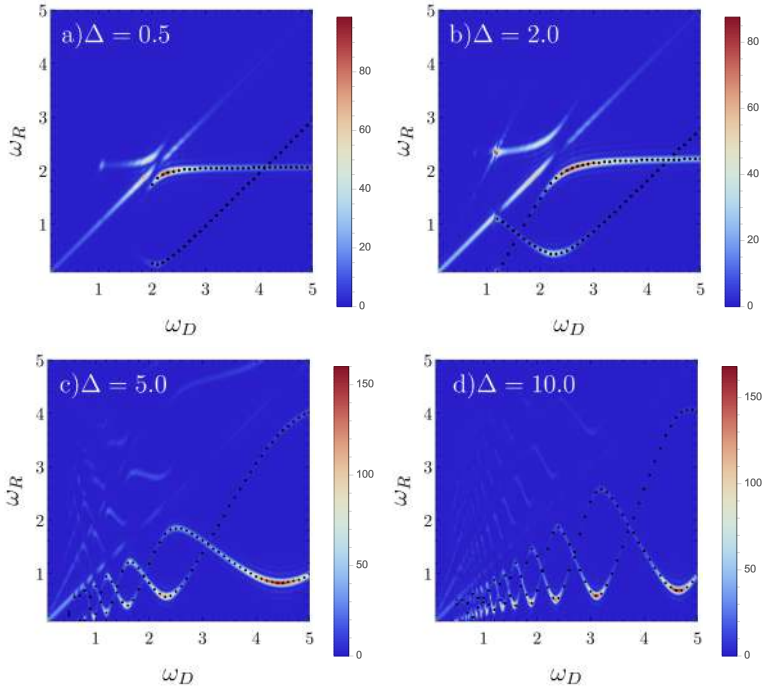


*Figure 6.2: Power spectrum $S(\omega_R)$ for a) $\Delta = 0.5$, b) $\Delta = 2.0$, c) $\Delta = 5.0$ and d) $\Delta = 10.0$. The white/red areas show the position of the peaks in $S(\omega_R)$ for a given driving frequency $\omega_D$. The black dots show the expected values for these frequencies according to the gaps in the Floquet quasienergy spectrum (see text for details).*

coefficient to the time-averaged value of the driving (that is, by switching $J_2$ from 1 to 0.5 at $t = 0$). This means that for smaller values of $\Delta$, the system quickly becomes non-responsive to fast driving frequencies. Moreover, the subsequent time evolution can be obtained by simply considering the time-average of the Hamiltonian over one period.

For larger $\Delta$, however, we obtain a different behavior: the reponse of the system is linear only for very small values of $\omega_D$, and the dominating peaks in the response frequency are always found below the diagonal, which characterizes a subharmonic response. We further compare the results for $S(\omega_R)$ obtained with the numerical time evolution with the prediction given by the Floquet quasienergies, as described in the previous section. By decomposing the inital wave function $|\Psi(0)\rangle$ in the Floquet modes $|u_n(t)\rangle$, we find that at all times $t$ only two of these modes dominate the time evolution. The corresponding quasienergies are thus given by $\epsilon_0$ and $\epsilon_1$. The position of the subharmonic peaks is obtained by simply calculating $\Delta\epsilon = |\epsilon_1 \pm \epsilon_0|$. These gaps are indicated by the black dots in Fig. 6.2. We point out that, while the subharmonic modes are easily predicted by these gaps, their amplitudes can be radically different. In fact, in some cases the smaller peaks are completely washed out by the dominating excitations. Furthermore, the numerical simu-

lations show also the existence of higher harmonics in the response frequency which are not directly captured by the quasienergy gaps.

## 6.3 Conclusions

In this chapter we have performed a study of a few-body spin chain under the action of an external periodic driving. We defined a driving protocol and calculated the response in an observable of choice. Since the Hamiltonian is periodic in time, we can apply Floquet theory to obtain the time evolution of the wave function and compare to numerical results. We find that both approaches match well over a wide range of driving frequencies and with different interaction parameters. Furthermore, the gaps in the quasienergy spectrum allow us to predict the position of the excitation peaks in the response frequency of the system.

While the model we considered here is not applied to a physical problem in particular, several possible realizations of driven spin chains can be devised, either in cold atomic setups or with superconducting circuits. Having these tools will thus help us obtain the properties of other systems with time-periodic Hamiltonians, as we will see in the next chapter.

# Chapter 7

# Spin-charge separation in strongly interacting multicomponent few-body systems

An effect of particular interest, in the context of one-dimensional systems, is the phenomenon known as spin-charge separation, where the degrees of freedom related to the mass ("charge") and spin components can be described independently. This effect is well-captured by the celebrated Tomonaga-Luttinger Liquid (TLL) model [92], originally proposed in the context of interacting electrons in one dimension. Theoretical descriptions of spin-charge separation usually explore this model [93] or assume weakly interacting many-body Fermi [94] or Bose [95] mixtures. The strongly interacting regime, however, is where this effect is expected to manifest itself more dramatically, with the freezing of the spin degrees of freedom as compared to the charge dynamics [96]. Additionally, the possibility of describing a strongly interacting mixed system as an effective spin chain [46, 59, 78, 80, 86] presents a landscape where the separation of spin and charge arises naturally in a dynamical context [97, 98].

Experimentally, ultracold atomic setups are good condidates for simulating a Tomonaga-Luttinger liquid [99–101] and measuring spin-charge separation in detail. Unlike experiments in condensed matter, ultracold atomic ensembles usually allow for a fine tuning of the interactions and the trapping geometries, as well as a precise control over the number of atoms [30]. However, while spin-charge separation has been observed in quantum wires [102], measurements with cold atoms are restricted to static signatures[103] and a dynamical measurement remains elusive [104].

In this chapter, we present an analysis of the dynamics of a strongly interacting few-body system of fermions with SU($N$) symmetry after a sudden

change - a *quench* - in the trapping potential. Recently, systems of cold atoms in optical lattices with SU(3) and SU(4) symmetries have been explored theoretically [105, 106]. We begin by assuming the formalism used to describe a system of strongly interacting atoms in a trap, where the Hamiltonian can be mapped into a spin chain with position-dependent exchange coefficients. We then describe the quench protocol, which essentially consists of changing the trap from a split well (where we assume a gaussian barrier in the center of the system) to a simple harmonic well (see Fig. 7.1 for a sketch of this protocol). The ground-state configuration for these two systems is considerably different, and by changing the potential we can expect a non-trivial time evolution in the spin and charge sectors. Initially we describe the effect of the quench in the spatial sector and its consequences on the spin chain dynamics. By combining the dynamics of both sectors, we can extract the signatures of spin-charge separation from the oscillations frequencies of the system, showing how this effect can be observed in few-body ensembles, even as the number of internal components is increased. Moreover, we show that for a completely balanced system (where each atom is in a different internal state) the spin signature vanishes, and the excitation spectrum is analogous to that of a gas of impenetrable bosons. Finally, we explore a case where SU($N$) symmetry is broken and obtain the resulting effects on the dynamics of the system.

Multi-component cold atomic ensembles with strong interactions are currently within experimental reach [36] and often exhibit exotic dynamical effects, such as edge states[37, 38]. In these systems, the internal states of the atoms can be manipulated with laser pulses, and the behavior of each component can be measured with precision. Studying cold atoms with different internal symmetries in a highly controllable environment can lead to insight on particle physics models and even shed light on the validity of unification schemes [107].

The content of this chapter has been taken from Ref. [108]. With respect to the original material, we have substantially changed this introduction and Section 7.1 to avoid redundant information. Except for minor changes, Sections 7.2 and 7.3 and the figures throughout the chapter remain identical to the original work.

## 7.1 System description

Our goal is to describe the dynamics of a strongly interacting few-body system with internal ("pseudospin") degrees of freedom. We focus our description on a fermionic system, but the formalism is equally valid for bosons with the correct adaptations to the Hamiltonian. We consider initially an SU(2) system, where the internal degrees of freedom are labeled by $|\uparrow\rangle$ and $|\downarrow\rangle$, as in the previous chapters. Later we will generalize our approach to systems with higher symmetries. We denote the particle numbers in each species as

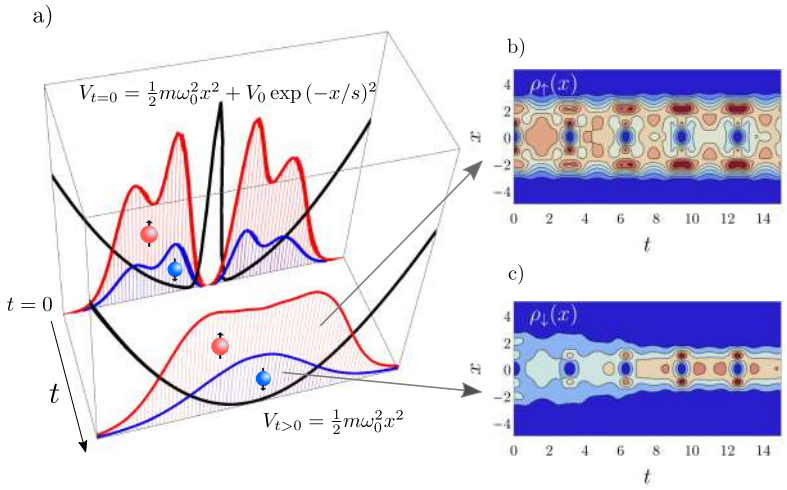


*Figure 7.1: a) Sketch of the quench protocol adopted in this work. An imbalanced ($N_\uparrow = 3$, $N_\downarrow = 1$) strongly interacting two-component system of atoms is initialized in the ground state of a harmonic potential modified by a gaussian bump centered at $x = 0$. For $t > 0$ this perturbation is suddenly switched off, which induces a dynamical behavior in the spin density of each component. The majority (minority) density $\rho_{\uparrow(\downarrow)}(x)$ is shown in red (blue). The black curves, which are rescaled for clarity, show the shape of the trapping potential at $t = 0$ and $t > 0$. b)-c) Time evolution of the spin densities, where length and time are given in units of the harmonic potential (see text for details). The slices shown in a) correspond to $t/T_0 = 0$ and $t/T_0 = 5$ in the figures on the right.*

$N_\uparrow$ and $N_\downarrow$, the total number of particles thus being given by $N = N_\uparrow + N_\downarrow$. For simplicity, we adopt the notation $N_\uparrow + N_\downarrow$ (e.g. 3+1 for a system with three particles of species $|\uparrow\rangle$ and one of species $|\downarrow\rangle$). Experimentally, two-component fermionic systems can be realized by preparing trapped ensembles of $^6$Li atoms in their two lowest hyperfine states [29, 39].

The Hamiltonian for the system under consideration is given by

$$H = \sum_i^N H_0(x_i) + g\sum_{\uparrow,\downarrow}\delta(x_i - x_j) \tag{7.1}$$

where $H_0(x) = -\frac{\hbar^2}{2m}\frac{\partial}{\partial x} + V(x)$ denotes the single particle Hamiltonian, where $V(x)$ is a trapping potential. The remaining term accounts for the contact interactions, where atoms in different internal states interact with strength $g$ (interactions between atoms in the same internal state are forbidden due to the Pauli principle, thus the difference with respect to Hamiltonian (2.10)). Since we are dealing with atoms of the same element in different internal states, we consider all masses equal. We use the same harmonic trap units as in the previous chapters.

### 7.1.1 Strong interactions

In the limit of strong interactions Eq. (7.1) can be written, up to linear order in $1/g$, as [86]

$$H = E_0 - \sum_{i=1}^{N-1} \frac{\alpha_i}{g}(1 - P_{i,i+1}), \tag{7.2}$$

where $P_{i,i+1}$ is the permutation operator, which exchanges two neighboring atoms of different components. When all interations between atoms in different internal states are the same, the system obeys SU($N$) symmetry.

The exchange coefficients are again determined by geometry of the trapping potential, and can be calculated as given in Eq. (2.19). In the particular case of SU(2) fermions, the permutation operator can be written as $P_{i,i+1} = \frac{1}{2}(1 + \vec{\sigma_i} \cdot \vec{\sigma_{i+1}})$, thus giving

$$H = E_0 - \frac{1}{2}\sum_{i=1}^{N-1} \frac{\alpha_i}{g}(1 - \vec{\sigma_i} \cdot \vec{\sigma_{i+1}}), \tag{7.3}$$

which is a Heisenberg Hamiltonian with ground state antiferromagnetic correlations. Obtaining the eigenstates of Eq. (7.3), we can calculate the spatial distributions of each atomic component in the trap using Eq. (2.29). Since we are interested in calculating the exchange coefficients and spin densities dynamically, we also use of Eqs. (2.8) and (2.26) to avoid calculating multidimensional integrals at each time step.

## 7.2 Dynamics

### 7.2.1 Quench protocol

In this section we describe the procedure that induces the dynamical evolution of the system, which consists of a sudden change of the trapping potential. Our initial choice of $V(x)$ is given by a harmonic trap with an additional gaussian bump in the center, as described by

$$V_{t=0}(x) = \frac{1}{2}\omega_0^2 x^2 + V_0 e^{-(x/s)^2}, \tag{7.4}$$

where $V_0$ determines the height of the gaussian peak and $s$ sets its width. The system is therefore separated in an effective double-well by taking $\omega_0 = 1$, $V_0 = 50$ and $s = 0.25$. The initial spinless fermion wave function $\Phi(x_1, ..., x_N, t = 0)$ is constructed with the single particle orbitals obtained by numerical diagonalization, using the $N_s = 35$ lowest energy states of the harmonic oscillator. We note that, since the gaussian peak is large compared to the individual densities of the orbitals, the ground state is quasi-degenerate (the two lowest energy states have nearly the same distribution, with opposite parity).

For $t > 0$, the peak is suddenly turned off by making $V_0 = 0$. The time evolution of the spinless fermion wave function can then be described in terms of the evolution of the single particles orbitals under the same quench protocol [109, 110]. We describe the dynamics of the orbitals $\phi_j(x, 0)$ according to

$$\phi_j(x,t) = \sum_{n=1}^{N_s} c_n e^{-i\epsilon_n t}\psi_n(x) \tag{7.5}$$

where $c_n = \int \psi^*(x)\phi(x,0)\,dx$ and $\psi_n(x)$ are the eigenstates of the harmonic oscillator, with $\epsilon_n$ the corresponding eigenvalues. We are then able to construct $\Phi(x_1, ..., x_N, t)$ for all times $t$, which in turn determines the time-dependence of the exchange coefficients in Eq. (2.19). In the next section we describe the time evolution of the spatial densities and its influence on $\alpha_i$.

### 7.2.2 Time evolution of charge density and geometrical coefficients

The $N-1$ exchange coefficients of the spin chain Hamiltonian given in Eq. (7.3) are determined, after the quench protocol, by $\Phi(x_1, ..., x_N, t)$. As a general rule, we can assume that the exchange coefficients are proportional to the overlap between the single particle distributions (as calculated by Eq.(2.6)); additionally, since the trapping potentials are symmetric at all times, we have $\alpha_3(t) = \alpha_1(t)$ for the case of $N = 4$ particles. In Fig. 7.2 a) we show the time evolution of the spatial densities obtained from $\Phi(x_1, ..., x_N, t)$. At this point, we are not considering the spin sector, so the densities shown correspond to the "charge" density

$$\rho_c(x,t) = \sum_{i=1}^{N} \rho^i(x,t), \tag{7.6}$$

which is normalized to the total number of particles. Its dynamical behavior is what should be expected for the coherent density oscillations of a Tonks-Girardeau gas [109]. In panel b), we see the behavior of $\alpha_1(t)/g$ and $\alpha_2(t)/g$ as a function of time (we consider a fixed value of $g = 20$ in our calculations). We observe that the periodicity of the spatial densities is reflected in the dynamics of the exchange coefficients. Particularly, since the system is approximately split in two parts at $t = 0$, we have that $\alpha(t = 0) \sim 0$ (there is nearly no overlap between the initial densities at the center of the system). When the densities in the central region become larger, we see that the numerical value of $\alpha_2(t)$ surpasses that of $\alpha_1(t)$.

Given the established time-periodicity of Hamiltonian (7.3), we can now analyze the dynamics of the spin sector using Floquet theory (see Chapter 6). While most studies performed in this context must deal with the issue of thermalization due to the external driving [111], in our case the time-dependence of the spin chain originates directly from the dynamics of the charge sector

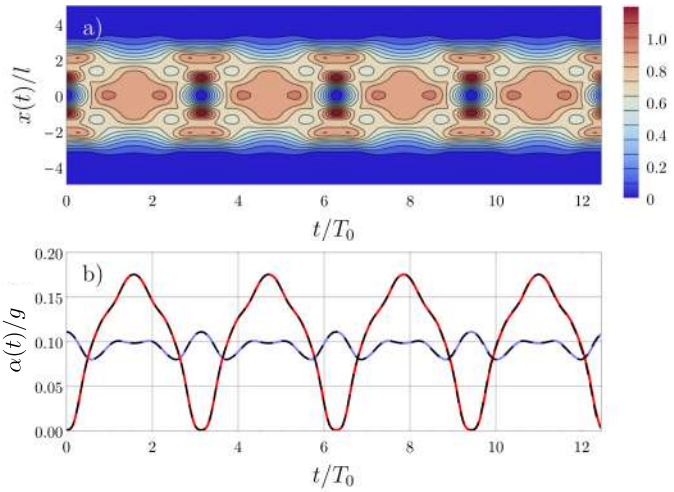


*Figure 7.2: Time evolution of a) the charge density $\rho_c(x,t)$ and b) the exchange coefficients $\alpha_1(t)$ (blue) and $\alpha_2(t)$ (red). Since the trapping potential is spatially symmetric at all times, we have $\alpha_3(t) = \alpha_1(t)$. In b), the black dashed curves show the analytical results obtained with an analytical fit of the numerical data with a Fourier expansion.*

generated by the sudden change of the trapping potential. To describe the time evolution of the system in these terms, we first find an analytical fit of the exchange coefficients in terms of Fourier modes. In Fig. 7.2 b), this approximation is shown as the black dashed curves.

### 7.2.3 Signatures of spin-charge separation

Once we know the time-dependence of Eq. (7.3), we can calculate the time evolution of an initial state of the spin chain, which we call $|\chi_0\rangle$. We numerically integrate the Schrödinger equation for this time-dependent Hamiltonian using the Crank-Nicolson method [88] (see Appendix A). Our quantities of interest are the dynamical charge ($\rho_c(x,t)$) and spin densities ($\rho_\uparrow(x,t)$ and $\rho_\downarrow(x,t)$), as well as the squared average density width of each spin component, defined as $\langle x^2_{\uparrow,\downarrow}(t)\rangle = \int dx\, \rho_{\uparrow\downarrow}(x,t)\, x^2$.

#### SU(2)

We choose initially a fermionic 3+1 case, which can be interpreted as a few-body Fermi background in the presence of an impurity, a system also known as the Fermi polaron [71]. As we will show next, in this simple setup it is already possible to find a signature of spin and charge separation in the time evolution of the observables. The ground state of Hamiltonian (7.3) with repulsive interactions ($g > 0$) has antiferromagnetic correlations, and can be

described by

$$|\mathrm{gs}\rangle = |{\downarrow}{\uparrow}{\uparrow}{\uparrow}\rangle + \left(1+\sqrt{2}\right)\left(|{\uparrow}{\uparrow}{\downarrow}{\uparrow}\rangle - |{\uparrow}{\downarrow}{\uparrow}{\uparrow}\rangle\right) - |{\uparrow}{\uparrow}{\uparrow}{\downarrow}\rangle, \tag{7.7}$$

aside from a normalization factor. Here, we have assumed a homogeneous potential, such that the exchange coefficients are identical and equal to 1. However, it can be shown that similar results hold for a harmonic trap. To observe how the ground state correlations change with the choice of $\alpha_i$, we define the operator

$$P_{\mathrm{edge}} = |\langle{\downarrow}{\uparrow}{\uparrow}{\uparrow}|\mathrm{gs}\rangle|^2 + |\langle{\uparrow}{\uparrow}{\uparrow}{\downarrow}|\mathrm{gs}\rangle|^2, \tag{7.8}$$

which gives us information regarding the position of the impurity (the $\downarrow$ atom) in the system. In Fig. 7.3 we show the values of $P_{\mathrm{edge}}$ for different choices of $\alpha_1$ and $\alpha_2$, where we assume a potential that is symmetryc across the origin, such that $\alpha_3 = \alpha = 1$ (this is true for the harmonic potential, for example).

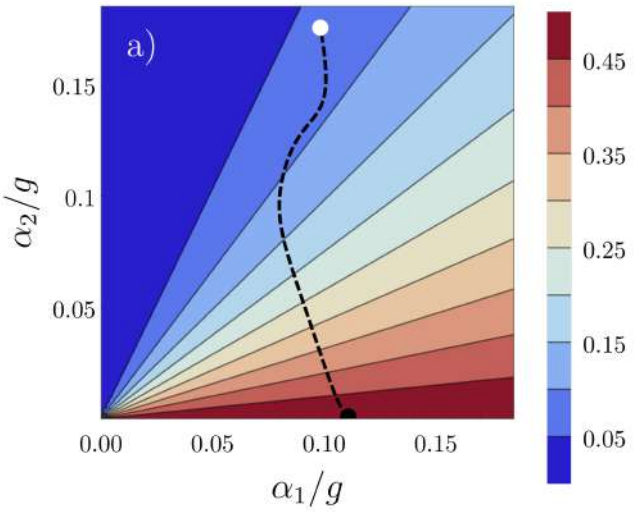


*Figure 7.3: Numerical values of $P_{edge}$ for different combinations of $\alpha_1$ and $\alpha_2$. The black dashed curve corresponds to the trajectory of the exchange coefficients in time after the trap quench. The initial point is marked by the black dot, while white dot marks the values of the exchange coefficients at $t = T_0/2$.*

We can readily see that, for $\alpha_1 = \alpha_2$, we have a constant result of $P_{\mathrm{edge}} = \frac{1}{4}(2-\sqrt{2})$, which is obtained by the normalized probabilities calculated from the coefficients in Eq. (7.8). Above the diagonal ($\alpha_2 > \alpha_1$) we have the region that includes, for instance, the coefficients obtained from a harmonic trap. In this case, the antiferromagnetic correlations are even more prevalent. If, however, $\alpha_2 \ll 1$, we have a larger probability of finding the impurity at the edges. These ground state correlations are obtained when considering a potential such as the one in Eq. (7.4). In fact, we can plot the trajectory of

the exchange coefficients after the quench in the trapping potential described in the previous section. This is shown by the dashed curve in Fig. 7.3. The white dot denotes the values at $t = 0$; the curve is then travelled back and forth periodically as $t$ increases. The fact that this trajectory crosses over the diagonal indicates that the sudden quench in the potential should induce major changes in the spin correlations of the system.

To quantify this effect we can calculate the dynamical spin densities $\rho_{\uparrow,\downarrow}(x,t)$, as well as the squared width of each component, given by $\langle x_{\uparrow,\downarrow}(t)\rangle^2$. It is important to notice that, for $t > 0$, the trapping potential is that of a simple harmonic oscillator. In Fig. 7.1 b) and c), we show the time evolution of $\rho_{\uparrow}(x,t)$ and $\rho_{\downarrow}(x,t)$, respectively. We notice that, while the underlying dynamics seen in Fig. 7.2 is still present, we now have an additional mode related to the spin dynamics. Specifically, after the sudden change in the potential, we observe a tendency of the majority atoms to spread to the edges, while the impurity localizes towards the center.

In Fig. 7.4 a) we show the time evolution of the squared widths $\langle x(t)^2_{\uparrow,\downarrow}\rangle$ for the density of each component, over a larger time interval. This can be interpreted as induced "breathing modes" for the background and the impurity. Additionally, we show the dynamical behavior of the charge density (Eq. (7.6)). Besides corroborating the results found in the time evolution of the densities, these curves show how the excitations in the charge and spin sectors are captured as two oscillations modes in each individual density. In Fig. 7.4 b) and c) we show the Fourier transform of $\langle x^2(t)\rangle$, defined as $\tilde{x}^2(\omega) = \int dt e^{-i\omega t}\langle x^2(t)\rangle$, where the contributions of the spin and charge excitations appear as two separate peaks, the lower frequency corresponding to the spin dynamics.

Here, we can see that the dynamics of the minority component is strongly dominated by the spin excitations, with a small contribution of the charge sector. On the other hand, the majority component has a more balanced distribution of oscillations in the charge and spin sectors. In Fig 7.4 b) and c), we additionally include the theoretical predictions for the charge and spin density oscillations (as black and gray dashed lines, respectively). The first is obtained by simply calculating the time-periodicity of 7.5. The second is extracted by calculating the gaps in the Floquet spectrum of the time-periodic spin chain (as done in Chapter 6). In the next sections, we show how increasing the number of internal components will affect the behavior of these quantities.

### SU(3)

We now consider a case of a three component strongly interacting fermionic gas with SU(3) symmetry. These systems are particularly interesting due to their connections to the quark model in the framework of quantum chromodynamics. We label the three internal states as $|\uparrow\rangle$, $|\rightarrow\rangle$ and $|\downarrow\rangle$. While the

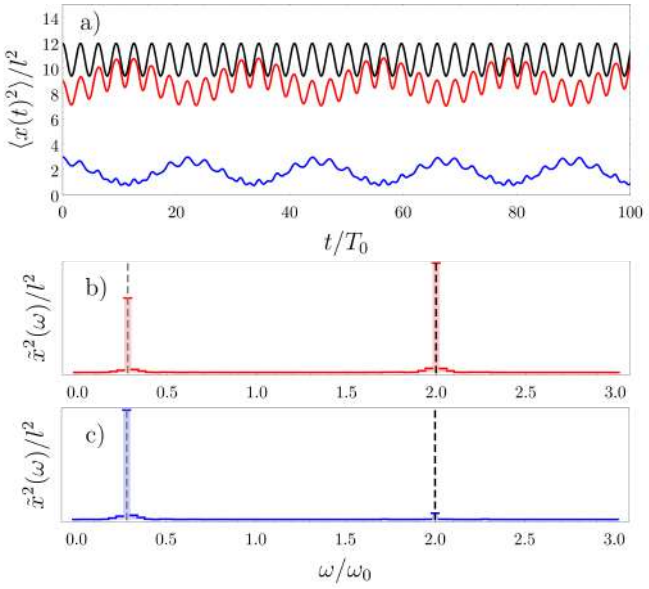


*Figure 7.4: Dynamics in the SU(2) fermionic system. a) Time evolution of the squared density widths $\langle x_\uparrow^2(t)\rangle$ (red), $\langle x_\downarrow^2(t)\rangle$ (blue) and $\langle x_c^2(t)\rangle$ (black). Panels b) and c) show the excitation peaks in the frequency domain, where the lower frequencies correspond to the spin excitations. The black dashed lines mark the frequency of the charge density oscillations. The gray dashed lines shows the value energy gap in the Floquet spectrum of the time-dependent spin chain.*

Hamiltonian can still be described by Eq. (7.2), the permutation operator is now given by

$$P_{i,i+1} = \frac{1}{3} + \frac{1}{2}\vec{\lambda}_i \cdot \vec{\lambda}_{i+1}, \tag{7.9}$$

where $\vec{\lambda}$ is the vector composed by the eight generators of the SU(3) group, namely the Gell-Mann matrices (see Appendix B for the matrix expressions of the generators). A system described by Eq. (7.9) can be mapped into the Lai-Sutherland model [112, 113] through $P_{i,i+1} = \vec{S}_i \cdot \vec{S}_{i+1} + (\vec{S}_i \cdot \vec{S}_{i+1})^2 - 1$, which is a particular case of the spin-1 bilinear biquadratic model [114, 115]. We keep the number of particles fixed as $N = 4$, with $N_\uparrow = 2$, $N_\rightarrow = 1$ and $N_\downarrow = 1$. We keep our focus on calculating the time evolution of the squared width $\langle x(t)^2\rangle$ its corresponding Fourier transform, while maintaining the quench protocol described in the previous sections.

In Fig. 7.5 a), we show $\langle x(t)^2\rangle$ for each component and for the charge density. Since we have two minority particles, each interacting with the remaining atoms with interaction strength $g$, the results for each of these components are identical. The excitation peaks seen in Figs. 7.5 b) and c) reveal the contributions of the charge and spin oscillations to the dynamics of each component. Still, we can see that the majority component has a larger contribution to

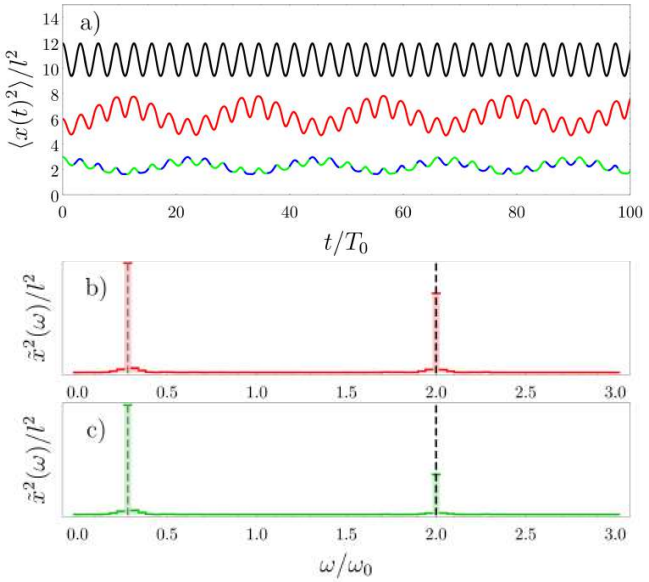


*Figure 7.5: Dynamics in the SU(3) fermionic system. a) Time evolution of the squared density widths $\langle x^2_\uparrow(t)\rangle$ (red), $\langle x^2_\rightarrow(t)\rangle$ (dashed green), $\langle x^2_\downarrow(t)\rangle$ (blue) and $\langle x^2_c(t)\rangle$ (black). Panels b) and c) show the excitation peaks in the frequency domain for $\langle x^2_\uparrow(t)\rangle$ and $\langle x^2_\rightarrow(t)\rangle$, respectively. The black dashed lines mark the frequency of the charge density oscillations. The gray dashed lines shows the value energy gap in the Floquet spectrum of the time-dependent spin chain.*

the charge excitations. The minority cases, however, show a slight increase in these frequencies as compared to the two-component case, with the spin oscillations remaining dominant.

### SU(4)

We now examine the effect of applying our formalism to the case where the number of particles $N$ matches the number of internal components. To that end, we consider the SU(4) fermionic gas with $N = 4$ and internal states labeled as $|\uparrow\rangle$, $|\nearrow\rangle$, $|\searrow\rangle$ and $|\downarrow\rangle$. The number of particles in each state is thus given by $N_\uparrow = 1$, $N_\nearrow = 1$, $N_\searrow = 1$ and $N_\downarrow = 1$ (the so-called 1+1+1+1 infinitely repulsive system with different masses is known to have interesting properties, which were described in Ref. [116]). We rewrite the permutation operator for the SU(4) system as

$$P_{i,i+1} = \frac{1}{4} + \frac{1}{2}\vec{\lambda}_i \cdot \vec{\lambda}_{i+1}, \tag{7.10}$$

where now $\vec{\lambda}$ represents the vector spanning the 15 SU(4) generators [117] (see Appendix B for the expressions). In the following, we focus on describing the results only for the $|\uparrow\rangle$ and $|\nearrow\rangle$ components.

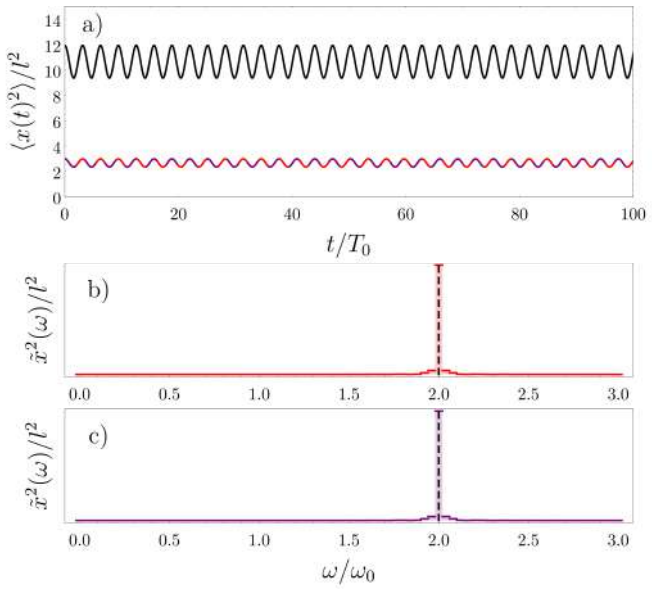


*Figure 7.6: Dynamics in the SU(4) fermionic system. a) Time evolution of the squared density widths $\langle x^2_\uparrow(t)\rangle$ (red), $\langle x^2_\nearrow(t)\rangle$ (dashed purple) and $\langle x^2_c(t)\rangle$ (black). Panels b) and c) show the excitation peaks in the frequency domain for $\langle x^2_\uparrow(t)\rangle$ and $\langle x^2_\nearrow(t)\rangle$, respectively. The black dashed lines mark the frequency of the charge density oscillations.*

It becomes clear that the behavior $\langle x^2(t)\rangle$ as a function of time is the same for both components shown in Fig. 7.6 (this also holds for the other two components not shown). This is expected since the number of internal components matches the total number of particles in the system. Moreover, the frequency spectrum shows that the only contributions in the oscillations stem from the charge excitations, as opoposed to the previous cases. This allows us to interpret the dynamics of the SU($N$) system with strong interactions as the one expected for a gas of impenetrable bosons, as long as the number of particles matches the number of internal components. This conclusion is in agreement with the observation that the momentum distribution of an SU($N$) Fermi with strong repulsion approaches that of a Tonks-Girardeau gas [36].

In the models considered here, a vanishing spin signal in the excitation spectrum can additionally be obtained by taking a balanced system with a lower number of internal components (e.g. a 2+2 SU(2) system). This can be explained as a result of the symmetric perturbation to the potential that determines the initial state of the system. Turning off the barrier in this particular case has no effect on the ground state of the spin chain, which remains unchanged as the charge oscillations take place. However, for a matching number of particles and internal components, the results described in this section are the only possible outcomes for a system initialized in the ground state.

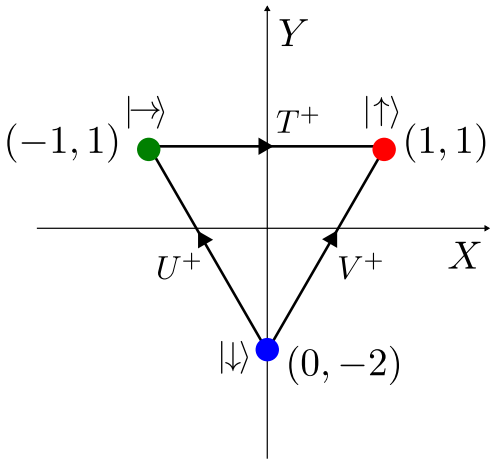


*Figure 7.7: Action of the SU(3) raising and lowering operators upon the internal states. Positions in the plane are defined by states' eigenvalues of the X and Y operators.*

### 7.2.4 Breaking SU(3) symmetry

An interesting perspective when dealing with multicomponent strongly interacting gases is a case where interactions are slightly imbalanced and a particular symmetry is broken. Here we analyze the three-component case with broken SU(3) symmetry. It is useful, in this context, to rewrite the SU(3) permutation operator in terms of raising and lowering operators. These are defined as $T^{\pm} = (\lambda^1 \pm i\lambda^2)/2$, $V^{\pm} = (\lambda^4 \pm i\lambda^5)/2$ and $U^{\pm} = (\lambda^6 \pm i\lambda^7)/2$, where once again $\lambda^i$ is a given Gell-Mann matrix. The internal states are eigenstates of the $X = \lambda^3$ and $Y = \sqrt{3}\lambda^8$ operators, as shown in Fig. 7.7. We still consider the particular case of $N = 4$, with $N_{\uparrow} = 2$, $N_{\rightarrow} = 1$ and $N_{\downarrow} = 1$.

Below we rewrite the permutation operator with these modifications, including an additional symmetry-breaking parameter $1/\eta$ which multiplies the operators $T^+$ and $T^-$.

$$\begin{aligned} P_{i,i+1} &= \frac{1}{3} + \frac{1}{\eta}\left(T_i^+ T_{i+1}^- + T_i^- T_{i+1}^+\right) + V_i^+ V_{i+1}^- + V_i^- V_{i+1}^+ \\ &+ U_i^+ U_{i+1}^- + U_i^- U_{i+1}^+ + \frac{1}{2}(\lambda_i^3 \lambda_{i+1}^3 + \lambda_i^8 \lambda_{i+1}^8), \end{aligned} \tag{7.11}$$

This means we are explicitly breaking the symmetry of the system by changing the energy contribution of turning $|\uparrow\rangle$ into $|\rightarrow\rangle$ and vice-versa. In Fig. 7.8 we show the result of breaking the SU(3) symmetry (by making $\eta = 0.5$) on the dynamics. While the effects in the $|\uparrow\rangle$ and $|\rightarrow\rangle$ components are subtle - a slight increase in the spin excitation frequency as seen in panels b) and c) - in $|\downarrow\rangle$ it is more drastic, with the spin contributions being distributed over several low frequencies. As a consequence, the peaks corresponding to

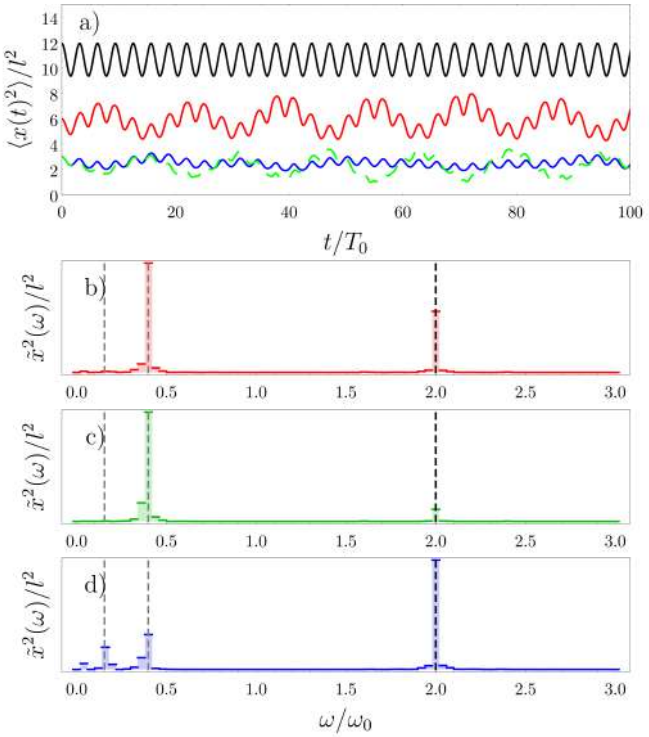


*Figure 7.8: Dynamics in the 3-component system with broken SU(3) symmetry. a) Time evolution of the squared density widths $\langle x^2_\uparrow(t)\rangle$ (red), $\langle x^2_\rightarrow(t)\rangle$ (dashed green), $\langle x^2_\downarrow(t)\rangle$ (blue) and $\langle x^2_c(t)\rangle$ (black). Panels b), c) and d) show the respective excitation peaks in the frequency domain. The black dashed lines mark the frequency of the charge density oscillations.*

spin oscillations in one of the components are almost washed out with respect to the charge excitations. On the other hand, the remaining components still preserve clear peaks for spin oscillations. This points to the possibility of measuring spin-charge separation even in a context where internal symmetries are not perfectly preserved. Of course, other results for the spin excitations can be expected by choosing a different value for $\eta$, or by breaking the symmetry in a different interaction channel.

### 7.2.5 A comparison to numerical results

In the calculations performed here we assumed that the spatial degrees of freedom could be described, in a dynamical context, by the time evolution of a Tonks-Girardeau wave function. The spin dynamics, on the other hand, is given by a time-dependent spin chain Hamiltonian.

Here we present a quick comparison of this approach to numerical calculations performed with the package OpenMPS (see Appendix A for details). We focus on comparing the case of SU(2) symmetry presented in Section. 7.2.3.

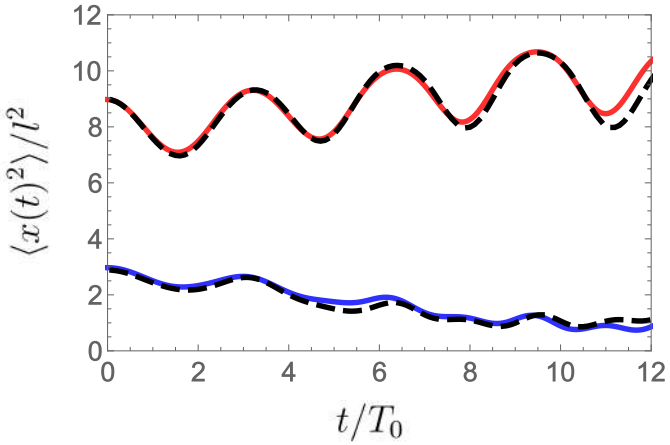


*Figure 7.9: Comparison of the oscillation modes for $\langle x_\uparrow^2(t)\rangle$ (red) and $\langle x_\downarrow^2(t)\rangle$ (blue) with numerical results obtained with the TEBD algorithm (black dashed curves).*

These calculations are performed with the TEBD (Time-Evolving Block Decimation) algorithm. We use the Fermi-Hubbard Hamiltonian as an approximation of the continuum problem by considering a total of $L = 51$ sites, where the continuum interaction strength is connected to the discrete interaction strength through $U = g/a$. The same protocol for the sudden change of the trapping potential is applied. Our results are displayed in Fig. 7.9.

Since the full numerical simulations are computationally cumbersome, we consider only the initial part of the time evolution of the system after the sudden change in the potential. A disagreement between the two methods should be expected in some measure, due to the approximation considered in the analytical approach but also because of a numerical error for larger times. The comparison could be improved by increasing the number of sites $L$ in the Fermi-Hubbard model to better approximate the continuum limit, or by decreasing the tolerance in the numerical error in the time evolution of the initial state.

## 7.3 Conclusions

In this chapter we have presented an analysis of the phenomenon of spin-charge separation in trapped atomic systems with SU($N$) symmetry. The dynamics of the system is obtained after a quench in the trapping potential, in which a central barrier in the harmonic trap is switched off. This simple protocol is particularly interesting from an experimental point of view, since it requires only minor modifications to the potential.

The sudden change in the trap induces the motion of the spatial degrees of freedom, which in turn are reflected in a time-dependence of the exchange coefficients of the spin chain. It is important to point out that, since the system

is initialized in the ground state of the spin chain, the motion observed in this sector is only possible due to the quench in the potential. By monitoring the time evolution of the breathing modes given by the oscillations in $\langle x^2(t)\rangle$, we describe the excitation spectrum of SU(2), SU(3) and SU(4) systems. In the particular case where the number of internal components exactly matches the number of particles, we see that the spin excitations are completely washed out, and the only contributions are due to charge oscillations that agree with those of a spinless Fermi gas.

We have thus demonstrated that spin-charge separation, rather than being a bulk effect of many-body systems, can occur in few-body ensembles under fairly simple conditions. The formalism described here can also be used to predict the behavior of quantum gases with different atomic species (e.g. a bosonic mixture), or generalized to more involved quench protocols, simply by mapping the time evolution of the spatial orbitals into the exchange coefficients of the spin chain under consideration.

# Chapter 8

# Discrete time-translation symmetry breaking in a few-body spin chain

Recent developments in theory and experiments with time-dependent quantum mechanical set-ups have consolidated the concept of the *discrete time crystal*, a system that spontaneously breaks discrete time-translation symmetry. The original proposals for time crystals, both in the quantum [118] and classical [119] regimes, suggested the possibility of a system exhibiting a periodic dynamical behavior in its lowest energy state [120]. This possibility seems to have been ruled out by subsequent discussions [121, 122], including no-go theorems for a broad class of systems [123, 124].

Surprisingly, it was later shown that systems in the presence of periodic driving, generally described by Floquet theory [89], can indeed self-organize and present a subharmonic response in the observables [125–127]. The phase which exhibits the features of spatiotemporal order now recognized in time crystals was also classified as the $\pi$-spin glass [128], and since then a precise definition has been put forward [129].

The main idea behind discrete time crystals is the following [130]: a periodically driven system exhibits discrete time-translation symmetry, given that the Hamiltonian behaves in time as $H(t+T) = H(t)$. Now, breaking this discrete symmetry means that the system responds to this periodic driving with a different period, which is usually larger and thus constitutes a subhamornic response. Moreover, it is required that this response be non-trivial (which rules out non-interacting systems) and robust against imperfections in the drive and spatial disorder.

The properties of these systems have been studied in radically different configurations, such as atoms bouncing off an oscillating mirror [131] or spin chains in the presence of disorder and many-body localization [132]. The latter proved to be an ideal starting point for experiments and resulted in the first

two observations of time crystals. While these experiments dealt with two rather distinct arrangements (one exploring nitrogen vacancies in diamonds [133] and the other a chain of trapped ions [134]), both had as a major feature the presence of disorder. Since the external driving in such systems leads to heating and eventual thermalization, it is generally assumed that Floquet time crystals should occur in a pre-thermal regime. The existence of a many-body localized regime serves, in this context, as a source of stabilization against thermal effects.

Other studies have shown, however, that disorder is not a crucial requirement for the realization of discrete time crystals [135]. Cold atomic systems, for instance, can sustain a time crystal phase even in a “clean" set-up where disorder is absent [136]. Experimentally, time crystal phases have been observed in ordered spin systems with nuclear magnetic resonance techniques [137, 138]. In these studies, the presence of interactions between atoms or spins is the decisive factor leading up to time-translation symmetry breaking. The manifestation of quasi-crystalline order and its transition to a time crystal has been observed with Bose-Einstein condensates under the action of periodical magnetic fields [139].

These developments raise the question of how simple a system that exhibits a time crystal phase can be. To address this matter, we present a proposal for the realization of discrete time-translation symmetry breaking in a few-body system of cold atoms (see Fig. 8.1 for a schematic depiction), where the interactions between different components can be tuned by means of Feshbach [14] or confinement induced resonances [15]. In the limit of strong interactions, the system behaves as a spin chain, where the exchange coefficients are determined by the shape of the trapping potential [34, 78]. Periodically driving the system with spin-flip pulses [140] results in a response in the magnetization which depends highly on the choice of interaction parameters. Moreover, we show that realizing the system with fermionic or bosonic atoms - the latter assuming that interactions between identical particles can be tuned - yields very distinct results.

The content of this chapter has been taken from Ref. [141]. The original material contains a section on superconducting circuits written in collaboration with Stig E. Rasmussen, which has been removed here to focus on the case of cold atoms. This introduction, Sections 8.1, 8.2, 8.3 and 8.5 and Fig. 8.1 have been changed to accommodate this modification. Section 8.4 is originally part of the Supplemental Material of the reference above. The title and some small sections of the text have also been modified with respect to the original publication.

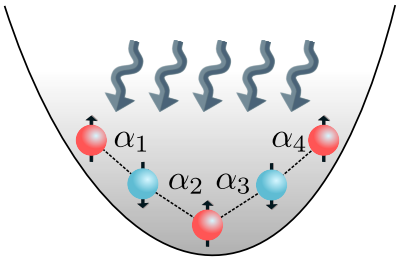


*Figure 8.1: Schematic depiction of the few-body system under consideration: an ensemble of cold atoms in a harmonic trap, where the strong interactions allow for a mapping of the system to a spin chain with position-dependent exchange coefficients. The driving protocol can be realized by applying spin-flip pulses, represented by the gray arrows.*

## 8.1 System description and driving protocol

Proposals for the realization of time-crystals with ultracold atoms usually involve the many-body problem of bosons in the presence of a periodic Hamiltonian [142, 143], which is generally described by the Gross-Pitaevskii equation. In the present case we focus on the few-body problem of bosonic atoms with two internal components, which we label as the pseudospin states $|\uparrow\rangle$ and $|\downarrow\rangle$. We assume contact interactions given by $g\sum_{i<j}\delta(x_i - x_j)$ for atoms in different internal states and $\kappa g\sum_{i<j}\delta(x_i - x_j)$ for atoms in the same internal state. All atoms are confined by an effectively one-dimensional harmonic trap described by $V(x) = \frac{1}{2}m\omega^2 x^2$. For simplicity, we assume the atoms to have the same mass $m = 1$, and define the trapping frequency as $\omega = 1$.

In the limit of strong interactions ($g \gg 1$), this system can be described, up to linear order in $1/g$, by an effective spin chain [46, 78], which can be described by

$$H = -\sum_{i=1}^{N-1}\frac{\alpha_i}{g}\left[\frac{1}{2}\left(1 - \vec{\sigma}^i\cdot\vec{\sigma}^{i+1}\right) + \frac{1}{\kappa}\left(1 + \sigma_z^i\sigma_z^{i+1}\right)\right], \tag{8.1}$$

where $\alpha_i$ are position-dependent exchange coefficients, which are determined solely by the trapping geometry, and the remaining parameters have the meaning described above. In the case of $N = 5$ in a harmonic trap, the exchange coefficients have the values $\alpha_1 = \alpha_4 \approx 2.16612$ and $\alpha_2 = \alpha_3 \approx 3.17738$, where the symmetry of the coefficients in guaranteed by the parity invariance of the trap. The Hamiltonian above is the same spin chain Hamiltonian derived in Chapter 2, where $\kappa$ sets the strength of the intraspecies interactions. While this Hamiltonian describes a system of strongly interacting bosons (due to the presence of interactions between identical components), we can reproduce a fermionic system by taking the limit $\kappa \to \infty$. Then, we obtain

$$H = -\sum_{i=1}^{N-1} \frac{\alpha_i}{g}(1 - P_{i,i+1}), \tag{8.2}$$

where $P^{i,i+1} = \frac{1}{2}(1 + \vec{\sigma}^i \cdot \vec{\sigma}^{i+1})$ is the permutation operator that exchanges neighboring spins. Contrary to other theoretical approaches [144, 145] and experiments [133], our model does not require long-range interactions.

## 8.2 Driving protocol

We focus on a system of $N = 5$ spins and our protocol for the external driving is fairly simple: we choose an initial antiferromagnetic state, such as $|\psi(0)\rangle = |\uparrow\downarrow\uparrow\downarrow\uparrow\rangle$, which is not an eigenstate of the spin chain under any non-trivial parameter configuration. We then realize a sequence of spin-flip operations (with period $T_D$) at each site, rotating all spins by an angle $\theta$. The spin-flip operator is thus described by

$$O = \exp\left(-i\frac{\theta}{2}\sum_{i=1}^{N}\sigma_x^i\right). \tag{8.3}$$

We keep track of the time evolution of the magnetization as given by

$$m(t) = \langle\psi(t)|\sum_{i=1}^{N}\sigma_z^i|\psi(t)\rangle, \tag{8.4}$$

which is the quantity we choose to register the effect of the external driving on the system. For perfect ($\theta = \pi$) pulses, the magnetization has a trivial periodicity of $T_m = 2T_D$. However, for imperfect rotations described by $\theta = \pi - \epsilon$, we obtain a different response, which is strongly determined by the presence of interactions between the spins. In the next section, we focus on pulse imperfections of a constant value. However, we have also taken into account cases with slightly modulated pulses (see Section 8.4).

## 8.3 Results

In Fig.8.2 a), b) and c) we show, respectively, the results for the time evolution of the magnetization $m(t)$, the overlap probability of the wave function with the initial state, given by

$$F(t) = |\langle\psi(0)|\psi(t)\rangle|^2, \tag{8.5}$$

and the spectral density

$$S(f) = |\hat{m}(f)|^2, \tag{8.6}$$

where $m(f) = \int dt\, e^{-2\pi i f t} m(t)$ is the Fourier transform of the magnetization. We initially assume a periodic pulse that rotates the spins by an angle of $\theta = \pi$

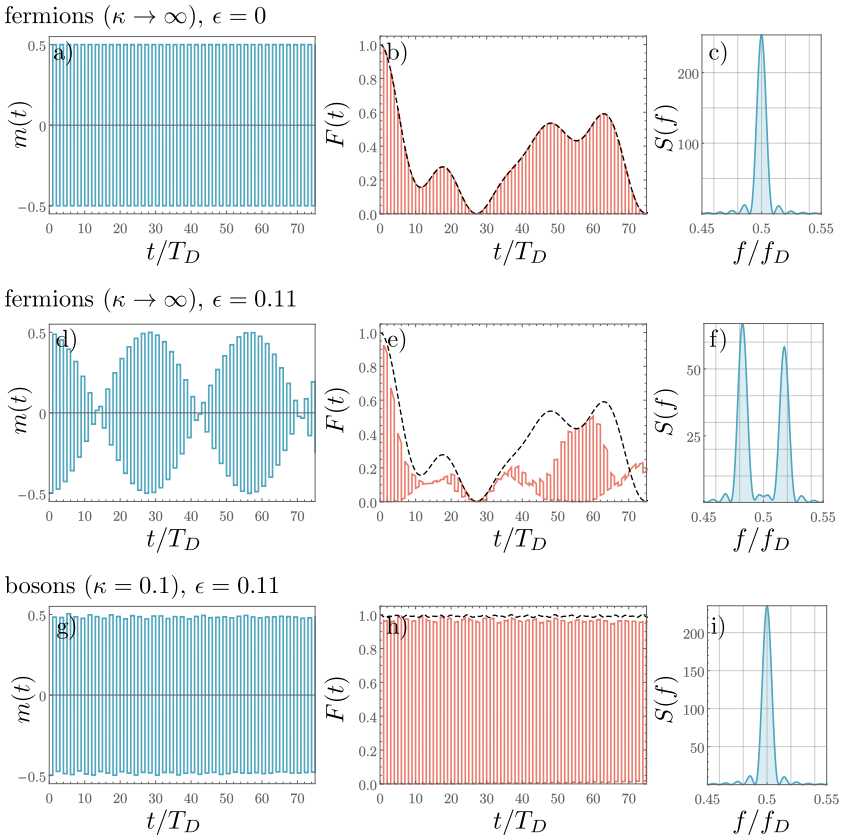


*Figure 8.2: Time evolution of observables in a system of $N = 5$ harmonically trapped atoms. The parameter $\kappa$ defines the atomic species (fermionic or bosonic) and the value of $\epsilon$ determines the presence of imperfections in the driving (for $\epsilon = 0$ we have a perfect $\pi$-pulse). Panels a), d) and g) show the time evolution of the magnetization, while panels b), e) and h) present the analogous results for the overlap with the initial state $F(t)$. In these figures, the black dashed curves show the results for $F(t)$ in the absence of driving. Panels c), f) and i) show the spectral density obtained through the Fourier transform of $m(t)$.*

at times $t = nT_D$ with $n$ being an integer. We find that the magnetization oscillates with a period twice as large as the driving, which results in a peak in $f = f_D/2$ where $f_D$ is the driving frequency. While this quantity only registers the global behavior of the system, the overlap with the initial state $F(t)$ describes its underlying spin dynamics. When all spins are rotated by $\pi$ with respect to the initial state, we have $F(t) = 0$. In the remaining times, we observe that the time evolution of the spin distribution is described by the exact results in the absence of periodic driving (black dashed curves).

If we consider an imperfect pulse with $\theta = \pi - \epsilon$, we observe two different results. In the case of fermions (Figs. 8.2 d), e) and f)), the magnetization now exhibits a beating pattern that destroys the subharmonic peak at $f = f_D/2$.

The overlap $F(t)$ is no longer described by the result in the absence of driving. For bosons (Figs. 8.2 g), h) and i)), on the other hand, the presence of a dominating interaction between identical spins - defined by the small value of $\kappa$ - locks back the magnetization response peak at $f = f_D/2$, even for $\epsilon \neq 0$. Here we see the breaking of the discrete time-translation symmetry (since the response period is larger than the periodicity of the Hamiltonian) which is not affected by the imperfect driving. This robustness of the response in the presence of imperfect pulses is one of the defining features of a time crystal phase [132]. In fact, here we find that it arises under fairly simple conditions, without the need of switching interactions on and off as part of the driving protocol. Moreover, it presents the possibility of studying the "melting" of time crystals - in a many-body context - as interactions are modified. This could be implemented, for instance, by taking a bosonic system and tuning $\kappa$ from small to large.

While cold atom experiments with fermions frequently deal with $^6$Li atoms [28], two-component bosonic systems can be produced with a gas of $^{87}$Rb atoms, where the two lowest hyperfine states are given by $|F = 2, m_f = -1\rangle$ and $|F = 1, m_f = 1\rangle$. Imbalance in the interactions can be introduced, for instance, by means of confinement induced resonances [146]. The atoms can then be driven between the two different hyperfine states through Raman pulses, with a typical frequency of $\sim 6834$ MHz. An important feature of these systems is that the energy and time scales can be controlled by modifying the external confinement (the inverse frequency of the harmonic trap in a few-body experiment is $\sim 100\,\mu$s). Recent works with multi-component bosonic $^{87}$Rb systems indicate a lifetime of the order of $\mu$s with minimal heating originating from Raman processes [37].

The driving protocol employed here can be also used in the case of systems with more than two internal components, as long as Ising-type interactions are dominant in the Hamiltonian. By periodically switching between different pseudospin states, it is possible to expect a fractional response frequency given by $f = f_D/\nu$ where $\nu$ is the number of internal states available. Multi-component cold atomic gases, such as fermionic systems with SU($N$) symmetry, have been theoretically explored [59, 86], and can be realized in the lab [36, 38]. A recent proposal for realizing time-crystals in SU($N$) systems explores the ladder of internal states as a synthetic dimension [136]. In a more extreme example, systems where the response frequency is much smaller than the driving frequency have been obtained in the framework of atoms bouncing off an oscillating mirror [142].

## 8.4 Simulation in a lattice potential

In this section we extend our simulations to the case of a lattice potential, which is extensively explored in experimental studies [13]. We increase our

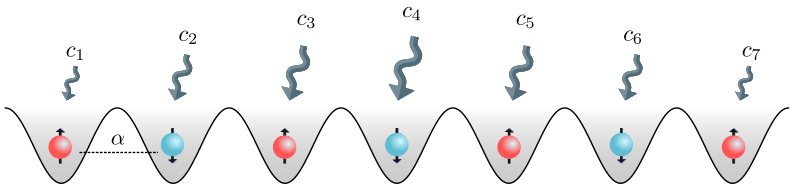


*Figure 8.3: A system of $N = 7$ atoms in a lattice potential. Our mixture consists of $N_\uparrow = 4$ and $N_\downarrow = 3$ atoms. We assume a set of homogeneous coefficients $\alpha = 1$. The external pulses are represented by the gray arrows and modulated by the coefficients $c_1 = c_7 = 0.98$, $c_2 = c_6 = 0.99$, $c_3 = c_5 = 1.0$, $c_4 = 1.1$.*

spin chain description of the strongly interacting system to a mixture consisting of $N_\uparrow = 4$ and $N_\downarrow = 3$ atoms and consider each site of the lattice to be populated by a single atom (half-filling).

The presence of the lattice potential is now encoded in a set of homogeneous exchange coefficients $\alpha_i$. The magnitude of these coefficients can be manipulated experimentally by changing the lattice depth and by consequence the size of the barrier separating a pair of atoms. Additionally, we consider also the presence of a slightly modulated driving pulse described by $O = \exp\left(-i\frac{\theta}{2}\sum_{i=1}^{N} c_i\sigma_x^i\right)$, where $\theta = \pi - \epsilon$ and $\epsilon$ is the pulse imperfection. The modulations are thus given by the coefficients $c_i$ and the initial state is kept as $|\psi_0\rangle = |\uparrow\downarrow\uparrow\downarrow\uparrow\downarrow\uparrow\rangle$. In Fig. 8.3 we show a sketch of the system under consideration.

In Fig. 8.4 we show the results for the time evolution of the magnetization $m(t)$, the overlap with the initial state $F(t)$ and the Fourier peaks of the magnetization $S(f)$. We focus on the perturbed cases where $\epsilon = 0.1$. The fermionic case ($\kappa \to \infty$) again shows beating due to the imperfect pulses, with the possibility of $m(t) > 0.5$ due to the modulation in the pulse. In the bosonic case with $\kappa = 0.1$ we again find a period locking, even with a modulated external pulse. Moreover, the system presents a complex underlying spin dynamics, which is made evident by the disagreement between the behavior of $F(t)$ in the plots and the predicted results in the abscence of driving (black dashed curves).

## 8.5 Conclusions

We have presented a proposal for the realization of discrete time-translation symmetry breaking in a few-body spin chain consisting of strongly interacting harmonically trapped atoms. A time crystal-like behavior arises under the action of a periodic spin-flip driving, provided that the intraspecies repulsion is smaller than the remaining interactions. This leads to the possibility of studying time crystallization in bosonic as opposed to fermionic systems, or even the dynamical “melting" of the time-crystal as the intraspecies interactions are tuned. In this approach we do not need to introduce disorder, which

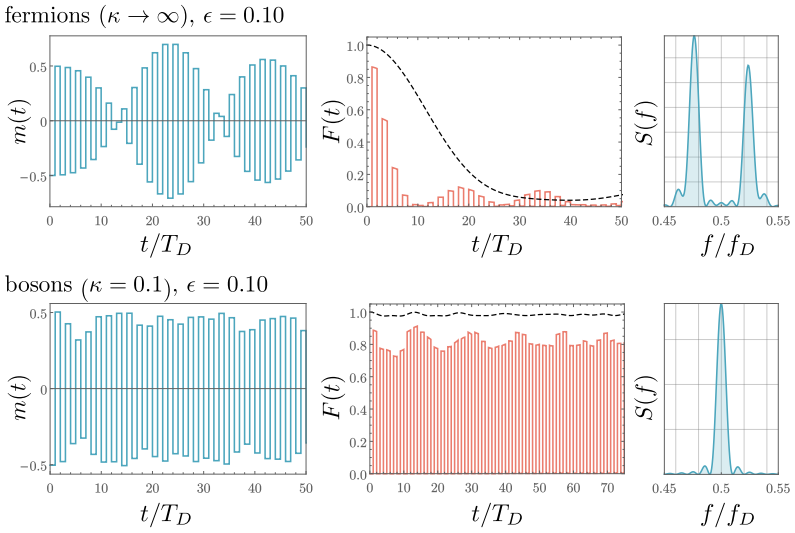


*Figure 8.4: Time evolution of the magnetization $m(t)$ (left column), the overlap with the initial state $F(t)$ (center column) and the Fourier peaks of the magnetization $S(f)$ (right column). The top panels show the results for fermions, while the bottom panels correspond to bosons. The black dashed curves show the results for $F(t)$ in the abscence of external driving. The driving period and driving frequency are denoted by $T_D$ and $f_D$, respectively.*

is a common features in previous studies. Naturally, the results described in our study can be generalized to larger chains or systems with more internal degrees of freedom.

# Part III

# Static and dynamical properties of one-dimensional bosonic mixtures

# Chapter 9

# Static correlations in a few-body Bose mixture

In the previous part of this thesis, we have focus on caculating the static and dynamical properties of one-dimensional strongly correlated systems. We employed our theoretical tools not only to study few-body systems of trapped cold atoms, but also spin chains which can be realized in alternative setups, such as superconducting circuits. Now we take a step back and focus on the properties of one-dimensional bosonic systems away from the limit of strong interactions.

In this chapter, we investigate the ground-state properties of a few-body system of bosons in a one-dimensional harmonic trap in the presence of an impurity of the same mass but in a different hyperfine state. We propose a trial wave function based on the analytical solution for two trapped particles [31], which generalizes the pair correlated wave function approach [147] for the case of different interactions. This procedure allows us to study few-body mixtures and calculate quantities such as correlation functions and momentum distribution. We obtain such quantities for a system of two bosons and one impurity and show that our results for the correlations are in good agreement with the exact diagonalization for all interacting regimes and with existing analytical results for the strongly repulsive impurity limit.

The results shown in this chapter have been published originally in Ref. [148], in collaboration with A. S. Dehkharghani, who provided the data for the numerical diagonalization and results for the infinitely repulsive limit. With respect to the original publication, the introduction and system description have been substantially changed to avoid repetition with respect to the previous chapters. A section from the original publication, on the analytics of the wave function in the limit of infinite repulsion, has been removed. Aside from minor modifications, the remaining part of the chapter and the figures have been kept identical to the original publication. The content of this chapter has also been presented as part of the Qualifying Exam.

## 9.1 Hamiltonian

We start by considering a system of bosons with contact interactions in a one-dimensional harmonic trap. The Hamiltonian for the $N$-body case is written as

$$H = -\frac{1}{2}\sum_{i=1}^{N}\frac{\partial^2}{\partial x_i^2} + \sum_{i=1}^{N}\frac{x_i^2}{2} + \sum_{i<j} g_{ij}\delta(x_i - x_j) \tag{9.1}$$

where we consider the energies and lengths in units of $\hbar\omega_L$ and $b_L = \sqrt{\hbar/m\omega_L}$, with $\omega_L$ being the longitudinal harmonic confinement. The parameter $g_{ij}$ is given in units of $\hbar^2/mb_L$ and accounts for the possible different interactions between the pairs of atoms. Experimentally, these interactions can be controlled by means of Feshbach [14] and confinement-induced resonances [15]. In the absence of a trapping potential and considering all interactions between the pairs to be equal, the Hamiltonian (9.1) reduces to the well-known Lieb-Liniger integrable Hamiltonian [17, 18]. In this work, we will be particularly interested in the case of three bosons with equal masses.

## 9.2 Ansatz

To calculate the physical properties of this model, we write our ansatz for the wave function as

$$\Psi(x_1, x_2, ..., x_N) = \Phi_{CM}\psi_R, \tag{9.2}$$

where $\Phi_{CM} = \mathcal{N}_{CM}\exp\left[\left(\sum_i^N x_i\right)^2/2N\right]$ is the center of mass part of the wave function and $\mathcal{N}_{CM}$ is a normalization constant. The relative part of the wave function, $\psi_R$, is written as

$$\psi_R = \mathcal{N}_R\prod_{i<j}^{P} D(\beta_{ij}|x_j - x_i|;\mu_{ij}), \tag{9.3}$$

where $P = \frac{N(N-1)}{2}$ is the number of pairs, $D$ is a parabolic cylinder function [149] which depends on the absolute separation between the particles $|x_j - x_i|$ and the parameters $\beta_{ij}$ and $\mu_{ij}$, and $\mathcal{N}_R$ is a normalization constant. This factorized form of the wave function has first been proposed and used to describe $N$-body bosonic systems with equal interactions in [147], where it is employed to calculate energies and correlation properties. It is based on the seminal solution by Thomas Busch *et al.* for the case of two $\delta$-interacting cold atoms in a harmonic trap [31]. For the case of different interactions in a homogeneous potential, a similar procedure has been proposed in Ref. [150]. Here, we combine these two approaches to treat the general case of bosons with different interactions in a trap. Using the boundary condition for the delta function potential between a pair of particles, we find the following relation for $\mu_{ij}$ and $g_{ij}$:

$$\frac{g_{ij}}{\beta_{ij}} = -\frac{2^{3/2}\Gamma(\frac{1-\mu_{ij}}{2})}{\Gamma(\frac{-\mu_{ij}}{2})}, \tag{9.4}$$

where $\Gamma$ are Gamma functions and $\mu_{ij}$ varies between 0 and 1 as $g_{ij}$ grows from 0 to $\infty$. By choosing all $\beta_{ij} = \sqrt{2/N}$ and considering all interactions equal ($g_{ij} = g$ for any pair) the total wave function reproduces the known analytical ground state results in the non-interacting

$$\Psi_0 = \mathcal{N} e^{-\sum_i^N \frac{x_i^2}{2}} \tag{9.5}$$

and infinitely repulsive, also called Tonks-Girardeau (TG) [44]

$$\Psi_\infty = \mathcal{N} e^{-\sum_i^N \frac{x_i^2}{2}} \prod_{i<j}^{P} |x_j - x_i| \tag{9.6}$$

cases, where $\mathcal{N}$ is the appropriate normalization constants for each limit. For the particular case of $N = 2$, Eq. (9.3) is the exact relative wave function at any interaction strength [31]. Outside of the limits described above (e. g. for equal intermediate interactions or mixtures of bosons with different interactions) the parameters $\beta_{ij}$ are not fixed at $\sqrt{2/N}$, and we may treat them variationally.

## 9.3 Probability densities

In this section we use our ansatz to calculate the densities for a system of three bosons in the harmonic trap. First we consider a system with equal interactions in the limits of $g = 0$ and $g \to \infty$, then we calculate the same properties for a system of two identical bosons plus an impurity, considering this atom has a different interaction strength than the remaining pair. The case of four particles is briefly discussed in the end of this section.

### 9.3.1 Equal Interactions

The single particle densities are defined for a normalized wave function as

$$\rho(x_1) = \int dx_2, ..., dx_N |\Psi(x_1, x_2, ..., x_N)|^2. \tag{9.7}$$

In Fig. 9.1 a) we show results for this quantity obtained using $\Psi(x_1, ..., x_N) = \Phi_{CM}\psi_R$ with $\psi_R$ defined in Eq. (9.3), for the strongly interacting ($g = 1000$, $\mu \sim 1$) and for the non-interacting ($g = 0$, $\mu = 0$) limits in the case of three identical bosons, where our wave function reproduces the exact results. We observe the tendency of the atoms to separate in the trap in the strongly repulsive case, with the appearance of three separate peaks. The

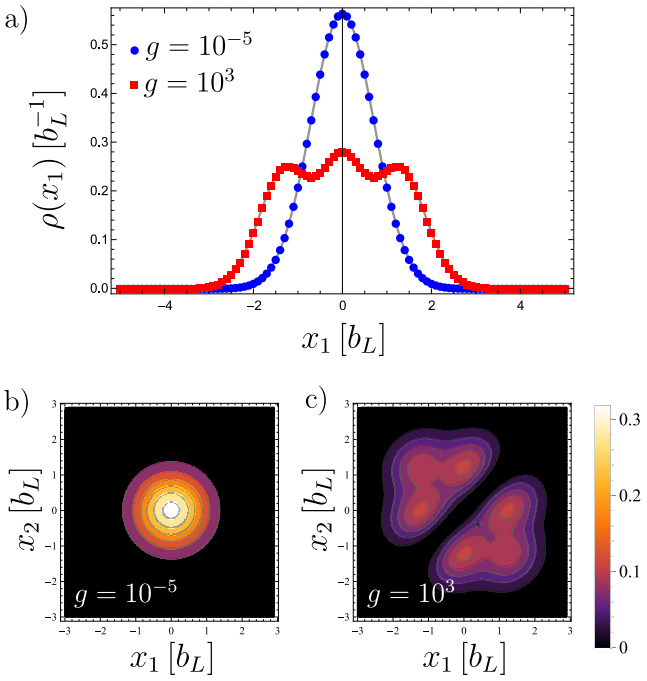


*Figure 9.1: a) Single-particle densities in the non-interacting (blue circles) and strongly interacting (red squares) limits. The solid gray lines show the results obtained using the analytical limits 9.5 and 9.6. Pair correlations for b) the non-interacting and c) the strongly repulsive limits.*

non-interacting case shows the expected Gaussian profile. We also notice that the wave function correctly reproduces the analytical cases given by Eqs. (9.5) and (9.6). The pair correlation function, defined as $\rho_2(x_1, x_2) = \int dx_3, ..., dx_N |\Psi(x_1, x_2, ..., x_N)|^2$, shows similar effects; in Fig. 9.1 b), the atoms do not interact; therefore the separation between any given pair can be zero. In Fig. 9.1 c), the density goes to zero around the diagonal $x_1 = x_2$, since the repulsion is strong.

### 9.3.2 Different Interactions: Two Bosons and one Impurity

We now turn to the case of different interactions between the atoms in the trap. We focus in the problem of two identical bosons plus an impurity. In Fig. 9.2 a) and b) we show a schematic depiction of two possible configurations of the system. In a) we have the non-interacting case where all bosons can be considered identical. In this scenario all particles tend to occupy positions close to the center of the trap. If the interaction between the impurity and the majority atoms is strong, as shown in Fig. 9.2 b), then the impurity will be found at the edges of the trap. This effect can be verified in the correlations of this system, as will be shown next.

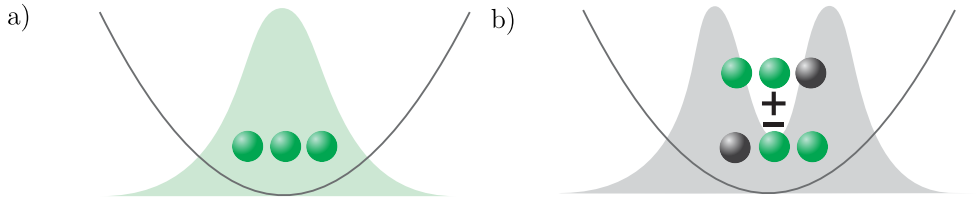


*Figure 9.2: Depiction of two possible states for three bosons in the trap. a) Three identical, non-interacting bosons and b) two identical bosons and a strongly repulsive impurity.*

We rewrite the coordinates as $x_I$ for the impurity atom and $(x_{M1}, x_{M2})$ for the majority identical bosons. The interaction parameters are set as $g_{IM}$ for the impurity-majority interactions and $g_{MM}$ for the majority-majority interaction. The condition $\beta_{ij} = \sqrt{2/N}$ is no longer necessary in the case of different interactions. Furthermore, since the interaction $g$ may be different for each pair, the parameters $\beta_{ij}$ may also be varied independently. To improve the precision of our approach, we therefore treat $\beta_{ij}$ variationally, optimizing this parameter in each interaction case. We focus in three interaction regimes: non-interacting ($g \sim 0$), intermediate interaction ($g = 2.56$) and strong interaction ($g = 200$).

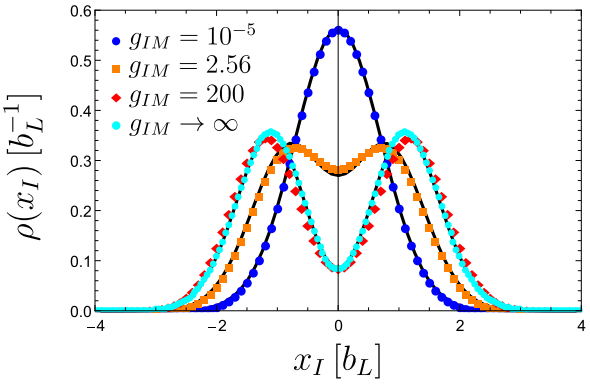


*Figure 9.3: Spatial densities for the impurity boson with different impurity-majority interaction strengths. The black solid lines show the results obtained through exact diagonalization and the light blue dots the results from the analytical wave function in the infinite repulsive limit.*

In Fig. 9.3 we plot the spatial densities for the impurity atom. We assume in this case that the majority bosons are non-interacting ($g_{MM} = 0$). The most relevant physical effect in this case is the increasing separation of the density for the impurity, which tends to locate at one of the sides of the trap as a consequence of the repulsion with the majority bosons. In Fig. 9.3 we also verify the validity of our approach by comparing to results obtained by numerical diagonalization. In the non-interacting regime we observe once

again that the exact density is reproduced. In the intermediate and strongly repulsive regimes, we observe small deviations from the exact results, although the general behavior is well captured. For the strongly repulsive regime we also present a comparison with an analytical wave function, obtained by considering $g_{MM} = 0$ and $g_{IM} \to \infty$ (see Ref. [57] for details). We notice that this result agrees well with the case of $g_{IM} = 200$, both in the exact diagonalization and in the pair correlated ansatz, which shows that for a value of $g_{IM} = 200$ the limit of infinite repulsion is effectively reached. The difference $\epsilon(x_I) = (\rho(x_I)_{ED} - \rho(x_I))^2$, where $\rho(x_I)_{ED}$ is the results for the one-body correlation function obtained by exact diagonalization, is, as expected, $\epsilon(x_I) = 0$ for all points in the non-interacting case; in the interacting cases, it assumes slightly larger values, in particular around $x_I = 0$ for $g_{IM} = 2.56$ and $x_I \pm 1.8$ for $g_{IM} = 200$. At these last points, nevertheless, the value of $\epsilon(x_I)$ is still considerably small ($\sim 0.001$).

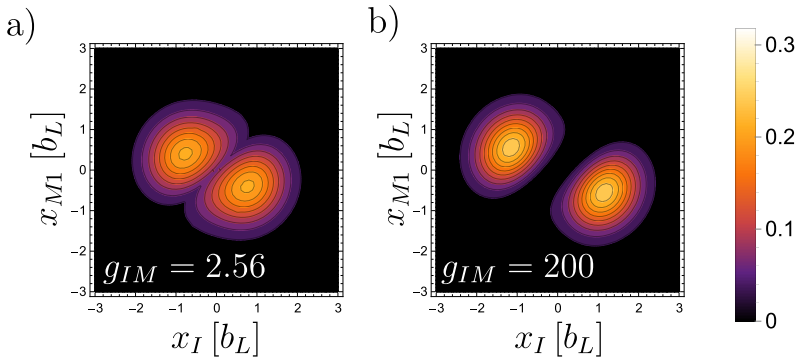


*Figure 9.4: Pair correlation function for an impurity-majority pair, with interactions fixed as a) $g_{IM} = 2.56$ and $g_{MM} = 0$, b) $g_{IM} = 200$ and $g_{MM} = 0$.*

The pair correlations shown for an impurity-majority pair in Figs. 9.4 a) and b) also depict the tendency for the separation between the atoms of different species, along the diagonal $x_I = x_{M1}$, as the interaction $g_{IM}$ is increased.

The momentum distribution, a quantity of great experimental interest, can be calculated as well from our approach, by taking a Fourier transform of the one-body correlation function: $n(p) = (1/2\pi) \int dx\, dx'\, e^{-ip(x-x')} \rho(x, x')$. In Fig. 9.5 a) we show results for the momentum distribution of the impurity as the interaction parameter $g_{IM}$ is increased. The non-interacting case is simply the Fourier transform of the non-interacting case shown in Fig. 9.3 and therefore has a simple Gaussian profile.

In the case of mixed interactions we consider $g_{MM} = 10^{-5}$. In Fig. 9.5 b) we show the agreement between these two results and the ones obtained by numerical diagonalization. In Fig. 9.5 c) we show the same results in log-log scale, where it becomes clear that, for the interacting cases, the momentum

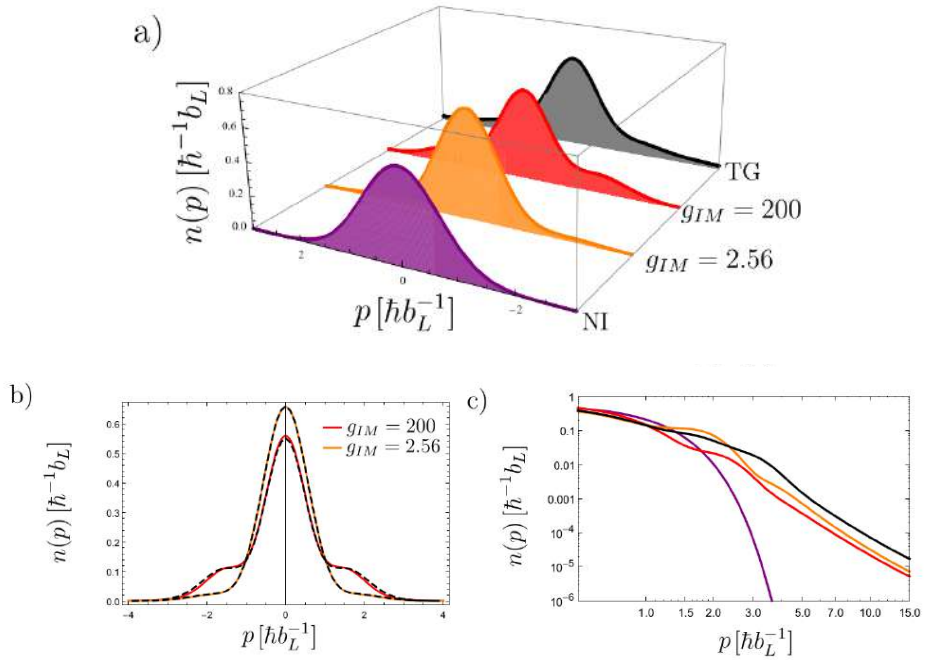


*Figure 9.5: a) Momentum distribution for the impurity in different interaction regimes. The purple curve shows the result obtained with the exact non-interacting wave function and the black curve shows the equal-interaction strongly repulsive case (Tonks-Girardeau gas). b) Same results as in a) for the mixed interactions: $g_{MM} = 10^{-5}$ and $g_{IM} = 200$ (red curve) and $g_{MM} = 10^{-5}$ and $g_{IM} = 2.56$ (orange curve), compared to exact diagonalization results (dashed curves). c) Log-log scale plot of the results in a). All interacting cases obey the $C/p^4$ power-law for asymptotic values of p.*

distribution obeys a power law $C/p^4$ for high values of $p$. This is a characteristic behavior of systems with $\delta$ interaction; the constant $C$ is usually called the contact parameter, a concept that captures all universal properties of systems [151] and can be obtained analytically for both homogeneous [152] and trapped [153] models.

For the particular case of a non-interacting majority pair and a strongly repulsive impurity it is also possible to notice the bunching of the majority bosons as a result of this repulsion. Fig. 9.6 a) shows the pair correlations for the majority pair in this scenario. The identical bosons tend to occupy the same position due to the weak repulsion between them, but this position is slightly deviated from the origin of the system. This effect has consequences on the Fourier transform of the pair correlations, defined as $n_2(p) = \int dx_3\, e^{-ip(x_1-x_2)}\rho_2(x_1, x_2)$ for an impurity-majority pair, and as $n_2(p) = \int dx_1\, e^{-ip(x_2-x_3)}\rho_2(x_2, x_3)$ for a majority-majority pair. In Fig. 9.6 b) we show results for this quantity in the same interaction regimes as in Fig. 9.5. The red and orange solid lines show the results for mixed interac-

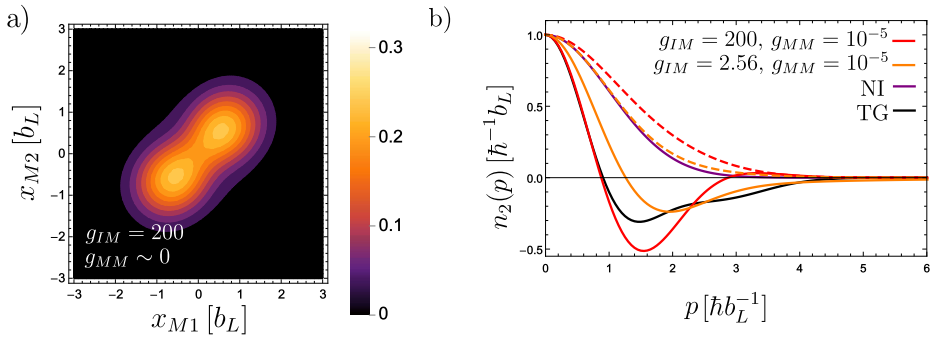


*Figure 9.6: a) Correlations for the non-interacting majority-majority pair with strongly repulsive impurity. b) Fourier transform of the pair correlations in the non-interacting and Tonks-Girardeau cases (purple and black solid lines, respectively) and in the cases of intermediate (orange) and strong (red) repulsion by the impurity. Solid lines correspond to the impurity-majority pair, while the dashed lines correspond to the majority-majority pair.*

tions considering an impurity-majority pair, with a behavior similar to that of Fig. 9.5 when compared to the cases of equal interactions. The Fourier transform of the majority pair (dashed lines), however, assumes values larger than the non-interacting results for the low-momentum region. This effect can be traced back to peaks in the static structure factor of homogeneous systems [150], which accounts for an effective attractive interaction for the given pair of bosons.

### 9.3.3 Three Bosons and one Impurity

Finally, to illustrate the generality of this approach, we extend it to the case of four particles (three identical bosons and an impurity). In Fig. 9.7, we present results for the one-body densities, with interactions between the impurity and the majority pair again ranging from weak to strong, while the majority-majority interactions are kept small ($g_{MM} = 10^{-5}$). Again, we notice the separation of the density for the impurity as the interactions are increased. The peaks are more pronounced than in Fig. 9.3, since the number of identical bosons is larger. This effect can also be interpreted as precursor of ferromagnetism in bosonic systems [57, 60], since particles of the same species tend to bunch up on one side of the trap (provided that the intra-species interaction is small).

### 9.3.4 Total density for mixed interactions

Considering our approach has been validated by the comparison to exact numerical results, and to further elucidate the effect of the repulsive delta interactions between the pairs on the correlations, we now look at the normalized total density $|\Psi(x_I, x_{M1}, x_{M2})|^2$ in nine different situations. The panels a), e)

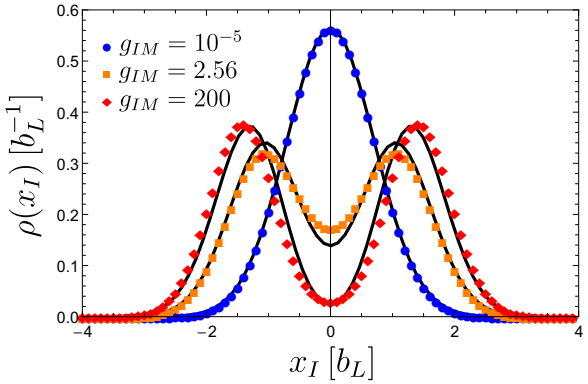


*Figure 9.7: One-body correlation function for the impurity boson in the four particle system with three different impurity-majority interaction strengths. The black solid lines show the results obtained through exact diagonalization. In all cases we consider* $g_{MM} = 10^{-5}$.

and i), along the diagonal in Fig. 9.8 have equal interactions between all the pairs. For the non-interacting a) and strongly repulsive i) densities we approximately reproduce the two cases shown in Fig. 9.1 a). Panel e) shows the intermediate case, with the depletion of probability along the planes $\{x_I = x_{M1}$, $x_I = x_{M2}$, $x_{M1} = x_{M2}\}$, in a similar way as shown in [147]. The off-diagonal densities are clearly not symmetric: in the column a), d) and g), only the interaction $g_{MM}$ is being increased. That means the probability is lowered only along the plane $\{x_{M1} = x_{M2}\}$, which leads to the separation of the density in two lobes. On the other hand, the line a), b), c) shows depletion of the probability on two planes, namely $\{x_I = x_{M1}$, $x_I = x_{M2}\}$, which leads to the appearance of a smaller lobe on b). The mixed cases f) and h) also reflect the asymmetry of the interactions on the probability densities.

## 9.4 Conclusions

We have used a pair correlated wave function, based on the solution for a pair of bosons in a trap, to access the features of the problem of few bosons in the presence of an impurity. We have shown that this wave function reproduces the limiting cases of zero interaction and infinite repulsion between the atoms. The results for intermediate interactions are consistent with the qualitative behavior expected for these systems. By increasing the interaction between the impurity and the remaining pair, we show that there is a tendency for this atom to occupy some position around the edges the trap. These effects on the spatial correlations are also reflected on quantities of experimental interest, such as the momentum distribution and the Fourier transform of the pair correlations. We also extend the approach to a case of three identical bosons and one impurity and compare results for the one-body densities with exact

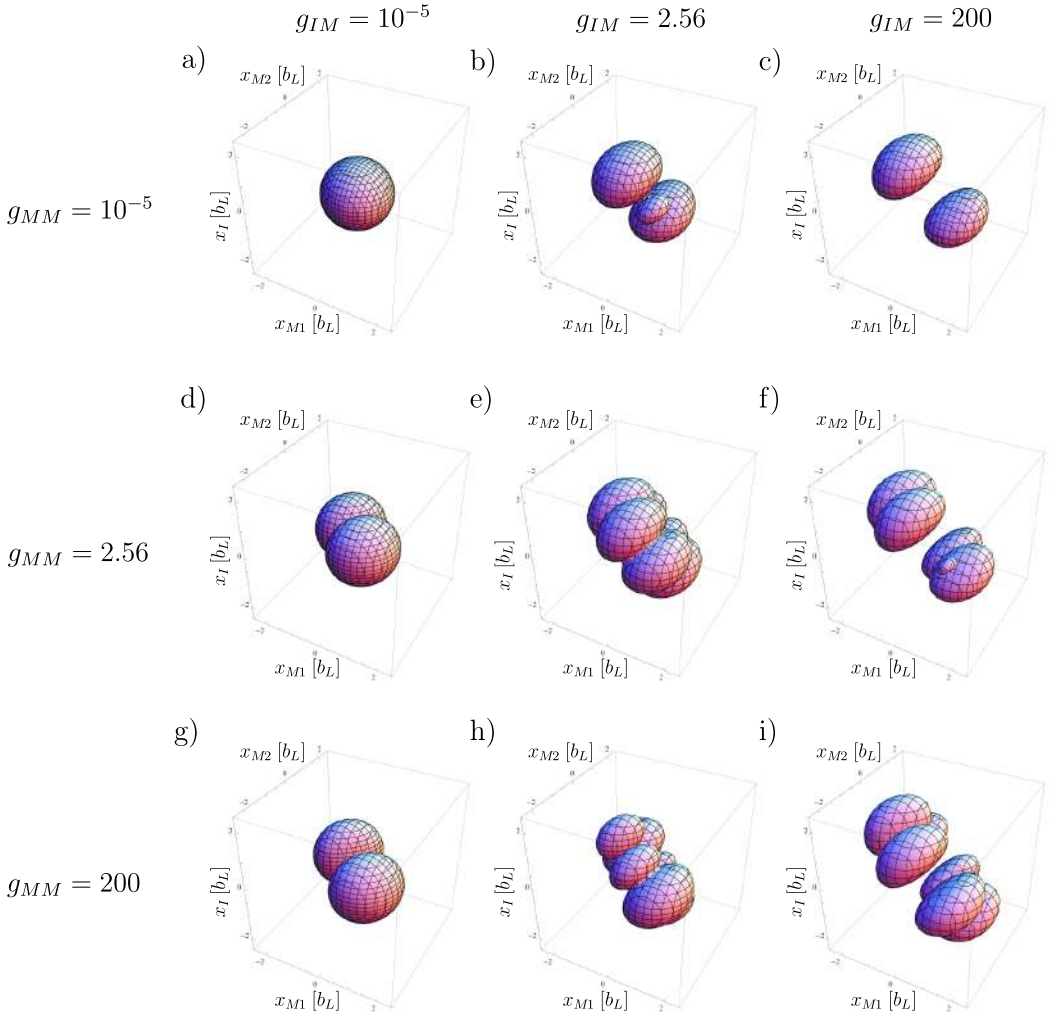


*Figure 9.8: Normalized total density $|\Psi(x_I, x_{M1}, x_{M2})|^2$ shows the depletion of the probability along the contact manifolds for different interactions. The repulsion between the majority-majority pair and the impurity-majority pairs is increased from top to bottom and left to right, respectively.*

numerical results. It becomes clear that by combining a pair-correlated wave function with variational optimization it is possible to address other systems of great interest, such as balanced mixtures of two or more bosonic species.

# Chapter 10

# A mean-field approach to spin-charge separation in two-component Bose gases

In Chapter 7 we explored the phenomenon of spin-charge separation in a few-body fermionic system with strong interactions. In the many-body regime, this effect has been theoretically treated with different approaches: the Luttinger liquid model [93], the Bethe ansatz approach [96, 154] and the Density Matrix Renormalization Group (DMRG) [94, 95]. An experimental study of spin-charge separation for two-component Bose gases has been presented in Ref. [56].

Here, we develop a numerical study based on the Gross-Pitaevskii (GP) equation [5, 6] for the propagation of charge and spin excitations in a two-component Bose gas. We show that our results agree with the predicitions from hydrodynamic theory. We further propose probing these effects in the presence of a harmonic trap by simulating the dynamics of the system after a sudden change in the trapping frequency.

## 10.1 Model and Hamiltonian

We consider a many-body Bose gas trapped in a quasi-1D geometry at zero temperature. We assume that the gas has two internal states and define the two components as $\uparrow$ and $\downarrow$. The numbers of particles in each component are written as $N_\uparrow$ and $N_\downarrow$, with the total number of particles given by $N = N_\uparrow + N_\downarrow$. In the mean-field limit, this system can be modelled by two coupled Gross-

Pitaevskii (GP) equations:

$$i\hbar\frac{\partial\psi_\uparrow(x)}{\partial t} = \left(-\frac{\hbar^2}{2m_\uparrow}\frac{\partial^2}{\partial x^2} + V(x) + G_{\uparrow\uparrow}|\psi_\uparrow(x)|^2 + G_{\downarrow\uparrow}|\psi_\downarrow(x)|^2\right)\psi_\uparrow(x)$$
$$i\hbar\frac{\partial\psi_\downarrow(x)}{\partial t} = \left(-\frac{\hbar^2}{2m_\downarrow}\frac{\partial^2}{\partial x^2} + V(x) + G_{\downarrow\downarrow}|\psi_\downarrow(x)|^2 + G_{\uparrow\downarrow}|\psi_\uparrow(x)|^2\right)\psi_\downarrow(x), \quad (10.1)$$

where $V(x)$ is an external trapping potential, which will be discussed below. The third term on the right-hand side of the equations ($G_{\uparrow\uparrow}, G_{\downarrow\downarrow}$) is related to the intraspecies interactions for each component, and the remaining terms ($G_{\uparrow\downarrow}, G_{\downarrow\uparrow}$) denote the interspecies interactions. We consider the wave functions $\psi_{(\uparrow,\downarrow)}(x)$ to be normalized to unity, while the interaction terms are scaled to the number of particles: this gives us $G_{\uparrow\uparrow} = N_\uparrow g_{\uparrow\uparrow}$, $G_{\downarrow\downarrow} = N_\downarrow g_{\downarrow\downarrow}$, $G_{\downarrow\uparrow} = N_\downarrow g_{\uparrow\downarrow}$ and $G_{\uparrow\downarrow} = N_\uparrow g_{\uparrow\downarrow}$, where $g_{\uparrow\uparrow}$, $g_{\downarrow\downarrow}$ and $g_{\uparrow\downarrow}$ are the "bare" interactions. In the following, we shall consider that the two components have the same masses ($m_\uparrow = m_\downarrow = m$), and that the intraspecies interactions are the same ($g_{\uparrow\uparrow} = g_{\downarrow\downarrow} = g$). We focus on repulsive interactions ($g, g_{\uparrow\downarrow} > 0$) and take, for simplicity, $\hbar = m = 1$. We will also assume a balanced system, where $N_\uparrow = N_\downarrow$, which gives us $G_{\uparrow\uparrow} = G_{\downarrow\downarrow} = G$ and $G_{\uparrow\downarrow} = G_{\downarrow\uparrow}$.

For the trapping potential $V(x)$, we assume a hard-wall box of length $L$. This is done so that the densities for the two components, $n_\uparrow(x) = N_\uparrow|\psi_\uparrow(x)|^2$ and $n_\downarrow(x) = N_\downarrow|\psi_\downarrow(x)|^2$ are approximately constant near the center of the system. For these constant densities we will simply use the notation $n_\uparrow$, $n_\downarrow$ or $n$, the latter referring to the single component gas. In our calculations, we consider all quantities in the units of the trapping potential: length, time and velocity are given in units of $L$, $t_B = 2mL^2/(\hbar\pi^2)$ and $v_0 = \hbar^2\pi^2/(2mL)$, respectively.

The Gross-Pitaevskii equation is assumed to be valid for small values of the parameter $\gamma = mg/n$. For large densities, the system is in the so-called Thomas-Fermi regime [6]. For smaller densities and $g \gg 1$, the system is in the strogly repulsive Tonks-Girardeau limit, which is beyond the range of our approach. Here, we focus on systems with large densities and relatively small values of the interaction parameter $g$. In our calculations, we use the split-step Crank-Nicolson method [88, 155], with the imaginary time evolution method applied to creating steady states of the system and with the real time evolution method applied to simulate the dynamics. A similar approach to the one adopted here, with a focus on stability and phase separation of two component Bose gases, is presented by Vidanović *et. al.* in Ref. [156].

## 10.2 Density perturbations and spin-charge separation

### 10.2.1 Single component

We first turn to the simple case of a single component in the box, for which we create a density perturbation and obtain its propagation velocity. A detailed study of the propagation of perturbations in a Bose gas at lower densities has been performed in Ref. [94]. Here, we reproduce the expected results in the GP regime to validate our approach for the case of two component gases. In the single component scenario, instead of two coupled GP equations as given in Eq. (10.1), we have a single equation with the interspecies interaction term dropped. We create a gaussian perturbation to the density in the center of the system, described by

$$V_p(x) = \epsilon \exp(-x^2/2\sigma), \tag{10.2}$$

where we consider $\sigma = 2$ and $\epsilon < 0$, which induces a bump in the density of the cloud at $x = 0$.

A steady state for the system in the presence of the perturbation is prepared using the imaginary-time evolution with the Crank-Nicolson method. With this we are able to calculate the average density $n(0)$ near the center of the trap, where the perturbation is placed. At $t = 0$ the perturbation is switched off. In Fig. 10.1 we show the time evolution of the density $n(x)$. The bump initially placed in the middle of the system splits into two perturbations that travel at the same velocity in opposite directions.

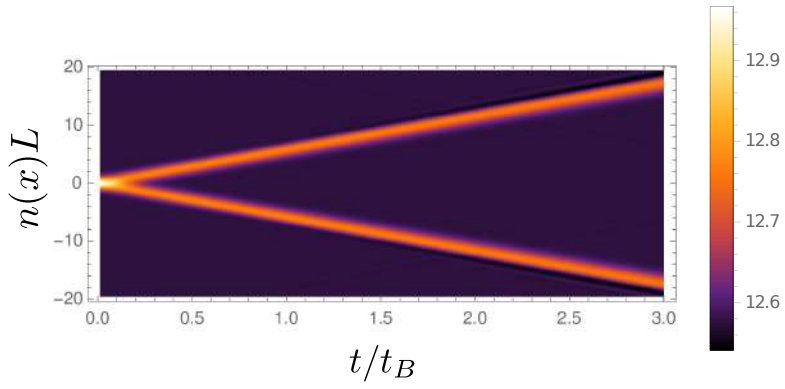


*Figure 10.1: Time evolution of the density perturbation in the single component Bose gas. The parameters used are $n \approx 12.5$, $g = 2.5$, and $\epsilon = -1$.*

For the time scales shown in Fig. 10.1, the density perturbations have not yet reached the edges of the system and there are no visible signs of boundary effects and interference. For an infinitesimal perturbation ($\epsilon \ll 1$)

it is predicted by the hydrodinamic approach [5] that the perturbation should propagate at the Bogoliubov speed of sound:

$$c = \sqrt{\frac{gn}{m}}. \tag{10.3}$$

We can compare the propagation of the density excitations to this result by considering a small perturbation and registering the velocity of the density peaks as seen in Fig. 10.1. In Fig. 10.2 we show a comparison of our results to the theoretical predictions. In Eq. (10.3) the density is assumed to be the average density near the center of the trap.

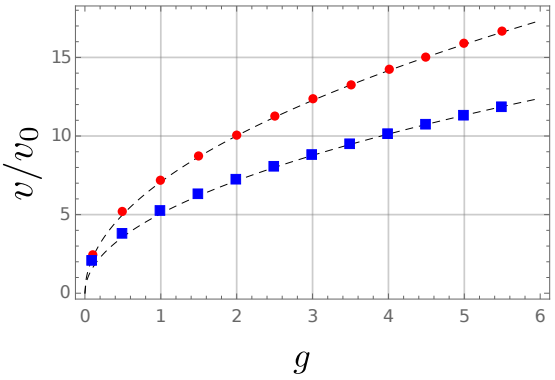


*Figure 10.2: Comparison between the propagation velocity of the perturbations (symbols) and the sound velocity predicted by hydrodinamic theory (dashed lines). The red circles are the results for $n \approx 50$ and the blue squares for $n \approx 25$. In both cases we consider $\epsilon = -0.1$.*

We see that our results agree well with the behavior expected from Eq. (10.3) up to intermediate values of $g$, provided that the value of $\gamma$ remains small enough. For all points, we have a deviation of at least 0.1 between the theoretical sound velocity and the perturbation velocity obtained from the simulations. This is due to the fact that the perturbations, while very small, still have a finite amplitude, which leads to propagation velocities larger than the sound velocity. This effect is more pronounced at small values of $g$, where the perturbation originated by Eq. (10.2) induces a larger bump in the gas density. Therefore, for a fixed value of $\epsilon$, we find better agreement with the sound velocity predictions for large values of the GP non-linear term $G = Ng$.

### 10.2.2 Two components

We now focus on the dynamics of two-component Bose gases in a box. The different species can be realized experimentally exploring different hyperfine atomic states (e.g. $|F = 2, m_F = -1\rangle$ and $|F = 1, m_F = 1\rangle$ in $^{87}$Rb). As a first example, we create a steady state in the presence of a spin-selective perturbation given by Eq. (10.2), which affects only one of the components

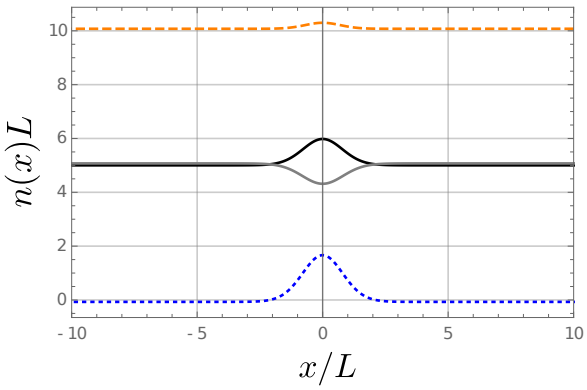


*Figure 10.3: Initial profiles for the densities of the two-component system. The solid curves refer to $n_\uparrow(x)$ (black) and $n_\downarrow(x)$ (gray), while the dashed orange curve and the blue dotted curve refer to $n_C(x)$ and $n_S(x)$, respectively.*

(we choose $\uparrow$). We further define a "charge" density as $n_C(x) = n_\uparrow(x) + n_\downarrow(x)$ and a "spin" density as $n_C(x) = n_\uparrow(x) - n_\downarrow(x)$. In Fig. 10.3, we show the steady state densities for the charge, spin and the two components in the presence of the perturbation, at $t = 0$.

As in the single component case, the perturbation induces a bump in $n_\uparrow(x)$. Due to the repulsive interactions, this leads to a depletion of density, or a dimp, in the distribution of $n_\downarrow(x)$. The combined effect of these distributions lead to perturbations of different amplitudes in the charge and spin densities (notice that the spin density perturbation is very small). At $t = 0$, we turn off the spin-selective potential, which leads to the propagation of the perturbations in the background gas. In Fig. 10.4 we show the results for the time evolution for the charge and spin densities.

It becomes clear than the charge and spin density perturbations travel at different velocities. This difference is expected to become larger as the system approaches the transition to phase separation ($g_{\uparrow\downarrow} > g$), where ferromagnetic interactions are dominant. For the particular case of $g_{\uparrow\downarrow} = g$, we expect to find a complete freezing of the spin degree of freedom as compared to the propagation of charge perturbations. This regime has been analitically explored with the Bethe ansatz in Ref. [96, 154]. The sound velocities for the two component case can also be obtained by the hydrodynamic approximation:

$$v_{c,s} = c\sqrt{1 \pm \frac{g_{\uparrow\downarrow}}{g}}, \tag{10.4}$$

where $c$ is the single component velocity of sound, and the indices $c$ and $s$ refer to charge and spin. In Fig. 10.5 we show a comparison for the velocity of propagation of charge and spin perturbations to the results predicted by Eq. 10.4. It is important to note that the velocity of the charge perturbation is obtained by applying the potential given by Eq. 10.2 to *both* components).

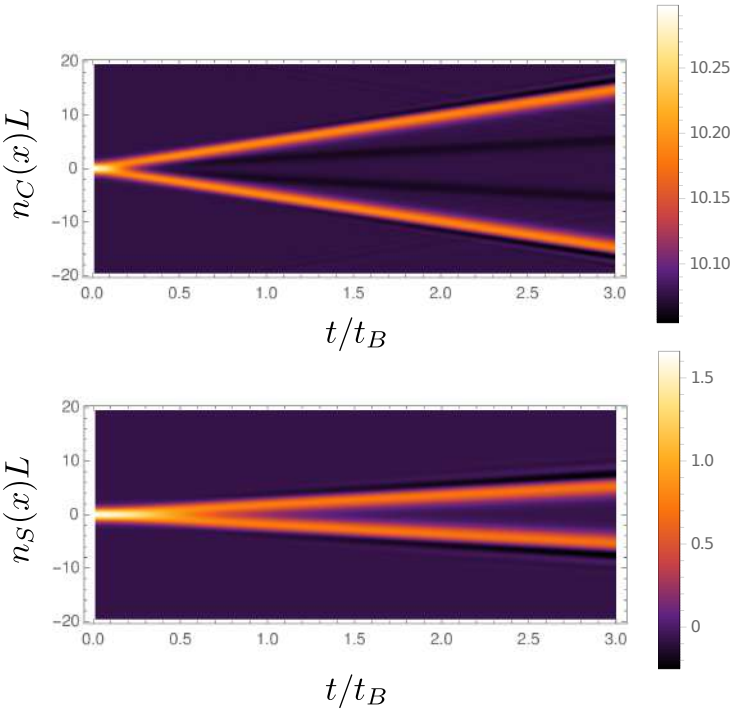


*Figure 10.4: Time evolution of the charge (top) and spin (bottom) densities. The parameters considered are* $n \approx 5$, $g = 2.5$, $g_{\uparrow\downarrow} = 2.0$ *and* $\epsilon = -1$.

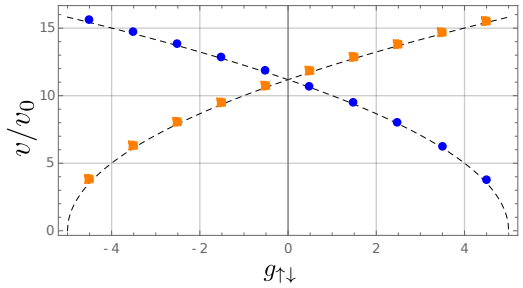


*Figure 10.5: Comparison between the charge (orange squares) and spin (blue circles) perturbation velocities and the sound velocities predicted by Eq. 10.4. The parameters used are* $n \approx 25$ *and* $\epsilon = -0.1$.

Once again we find good agreement up to intermediate values of $g_{\uparrow\downarrow}$, with a fixed intraspecies interaction strength of $g = 5$. The small deviations observed in the single component case, due to the finite size of the perturbations, are also present here. These results can be qualitatively compared to the ones obtained for lower densities beyond the hydrodynamic description in Ref. [95, 157]. We further highlight the fact that large densities (as considered in the single component case), which lead to strong non-linearities in the GP equation, can induce instabilities in the dynamics of the the two-component, coupled GP equations. More reliable results are obtained for the smaller densities shown in Figs. 10.4 and 10.5.

### 10.2.3 Two component Bose gas in a harmonic trap

We now extend our approach to the case where the two-component Bose gas is confined by a harmonic trap given by $V(x) = m\omega^2 x^2/2$, where $\omega$ is the trap frequency. Length and time are now given in units of the harmonic oscillator length $l_H = \sqrt{\hbar/m\omega}$ and the inverse frequency $t_H = \omega^{-1}$.

It has been shown that spin-charge separation is also manifested in the presence of a harmonic trap [157]. However, the dynamics of small perturbations may be hard to register for these trapping geometries, since the spatial distributions are inhomogeneous. Instead, here we consider a two-component system confined by spin-selective trapping frequencies $\omega_\uparrow$ and $\omega_\downarrow$. We prepare a steady state at $t/t_H < 0$ considering $\omega_\uparrow = \omega_\downarrow$. At $t/t_H = 0$, we switch the frequency of one of the components, such that $\omega_\uparrow > \omega_\downarrow$, and at $t/t_H \approx 0.5$ we switch back. The sudden changes in the trapping frequency for one of the components induce oscillations in the distributions over time. These “trap quenches" have been adopted in the hydrodynamic description to simulate monopole oscillations in a Bose gas over a wide range of interactions [158]. Here, the oscillations are extended to both components due to the interspecies repulsion. To quantify this oscillatory behavior, we keep track of the “charge" and “spin" squared widths $w^2_{C,S} = w^2_\uparrow \pm w^2_\downarrow$, where

$$w^2_{\uparrow,\downarrow} = \int |\psi_{\uparrow,\downarrow}(x)|^2 x^2 dx \tag{10.5}$$

is the squared width for a single component. These monopole oscillations in the width of the atomic cloud after trap quenches are also often called “breathing modes" [159, 160].

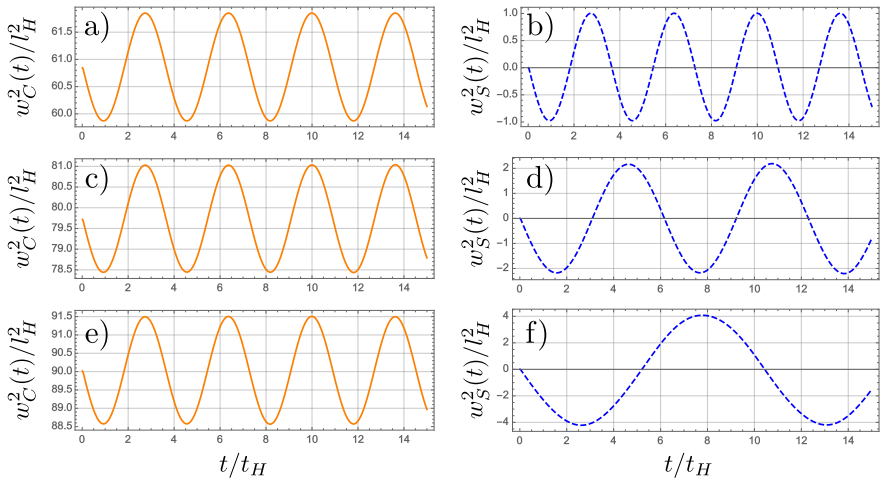


*Figure 10.6: Time-evolution of the charge (solid orange curves) and spin (dashed blue curves) squared widths for $g = 5.0$ and a)-b) $g_{\uparrow\downarrow} = 0$, c)-d) $g_{\uparrow\downarrow} = 2.5$ and e)-f) $g_{\uparrow\downarrow} = 4.0$.*

In Fig. 10.6 we show the results for $w_C^2(t)$ and $w_S^2(t)$, with the intraspecies interactions fixed as $g = 5$ and for different values of the $g_{\uparrow\downarrow}$. We immediately notice that increasing $g_{\uparrow\downarrow}$ has little effect on the dynamics of the charge sector other than an increase of the average width of the cloud. The spin oscillations, however, are highly affected by this parameter; we see that, as $g_{\uparrow\downarrow}$ is increased, the frequency of these oscillations is lowered (in the case of $g_{\uparrow\downarrow} = 0$, the spin and charge oscillations naturally have the same frequency as the two components are decoupled). We could expect these spin oscillations to would completely freeze for $g_{\uparrow\downarrow} \to \infty$ (this regime is not, however, realistically treated within the Gross-Pitaevskii approach).

### 10.2.4 Numerical details

In our simulations we obtain the steady states and the dynamics for the two-components Bose gas using the split-step Crank-Nicolson method [155]. The trapping potential considered is a box of length $L$ centered at $x = 0$. We discretize the system with a grid size of $dx = 0.05$, and consider the half-length $L/2 = 25$. Outside these limits, we impose $V(x) \gg 1$ so that the boundaries are effective hard walls. The size of the time step used in our simulations is $\Delta t = 10^{-4}$, except in the case of the coupled GP equations at large densities (e.g. Fig. 10.5) where instabilities arise due to the large values of the non-linearities; in this cases, we consider $\Delta t = 0.25 \times 10^{-4}$. The steady states and dynamics are obtained using a total number of time steps of around $3 \times 10^4$. In the harmonically trapped system, we consider a total size of $L = 25$, with the same discretization parameters. The quench is performed by considering $\omega_\uparrow = 1.25\omega_\downarrow$.

## 10.3 Conclusions

In this chapter, we have performed a study of spin-charge separation in a two-component one-dimensional bose gas. Contrary to Chapter 7, where we focused on a few-body system with strong interactions, here we explore the many-body case where interactions are weak enought to be treated with the Gross-Pitaevskii equation. Our initial step consists of obtaining results using a quench protocol which is similar to previous studies with DMRG [94, 95]. We show that, in the single-component case, our results match the predictions of Bogoliubov theory for the velocity of propagation of perturbations.

We then extend the same approach to the two-component case, where we find that spin-charge separation is also manifested in the mean-field regime. Once again, the results agree with the expected behavior obtained from the hydrodynamic approximation.

To address the problem in the context of experiments with trapped cold atoms, we further propose the case of a two-component Bose gas in a harmonic trap. In this geometry, our quench protocol consists of suddenly changing the trap frequency for one of the components, therefore inducing breathing modes in the densities. By calculating the time-evolution of the charge and spin densities we are able to obtain different oscillation frequencies for these quantities, which also depend on the strength of the repulsion between the two-components.

# Chapter 11

# Conclusion and Final Remarks

We now present a brief summary of the work presented in each of the chapters of this thesis, along with some remarks on the potential developments of the subjects considered here.

The first part of the thesis is dedicated to an overview of the field of cold atoms and the tools we employ in our studies. In the Introduction we provided general information on the types of systems we take under consideration, namely one-dimensional quantum systems of interacting particles. A major part of the renewed interest in this theoretical field of study is due to the advances in experiments with trapped cold atoms, where several parameters can be manipulated with precision. Numerous different theoretical proposals appeared as a consequence of the possibilities presented by these experiments. The combined effort of theory and experiment has given rise to a rich area that draws insight from quantum and statistical mechanics, as well as atomic, molecular and optical physics.

Chapter 2 lays out the general theory that is applied throughout the thesis. The main goal of the chapter is to describe the mapping between a strongly interacting system of atoms in one dimension and a spin chain, where the spin states represent internal atomic degrees of freedom. We additionally present a section dealing with the experimental details involved in realizing one-dimensional systems of cold atoms, including recent experiments exploring their exotic properties.

In the second and main part of the thesis we focus on presenting our studies of dynamical effects in strongly interacting one-dimensional systems. In Chapter 3 we show how transitions between magnetic profiles can be obtained by considering a two-component Bose gas where a single parameter - the instraspecies interaction strength - is slowly changed in time. This simple protocol allows for the manipulation of magnetic correlations in the system, and the same procedure could in principle be extended to many-body ensem-

bles.

In Chapter 4 we study the case of a strongly interacting bosonic system in the presence of a single impurity. We show that, by changing the strength of the background repulsion (which is essentially the same parameter we manipulate in Chapter 3), we can greatly affect the dynamics of the impurity. In fact, in a certain regime of interactions, the impurity presents an oscillatory behavior that resembles a Josephson junction, even in the abscence of a potential barrier. Additionally, we find that the barrier can enhance the tunneling of the impurity in some particular cases, and provide an analysis of this phenomenon through the interpretation of the energy gaps of the system.

In Chapter 5 we explore a more exotic possibility, where a two-component Bose gas has a set of completely independent interaction parameters between the two species. We show results for the spin densities in this system, considering a homogeneous potential and several combinations of interactions. One of these specific combinations allows a minority set of spins to travel through the system as an effective wave packet, an effect that could have applications in the study of spin state transfer in long one-dimensional chains.

Chapter 6 presents an intermediate study in which we consider a spin chain where one of the exchange coefficients is time-dependent. This model configures a gateway into the exploration of time-periodic and externally driven spin systems, which are currently the object of great interest in the physics community. By comparing numerical and analytical results, we show how we can apply Floquet theory to predict the dynamical behavior of the observables in this system.

In Chapter 7 we apply the methods above to the study of the dynamics of a multicomponent few-body Fermi gas after a sudden change in the trapping potential. We show how the time-evolution of the spatial sector provides us with a set of time-dependent exchange coefficients for the spin chain. Combining the contribution of each sector, we obtain the time-evolution of the spin densities, which show separate signals for charge and spin dynamics. Interestingly, the spin excitations can again be predicted by the energy gaps in the Floquet quasienergy spectrum of a spin chain with time periodicity. We additionally study the possibility of increasing the number of internal components and the effect of doing so on the dynamics of the system. When the number of internal states matches the number of atoms, we find that the spin oscillations vanish and the system can be accurately described as a gas of impenetrable bosons.

In Chapter 8 we take under consideration a different type of driven system, where we analyze the response of a spin chain to an external spin-flip drive. We provide details on the driving protocol and show that a bosonic system is able to sustain, in a certain regime, the type of behavior expected for a time crystal phase, where discrete time-translation symmetry is non-trivially broken. This effect is shown to be robust against imperfections in the drive, and is also present in a larger system in a lattice.

The third part of the thesis is concerned with two alternative studies where we explore different regimes of interactions and particle number. Chapter 9 presents static results for a few-body Bose mixture in a trap, where we apply a variational approach to obtain the ground state wave function over a large interval of interactions. We compare our results to numerical diagonalization and show that we are able to reproduce the expected behavior for different quantities, such as spatial densities and momentum distribution.

In Chapter 10 we go back to the effect of spin-charge separation, this time employing the Gross-Pitaevskii description of a many-body Bose gas. We begin by comparing the behavior of a perturbation in the single-component Bose gas with the predictions of Bogoliubov theory. Then we extend our study to the two-component case by numerically solving a set of coupled Gross-Pitaevskii equations. Finally, we provide a proposal of a quench protocol suited for the observation of spin-charge separation in a harmonically trapped system.

The work presented in this thesis takes into account only a small fraction of the possiblities offered by experiments with trapped cold atoms. Recent studies are continuously pushing the boundaries of the field, either considering different geometries and combinations of internal states or taking into account out-of-equilibrium systems, where the Hamiltonian is modified by external fields. Furthermore, using cold atoms as quantum simulators may provide insight on models belonging to fields as diverse as condensed matter and particle physics. The models studied in this thesis have also become the object of experiments with superconducting circuits, where similar chains of spins can be built and controlled with precision. These platforms will certainly contribute for future advances in basic physics research as well as in the design of quantum devices.

# Part IV

# Appendices

# Appendix A

# Numerical methods

In this appendix we present some details on the numerical methods used for simulations of dynamics throughout this work. In the first section we provide a brief description of the well-known Crank-Nicolson method, which is commonly used for simulations of dynamics in quantum mechanics. In the second part we describe the lattice Hamiltonian we consider when simulating the continuum and comparing to the spin chain results in Chapter 2.

## A.1 Crank-Nicolson method

Throughout this thesis, we present several cases of simulations in dynamics which frequently deal with sudden changes in the potential or even time-dependent Hamiltonians. To address these problems, we use an implementation of the Crank-Nicolson method [88, 155]. The basic idea behind this method is rather simple [161]. We assume that, for a small time step $\Delta t$, the wave function evolves as

$$\psi(t+\Delta t) = e^{-iH\Delta t}\psi(t), \tag{A.1}$$

where we assume $\hbar = 1$. By simply expanding the exponential to first order we obtain

$$\psi(t+\Delta t) = 1 - iH\Delta t\psi(t). \tag{A.2}$$

However, this simple expression does not preserver unitarity. To fix this, we can split the time evolution operator as

$$\psi(t+\Delta t) = e^{\frac{-iH\Delta t}{2}} e^{\frac{-iH\Delta t}{2}} \psi(t), \tag{A.3}$$

and multiply both sides of the expression by $e^{\frac{iH\Delta t}{2}}$ to get

$$e^{\frac{iH\Delta t}{2}} \psi(t+\Delta t) = e^{\frac{-iH\Delta t}{2}} \psi(t). \tag{A.4}$$

We now expand the exponentials to first order to obtain the time-evolution of the wave function with Cayley's form

$$\psi(t+\Delta t) \approx \frac{1-\frac{1}{2}iH\Delta t}{1+\frac{1}{2}iH\Delta t}\psi(t), \tag{A.5}$$

which can also be written as

$$\left(1+\frac{1}{2}iH\Delta t\right)\psi(t+\Delta t) = \left(1-\frac{1}{2}iH\Delta t\right)\psi(t). \tag{A.6}$$

Since we aim to describe a discrete system, we define the matrix $A = 1+\frac{1}{2}iH\Delta t$ and write the wave function vector as $\Psi^n$, where $n$ now denotes the time step parameter. We have, therefore

$$A\cdot\Psi^{n+1} = A^*\cdot\Psi^n, \tag{A.7}$$

which leads to

$$\Psi^{n+1} = A^{-1}A^*\cdot\Psi^n. \tag{A.8}$$

By iteratively applying this operator to an initial wave vector, we are able to approximate the exact time-evolution of the system, even for time-dependent Hamiltonians. The Crank-Nicolson method is characterized by a second order error in the time step, which is negligible for $\Delta t \ll 1$. In our simulations, we usually employ $\Delta t = 2.5\times10^{-3}$, unless stated otherwise. One important point regarding this method is that, if $A$ is a tridiagonal matrix, the computation time can be greatly reduced by exploring the Thomas algorithm [162]. This is the case for $N+1$ spin chains, where only one anti-aligned spin is considered, or in the case of the discretized Gross-Pitaevskii equation.

We now apply this formalism to dynamical simulations of a Heisenberg chain, after the wave function is initialized in an arbitrary state. The Hamiltonian is simply defined by

$$H = -J\sum_{i=1}^{N-1}\frac{1}{2}\left(1-\vec{\sigma}^i\cdot\vec{\sigma}^{i+1}\right), \tag{A.9}$$

where we fix the exchange coefficients $J=1$. We choose a $N=6$ system, with two different combinations of spins: 3+3 and 5+1. In the first case, the time-evolution of the system is obtained with the Crank-Nicolson method, as described above. In the second, the Hamiltonian matrix can be reduced to a tridiagonal shape and the Thomas algorithm is employed. In Fig. A.1 a) and b) we show the comparison for the overlap probability $F(t) = |\langle\psi_0|\psi(t)\rangle|^2$ between the exact and the numerical time-evolution of the system. The exact result is obtained from

$$|\psi(t)\rangle = \sum_{n=1}^{N_s} c_n e^{-iE_nt}|\phi_n\rangle, \tag{A.10}$$

where $N_s$ denotes the total number of eigenstates $|\phi_n\rangle$ and $E_n$ are the corresponding eingenvalues. The initial states are given by $\psi_0 = |\uparrow\uparrow\uparrow\downarrow\downarrow\downarrow\rangle$ in the 3+3 case and by $\psi_0 = |\uparrow\uparrow\uparrow\uparrow\uparrow\downarrow\rangle$ in the 5+1 case.

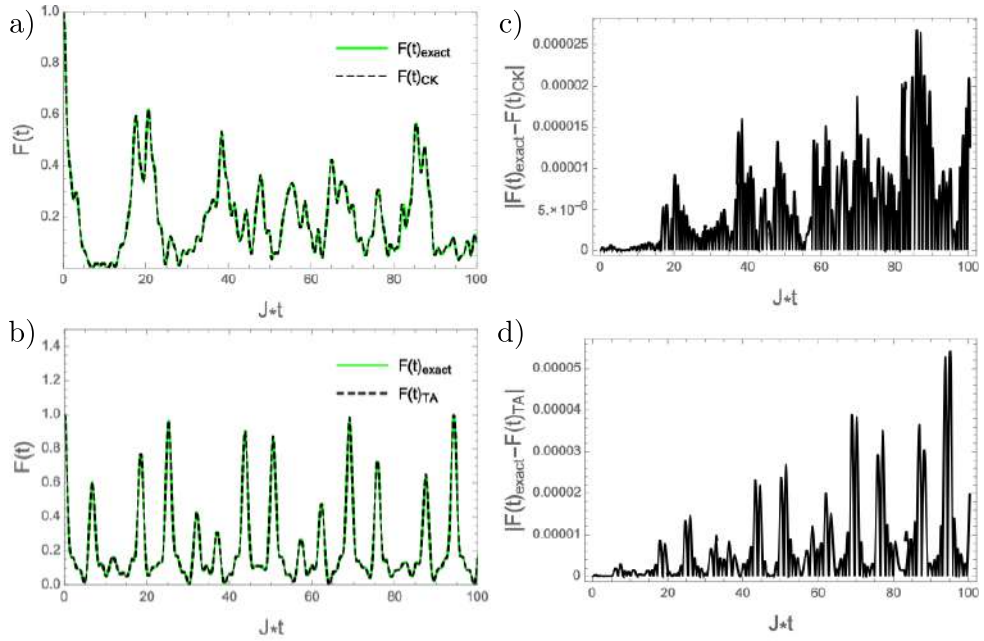


*Figure A.1: Time-evolution of a) $\psi_0 = |\uparrow\uparrow\uparrow\downarrow\downarrow\downarrow\rangle$ and b) $\psi_0 = |\uparrow\uparrow\uparrow\uparrow\uparrow\downarrow\rangle$, as given by Hamiltonian* (A.9)*. The solid green curve shows the exact results from Eq.* (A.10)*, while the dashed black curves show the numerical resuts. In c) and d) we present the increase in the error of $F(t)$ between the numerical and exact approaches.*

Besides applying the Crank-Nicolson method to the time-evolution of spin chains with time-dependent Hamiltonians, we also use it, in Chapter 10, to solve the Gross-Pitaevskii equation decribing a many-body one-dimensional Bose gas. In this case, the Hamiltonian includes a self-interaction term which depends on the wave function, which also makes in time-dependent. Furthermore, we employ the imaginary-time version of the code [155] to obtain the steady states used in the description of the initial wave function in quench protocols.

## A.2 Matrix Product States

To validate the mapping of a strongly interacting two-component gas in one dimension to a spin chain Hamiltonian, in Chapter 2 we have compared results for the spin densities obtained with this method to numerical results stemming from simulations with Matrix Product States (MPS). In this section we provide details on the construction of the Hamiltonian and the mapping between a

lattice model and the continuum. We focus on the description for a two-component fermionic gas obeying the Fermi-Hubbard Hamiltonian [94], but the case of bosons [95] can be also considered by including the corresponding interaction terms in the theoretical description. The lattice Hamiltonian for a fermionic gas with two internal components is given by

$$H = -t\sum_{j,\sigma}(c^{\dagger}_{j+1,\sigma}c_{j,\sigma} + \text{H.c.}) + U\sum_{j} n_{j,\uparrow}n_{j,\downarrow} + \sum_{j,\sigma}\epsilon_j n_{j,\sigma}, \tag{A.11}$$

where $c^{\dagger}$ and $c$ are the creation and annihilation operators, respectively, $t$ is the hopping parameter and $U$ denotes the stregnth of the on-site interactions between fermions with different spin projections. Additionally, we include a term for the external potential $\epsilon_j$ which depends on the position.

To simulate the continuum, we choose a system length of $2L$ and a total number of sites $M$, which defines the lattice spacing as $a = 2l/M$. The mapping between the lattice and the continuum models is done by taking $t = \frac{1}{2ma^2}$, and $U = \frac{g}{a}$ where $m$ is the mass of the atoms and $g$ is the interaction strength in the continuum. For simplicity, we again consider $m = \hbar = 1$. We simulate an external harmonic trap with $\epsilon_j = \frac{1}{2}m\omega^2 x_j^2$ where $x_j$ is the discretized position variable. To match the energies to the continuum, we must additionally include in the Hamiltonian a term given by $\sum_{j,\sigma} 1/a^2$. As mentioned in Chapter 2, the simulations are performed with the open source Python package OpenMPS [51, 163]. For these static simulations we define a tolerance for the variance of $\Delta E = 10^{-5}$ and a maximum bond dimension of $\chi = 500$.

# Appendix B

# Generators of SU(3) and SU(4) symmetries

In this chapter we present the matrix expressions for the SU(3) and SU(4) generators used in Chapter 7. We additionally show the expressions for the ladder operators of SU(3) symmetry.

## B.1 SU(3)

The 8 generators for the SU(3) symmetry (Gell-Mann matrices [117]) are given by:

$$\lambda^1 = \begin{pmatrix} 0 & 1 & 0 \\ 1 & 0 & 0 \\ 0 & 0 & 0 \end{pmatrix}, \quad \lambda^2 = \begin{pmatrix} 0 & -i & 0 \\ i & 0 & 0 \\ 0 & 0 & 0 \end{pmatrix}, \quad \lambda^3 = \begin{pmatrix} 1 & 0 & 0 \\ 0 & -1 & 0 \\ 0 & 0 & 0 \end{pmatrix},$$

$$\lambda^4 = \begin{pmatrix} 0 & 0 & 1 \\ 0 & 0 & 0 \\ 1 & 0 & 0 \end{pmatrix}, \quad \lambda^5 = \begin{pmatrix} 0 & 0 & -i \\ 0 & 0 & 0 \\ i & 0 & 0 \end{pmatrix}, \quad \lambda^6 = \begin{pmatrix} 0 & 0 & 0 \\ 0 & 0 & 1 \\ 0 & 1 & 0 \end{pmatrix},$$

$$\lambda^7 = \begin{pmatrix} 0 & 0 & 0 \\ 0 & 0 & -i \\ 0 & i & 0 \end{pmatrix}, \quad \lambda^8 = \frac{1}{\sqrt{3}} \begin{pmatrix} 1 & 0 & 0 \\ 0 & 1 & 0 \\ 0 & 0 & -2 \end{pmatrix}.$$

When studying the effects of symmetry breaking in the dynamics of the SU(3) system, we consider also the action of the raising and lowering operators given by

$$
\begin{aligned}
T^+ &= \begin{pmatrix} 0 & 1 & 0 \\ 0 & 0 & 0 \\ 0 & 0 & 0 \end{pmatrix}, \quad T^- = \begin{pmatrix} 0 & 0 & 0 \\ 1 & 0 & 0 \\ 0 & 0 & 0 \end{pmatrix}, \\
V^+ &= \begin{pmatrix} 0 & 0 & 1 \\ 0 & 0 & 0 \\ 0 & 0 & 0 \end{pmatrix}, \quad V^- = \begin{pmatrix} 0 & 0 & 0 \\ 0 & 0 & 0 \\ 1 & 0 & 0 \end{pmatrix}, \\
U^+ &= \begin{pmatrix} 0 & 0 & 0 \\ 0 & 0 & 1 \\ 0 & 0 & 0 \end{pmatrix}, \quad U^- = \begin{pmatrix} 0 & 0 & 0 \\ 0 & 0 & 0 \\ 0 & 1 & 0 \end{pmatrix}.
\end{aligned}
$$

## B.2 SU(4)

The 15 generators for the SU(4) symmetry are given by

$$\lambda^1 = \begin{pmatrix} 0 & 1 & 0 & 0 \\ 1 & 0 & 0 & 0 \\ 0 & 0 & 0 & 0 \\ 0 & 0 & 0 & 0 \end{pmatrix}, \quad \lambda^2 = \begin{pmatrix} 0 & -i & 0 & 0 \\ i & 0 & 0 & 0 \\ 0 & 0 & 0 & 0 \\ 0 & 0 & 0 & 0 \end{pmatrix},$$

$$\lambda^3 = \begin{pmatrix} 1 & 0 & 0 & 0 \\ 0 & -1 & 0 & 0 \\ 0 & 0 & 0 & 0 \\ 0 & 0 & 0 & 0 \end{pmatrix}, \quad \lambda^4 = \begin{pmatrix} 0 & 0 & 1 & 0 \\ 0 & 0 & 0 & 0 \\ 1 & 0 & 0 & 0 \\ 0 & 0 & 0 & 0 \end{pmatrix},$$

$$\lambda^5 = \begin{pmatrix} 0 & 0 & -i & 0 \\ 0 & 0 & 0 & 0 \\ i & 0 & 0 & 0 \\ 0 & 0 & 0 & 0 \end{pmatrix}, \quad \lambda^6 = \begin{pmatrix} 0 & 0 & 0 & 0 \\ 0 & 0 & 1 & 0 \\ 0 & 1 & 0 & 0 \\ 0 & 0 & 0 & 0 \end{pmatrix},$$

$$\lambda^7 = \begin{pmatrix} 0 & 0 & 0 & 0 \\ 0 & 0 & -i & 0 \\ 0 & i & 0 & 0 \\ 0 & 0 & 0 & 0 \end{pmatrix}, \quad \lambda^8 = \frac{1}{\sqrt{3}} \begin{pmatrix} 1 & 0 & 0 & 0 \\ 0 & 1 & 0 & 0 \\ 0 & 0 & -2 & 0 \\ 0 & 0 & 0 & 0 \end{pmatrix},$$

$$\lambda^9 = \begin{pmatrix} 0 & 0 & 0 & 1 \\ 0 & 0 & 0 & 0 \\ 0 & 0 & 0 & 0 \\ 1 & 0 & 0 & 0 \end{pmatrix}, \quad \lambda^{10} = \begin{pmatrix} 0 & 0 & 0 & -i \\ 0 & 0 & 0 & 0 \\ 0 & 0 & 0 & 0 \\ i & 0 & 0 & 0 \end{pmatrix},$$

$$\lambda^{11} = \begin{pmatrix} 0 & 0 & 0 & 0 \\ 0 & 0 & 0 & 1 \\ 0 & 0 & 0 & 0 \\ 0 & 1 & 0 & 0 \end{pmatrix}, \quad \lambda^{12} = \begin{pmatrix} 0 & 0 & 0 & 0 \\ 0 & 0 & 0 & -i \\ 0 & 0 & 0 & 0 \\ 0 & i & 0 & 0 \end{pmatrix},$$

$$\lambda^{13} = \begin{pmatrix} 0 & 0 & 0 & 0 \\ 0 & 0 & 0 & 0 \\ 0 & 0 & 0 & 1 \\ 0 & 0 & 1 & 0 \end{pmatrix}, \quad \lambda^{14} = \begin{pmatrix} 0 & 0 & 0 & 0 \\ 0 & 0 & 0 & 0 \\ 0 & 0 & 0 & -i \\ 0 & 0 & i & 0 \end{pmatrix},$$

$$\lambda^{15} = \frac{1}{\sqrt{6}} \begin{pmatrix} 1 & 0 & 0 & 0 \\ 0 & 1 & 0 & 0 \\ 0 & 0 & 1 & 0 \\ 0 & 0 & 0 & -3 \end{pmatrix}.$$

# Bibliography


[1] K. B. Davis, M. O. Mewes, M. R. Andrews, N. J. van Druten, D. S. Durfee, D. M. Kurn, and W. Ketterle, "Bose-Einstein condensation in a gas of sodium atoms," *Phys. Rev. Lett.*, vol. 75, pp. 3969–3973, Nov 1995. 3, 19

[2] M. H. Anderson, J. R. Ensher, M. R. Matthews, C. E. Wieman, and E. A. Cornell, "Observation of bose-einstein condensation in a dilute atomic vapor," *Science*, vol. 269, no. 5221, pp. 198–201, 1995. 3, 19

[3] W. D. Phillips, "Nobel lecture: Laser cooling and trapping of neutral atoms," *Rev. Mod. Phys.*, vol. 70, pp. 721–741, Jul 1998. 3, 19

[4] W. Ketterle and N. V. Druten, "Evaporative cooling of trapped atoms," vol. 37 of *Advances In Atomic, Molecular, and Optical Physics*, pp. 181 – 236, Academic Press, 1996. 3, 19

[5] L. Pitaevskii and S. Stringari, *Bose-Einstein Condensation*. International Series of Monographs on Physics, Clarendon Press, 2003. 3, 93, 96

[6] C. Pethick and H. Smith, *Bose-Einstein Condensation in Dilute Gases*. Cambridge University Press, 2002. 3, 4, 20, 93, 94

[7] R. Pathria and P. Beale, *Statistical Mechanics*. Elsevier Science, 2011. 3

[8] M. Takahashi, *Thermodynamics of One-Dimensional Solvable Models*. Cambridge University Press, 2005. 3, 4

[9] E. Merzbacher, *Quantum Mechanics*. Wiley, 1998. 3, 34

[10] J. Sakurai and J. Napolitano, *Modern Quantum Mechanics*. Cambridge University Press, 2017. 3

[11] M. Inguscio and L. Fallani, *Atomic Physics: Precise Measurements and Ultracold Matter*. OUP Oxford, 2013. 3, 19

[12] C. Monroe, W. Swann, H. Robinson, and C. Wieman, "Very cold trapped atoms in a vapor cell," *Phys. Rev. Lett.*, vol. 65, pp. 1571–1574, Sep 1990. 3

[13] I. Bloch, "Ultracold quantum gases in optical lattices," *Nat Phys*, vol. 1, pp. 23–30, Oct 2005. 3, 76

[14] C. Chin, R. Grimm, P. Julienne, and E. Tiesinga, "Feshbach resonances in ultracold gases," *Rev. Mod. Phys.*, vol. 82, pp. 1225–1286, Apr 2010. 3, 20, 72, 82

[15] M. Olshanii, "Atomic scattering in the presence of an external confinement and a gas of impenetrable bosons," *Phys. Rev. Lett.*, vol. 81, pp. 938–941, Aug 1998. 3, 21, 72, 82

[16] T. Giamarchi, *Quantum Physics in One Dimension*. International Series of Monogr, Clarendon Press, 2004. 4

[17] E. H. Lieb and W. Liniger, "Exact analysis of an interacting Bose gas. i. the general solution and the ground state," *Phys. Rev.*, vol. 130, pp. 1605–1616, May 1963. 4, 8, 82

[18] E. H. Lieb, "Exact analysis of an interacting Bose gas. ii. the excitation spectrum," *Phys. Rev.*, vol. 130, pp. 1616–1624, May 1963. 4, 8, 82

[19] J. B. McGuire, "Interacting fermions in one dimension. i. repulsive potential," *Journal of Mathematical Physics*, vol. 6, no. 3, pp. 432–439, 1965. 4

[20] J. B. McGuire, "Interacting fermions in one dimension. ii. attractive potential," *Journal of Mathematical Physics*, vol. 7, no. 1, pp. 123–132, 1966. 4

[21] M. Gaudin, "Un systeme a une dimension de fermions en interaction," *Physics Letters A*, vol. 24, no. 1, pp. 55 – 56, 1967. 4

[22] C. N. Yang, "Some exact results for the many-body problem in one dimension with repulsive delta-function interaction," *Phys. Rev. Lett.*, vol. 19, pp. 1312–1315, Dec 1967. 4

[23] M. Gaudin and J. Caux, *The Bethe Wavefunction*. Cambridge University Press, 2014. 4

[24] M. Albiez, R. Gati, J. Fölling, S. Hunsmann, M. Cristiani, and M. K. Oberthaler, "Direct observation of tunneling and nonlinear self-trapping in a single bosonic Josephson junction," *Phys. Rev. Lett.*, vol. 95, p. 010402, Jun 2005. 4

[25] B. Paredes, A. Widera, V. Murg, O. Mandel, S. Folling, I. Cirac, G. V. Shlyapnikov, T. W. Hansch, and I. Bloch, "Tonks-Girardeau gas of ultracold atoms in an optical lattice," *Nature*, vol. 429, pp. 277–281, May 2004. 4, 21

[26] T. Kinoshita, T. Wenger, and D. S. Weiss, "Observation of a one-dimensional Tonks-Girardeau gas," *Science*, vol. 305, no. 5687, pp. 1125–1128, 2004. 21

[27] E. Haller, M. Gustavsson, M. J. Mark, J. G. Danzl, R. Hart, G. Pupillo, and H.-C. Nägerl, "Realization of an excited, strongly correlated quantum gas phase," *Science*, vol. 325, no. 5945, pp. 1224–1227, 2009. 4, 21, 34

[28] G. Zürn, F. Serwane, T. Lompe, A. N. Wenz, M. G. Ries, J. E. Bohn, and S. Jochim, "Fermionization of two distinguishable fermions," *Phys. Rev. Lett.*, vol. 108, p. 075303, Feb 2012. 4, 21, 76

[29] S. Murmann, A. Bergschneider, V. M. Klinkhamer, G. Zürn, T. Lompe, and S. Jochim, "Two fermions in a double well: Exploring a fundamental building block of the Hubbard model," *Phys. Rev. Lett.*, vol. 114, p. 080402, Feb 2015. 4, 21, 57

[30] A. N. Wenz, G. Zürn, S. Murmann, I. Brouzos, T. Lompe, and S. Jochim, "From few to many: Observing the formation of a Fermi sea one atom at a time," *Science*, vol. 342, no. 6157, pp. 457–460, 2013. 4, 55

[31] T. Busch, B.-G. Englert, K. Rzażewski, and M. Wilkens, "Two cold atoms in a harmonic trap," *Foundations of Physics*, vol. 28, no. 4, pp. 549–559, 1998. 4, 81, 82, 83

[32] F. Deuretzbacher, K. Fredenhagen, D. Becker, K. Bongs, K. Sengstock, and D. Pfannkuche, "Exact solution of strongly interacting quasi-one-dimensional spinor Bose gases," *Phys. Rev. Lett.*, vol. 100, p. 160405, Apr 2008. 4, 11

[33] L. Guan, S. Chen, Y. Wang, and Z.-Q. Ma, "Exact solution for infinitely strongly interacting Fermi gases in tight waveguides," *Phys. Rev. Lett.*, vol. 102, p. 160402, Apr 2009. 35

[34] A. G. Volosniev, D. V. Fedorov, A. S. Jensen, M. Valiente, and N. T. Zinner, "Strongly interacting confined quantum systems in one dimension," *Nature Communications*, vol. 5, pp. 5300 EP –, Nov 2014. Article. 4, 72

[35] T. Kinoshita, T. Wenger, and D. S. Weiss, "A quantum Newton's cradle," *Nature*, vol. 440, pp. 900–903, Apr 2006. 4

[36] G. Pagano, M. Mancini, G. Cappellini, P. Lombardi, F. Schäfer, H. Hu, X.-J. Liu, J. Catani, C. Sias, M. Inguscio, and L. Fallani, "A one-dimensional liquid of fermions with tunable spin," *Nature Physics*, vol. 10, pp. 198–201, 3 2014. 4, 21, 56, 65, 76

[37] B. K. Stuhl, H.-I. Lu, L. M. Aycock, D. Genkina, and I. B. Spielman, "Visualizing edge states with an atomic Bose gas in the quantum Hall regime," *Science*, vol. 349, no. 6255, pp. 1514–1518, 2015. 4, 21, 56, 76

[38] M. Mancini, G. Pagano, G. Cappellini, L. Livi, M. Rider, J. Catani, C. Sias, P. Zoller, M. Inguscio, M. Dalmonte, and L. Fallani, "Observation of chiral edge states with neutral fermions in synthetic Hall ribbons," *Science*, vol. 349, no. 6255, pp. 1510–1513, 2015. 4, 21, 56, 76

[39] S. Murmann, F. Deuretzbacher, G. Zürn, J. Bjerlin, S. M. Reimann, L. Santos, T. Lompe, and S. Jochim, "Antiferromagnetic Heisenberg spin chain of a few cold atoms in a one-dimensional trap," *Phys. Rev. Lett.*, vol. 115, p. 215301, Nov 2015. 4, 29, 57

[40] I. Bloch, J. Dalibard, and S. Nascimbène, "Quantum simulations with ultracold quantum gases," *Nature Physics*, vol. 8, pp. 267 EP –, Apr 2012. Review Article. 4

[41] C. Gross and I. Bloch, "Quantum simulations with ultracold atoms in optical lattices," *Science*, vol. 357, no. 6355, pp. 995–1001, 2017. 4

[42] R. E. Barfknecht, A. Foerster, and N. T. Zinner, "Emergence of junction dynamics in a strongly interacting bose mixture," *New Journal of Physics*, vol. 20, no. 6, p. 063014, 2018. 7, 33

[43] P. A. M. Dirac, "On the Theory of Quantum Mechanics," *Proceedings of the Royal Society of London Series A*, vol. 112, pp. 661–677, Oct. 1926. 8

[44] M. Girardeau, "Relationship between systems of impenetrable bosons and fermions in one dimension," *Journal of Mathematical Physics*, vol. 1, no. 6, pp. 516–523, 1960. 9, 83

[45] A. Lenard, "Momentum Distribution in the Ground State of the One-Dimensional System of Impenetrable Bosons," *Journal of Mathematical Physics*, vol. 5, pp. 930–943, July 1964. 9

[46] A. G. Volosniev, D. Petrosyan, M. Valiente, D. V. Fedorov, A. S. Jensen, and N. T. Zinner, "Engineering the dynamics of effective spin-chain models for strongly interacting atomic gases," *Phys. Rev. A*, vol. 91, p. 023620, Feb 2015. 12, 26, 36, 38, 46, 55, 73

[47] N. J. S. Loft, O. V. Marchukov, D. Petrosyan, and N. T. Zinner, "Tunable self-assembled spin chains of strongly interacting cold atoms for demonstration of reliable quantum state transfer," *New Journal of Physics*, vol. 18, no. 4, p. 045011, 2016. 14, 17, 36, 46

[48] N. Loft, L. Kristensen, A. Thomsen, A. Volosniev, and N. Zinner, "CONAN—the cruncher of local exchange coefficients for strongly interacting confined systems in one dimension," *Computer Physics Communications*, vol. 209, pp. 171 – 182, 2016. 16, 17, 40

[49] F. Deuretzbacher, D. Becker, and L. Santos, "Momentum distributions and numerical methods for strongly interacting one-dimensional spinor gases," *Phys. Rev. A*, vol. 94, p. 023606, Aug 2016. 16

[50] O. V. Marchukov, A. G. Volosniev, M. Valiente, D. Petrosyan, and N. T. Zinner, "Quantum spin transistor with a heisenberg spin chain," *Nature Communications*, vol. 7, pp. 13070 EP –, Oct 2016. Article. 17, 26

[51] D. Jaschke, M. L. Wall, and L. D. Carr, "Open source matrix product states: Opening ways to simulate entangled many-body quantum systems in one dimension," *Computer Physics Communications*, vol. 225, pp. 59 – 91, 2018. 17, 112

[52] P. Massignan, J. Levinsen, and M. M. Parish, "Magnetism in strongly interacting one-dimensional quantum mixtures," *Phys. Rev. Lett.*, vol. 115, p. 247202, Dec 2015. 18, 25, 26, 28, 35, 50

[53] `https://www.uibk.ac.at/exphys/ultracold/?https://www.uibk.ac.at/exphys/ultracold/projects/cs3/index1.html`. Ultracold atoms and quantum gases homepage - University of Innsbruck (accessed: 2018-11-20). 20

[54] E. Haller, M. J. Mark, R. Hart, J. G. Danzl, L. Reichsöllner, V. Melezhik, P. Schmelcher, and H.-C. Nägerl, "Confinement-induced resonances in low-dimensional quantum systems," *Phys. Rev. Lett.*, vol. 104, p. 153203, Apr 2010. 21

[55] D. S. Hall, M. R. Matthews, J. R. Ensher, C. E. Wieman, and E. A. Cornell, "Dynamics of component separation in a binary mixture of Bose-Einstein condensates," *Phys. Rev. Lett.*, vol. 81, pp. 1539–1542, Aug 1998. 21

[56] P. Wicke, S. Whitlock, and N. J. van Druten, "Controlling spin motion and interactions in a one-dimensional Bose gas," *ArXiv e-prints*, Oct. 2010. 21, 93

[57] A. Dehkharghani, A. Volosniev, J. Lindgren, J. Rotureau, C. Forssén, D. Fedorov, A. Jensen, and N. Zinner, "Quantum magnetism in strongly interacting one-dimensional spinor Bose systems," *Scientific Reports*, vol. 5, pp. 10675 EP –, Jun 2015. Article. 25, 27, 86, 88

[58] R. E. Barfknecht, A. Foerster, and N. T. Zinner, "Dynamical realization of magnetic states in a strongly interacting Bose mixture," *Phys. Rev. A*, vol. 95, p. 023612, Feb 2017. 25

[59] L. Yang and X. Cui, "Effective spin-chain model for strongly interacting one-dimensional atomic gases with an arbitrary spin," *Phys. Rev. A*, vol. 93, p. 013617, Jan 2016. 26, 44, 45, 55, 76

[60] A. S. Dehkharghani, A. G. Volosniev, and N. T. Zinner, "Quantum impurity in a one-dimensional trapped Bose gas," *Phys. Rev. A*, vol. 92, p. 031601, Sep 2015. 26, 35, 88

[61] Y. J. Hao and S. Chen, "Ground-state properties of interacting two-component Bose gases in a one-dimensional harmonic trap," *The European Physical Journal D*, vol. 51, no. 2, pp. 261–266, 2009. 28, 35

[62] J. R. Anglin and A. Vardi, "Dynamics of a two-mode Bose-Einstein condensate beyond mean-field theory," *Phys. Rev. A*, vol. 64, p. 013605, May 2001. 33

[63] A. P. Tonel, J. Links, and A. Foerster, "Quantum dynamics of a model for two Josephson-coupled Bose–Einstein condensates," *Journal of Physics A: Mathematical and General*, vol. 38, no. 6, p. 1235, 2005.

[64] J. Links, A. Foerster, A. P. Tonel, and G. Santos, "The two-site Bose-Hubbard model," *Annales Henri Poincaré*, vol. 7, pp. 1591–1600, Dec 2006.

[65] D. Masiello, S. B. McKagan, and W. P. Reinhardt, "Multiconfigurational Hartree-Fock theory for identical bosons in a double well," *Phys. Rev. A*, vol. 72, p. 063624, Dec 2005.

[66] M. A. Garcia-March and T. Busch, "Quantum gas mixtures in different correlation regimes," *Phys. Rev. A*, vol. 87, p. 063633, Jun 2013. 33

[67] S. Zöllner, H.-D. Meyer, and P. Schmelcher, "Tunneling dynamics of a few bosons in a double well," *Phys. Rev. A*, vol. 78, p. 013621, Jul 2008. 33, 39

[68] I. Brouzos, A. I. Streltsov, A. Negretti, R. S. Said, T. Caneva, S. Montangero, and T. Calarco, "Quantum speed limit and optimal control of many-boson dynamics," *Phys. Rev. A*, vol. 92, p. 062110, Dec 2015.

[69] T. Sowiński, M. Gajda, and K. Rzażewski, "Diffusion in a system of a few distinguishable fermions in a one-dimensional double-well potential," *EPL (Europhysics Letters)*, vol. 113, no. 5, p. 56003, 2016.

[70] J. Dobrzyniecki and T. Sowiński, "Exact dynamics of two ultra-cold bosons confined in a one-dimensional double-well potential," *The European Physical Journal D*, vol. 70, p. 83, Apr 2016.

[71] M. Tylutki, G. E. Astrakharchik, and A. Recati, "Coherent oscillations in small Fermi polaron systems," *eprint arXiv:1706.09466*, June 2017. 33, 60

[72] B. Josephson, "Possible new effects in superconductive tunnelling," *Physics Letters*, vol. 1, no. 7, pp. 251 – 253, 1962. 33

[73] P. W. Anderson and J. M. Rowell, "Probable observation of the Josephson superconducting tunneling effect," *Phys. Rev. Lett.*, vol. 10, pp. 230–232, Mar 1963. 33

[74] K. Sakmann, A. I. Streltsov, O. E. Alon, and L. S. Cederbaum, "Exact quantum dynamics of a bosonic Josephson junction," *Phys. Rev. Lett.*, vol. 103, p. 220601, Nov 2009. 33

[75] R. Gati and M. K. Oberthaler, "A bosonic Josephson junction," *Journal of Physics B: Atomic, Molecular and Optical Physics*, vol. 40, no. 10, p. R61, 2007. 33

[76] L. Guan and S. Chen, "Super-Tonks-Girardeau gas of spin-1/2 interacting fermions," *Phys. Rev. Lett.*, vol. 105, p. 175301, Oct 2010. 34

[77] M. A. García-March, A. Yuste, B. Juliá-Díaz, and A. Polls, "Mesoscopic superpositions of tonks-girardeau states and the bose-fermi mapping," *Phys. Rev. A*, vol. 92, p. 033621, Sep 2015. 35

[78] F. Deuretzbacher, D. Becker, J. Bjerlin, S. M. Reimann, and L. Santos, "Quantum magnetism without lattices in strongly interacting one-dimensional spinor gases," *Phys. Rev. A*, vol. 90, p. 013611, Jul 2014. 35, 55, 72, 73

[79] E. J. Lindgren, J. Rotureau, C. Forssén, A. G. Volosniev, and N. T. Zinner, "Fermionization of two-component few-fermion systems in a one-dimensional harmonic trap," *New Journal of Physics*, vol. 16, no. 6, p. 063003, 2014.

[80] L. Yang, L. Guan, and H. Pu, "Strongly interacting quantum gases in one-dimensional traps," *Phys. Rev. A*, vol. 91, p. 043634, Apr 2015. 35, 55

[81] X.-W. Guan, M. T. Batchelor, and M. Takahashi, "Ferromagnetic behavior in the strongly interacting two-component Bose gas," *Phys. Rev. A*, vol. 76, p. 043617, Oct 2007. 35, 45

[82] G. M. Nikolopoulos, D. Petrosyan, and P. Lambropoulos, "Coherent electron wavepacket propagation and entanglement in array of coupled quantum dots," *EPL (Europhysics Letters)*, vol. 65, no. 3, p. 297, 2004. 36

[83] M. Christandl, N. Datta, A. Ekert, and A. J. Landahl, "Perfect state transfer in quantum spin networks," *Phys. Rev. Lett.*, vol. 92, p. 187902, May 2004. 36

[84] R. E. Barfknecht, A. Foerster, and N. T. Zinner, "Effects of interaction imbalance in a strongly repulsive one-dimensional bose gas," *Few-Body Systems*, vol. 59, p. 22, Mar 2018. 43

[85] J. Decamp, P. Armagnat, B. Fang, M. Albert, A. Minguzzi, and P. Vignolo, "Exact density profiles and symmetry classification for strongly interacting multi-component fermi gases in tight waveguides," *New Journal of Physics*, vol. 18, no. 5, p. 055011, 2016. 44

[86] E. K. Laird, Z.-Y. Shi, M. M. Parish, and J. Levinsen, "SU($N$) fermions in a one-dimensional harmonic trap," *Phys. Rev. A*, vol. 96, p. 032701, Sep 2017. 44, 55, 58, 76

[87] F. Deuretzbacher, D. Becker, J. Bjerlin, S. M. Reimann, and L. Santos, "Spin-chain model for strongly interacting one-dimensional Bose-Fermi mixtures," *Phys. Rev. A*, vol. 95, p. 043630, Apr 2017. 46, 48

[88] J. Crank and P. Nicolson, "A practical method for numerical evaluation of solutions of partial differential equations of the heat-conduction type," *Advances in Computational Mathematics*, vol. 6, pp. 207–226, Dec 1996. 49, 60, 94, 109

[89] G. Floquet, "Sur les équations différentielles linéaires à coefficients périodiques," *Annales scientifiques de l'École Normale Supérieure*, vol. 12, pp. 47–88, 1883. 49, 50, 71

[90] J. R. Johansson, P. D. Nation, and F. Nori, "Qutip 2: A Python framework for dynamics of open quantum systems," *Comp. Phys. Comm.*, vol. 184, no. 4, pp. 1234–1240, 2013. 50

[91] A. Eckardt and E. Anisimovas, "High-frequency approximation for periodically driven quantum systems from a Floquet-space perspective," *New Journal of Physics*, vol. 17, no. 9, p. 093039, 2015. 50

[92] F. D. M. Haldane, "'Luttinger liquid theory' of one-dimensional quantum fluids. I. properties of the Luttinger model and their extension to the general 1d interacting spinless Fermi gas," *Journal of Physics C: Solid State Physics*, vol. 14, no. 19, p. 2585, 1981. 55

[93] A. Recati, P. O. Fedichev, W. Zwerger, and P. Zoller, "Spin-charge separation in ultracold quantum gases," *Phys. Rev. Lett.*, vol. 90, p. 020401, Jan 2003. 55, 93

[94] C. Kollath, U. Schollwöck, and W. Zwerger, "Spin-charge separation in cold Fermi gases: A real time analysis," *Phys. Rev. Lett.*, vol. 95, p. 176401, Oct 2005. 55, 93, 95, 101, 112

[95] A. Kleine, C. Kollath, I. P. McCulloch, T. Giamarchi, and U. Schollwöck, "Spin-charge separation in two-component Bose gases," *Phys. Rev. A*, vol. 77, p. 013607, Jan 2008. 55, 93, 99, 101, 112

[96] J. N. Fuchs, D. M. Gangardt, T. Keilmann, and G. V. Shlyapnikov, "Spin waves in a one-dimensional spinor Bose gas," *Phys. Rev. Lett.*, vol. 95, p. 150402, Oct 2005. 55, 93, 97

[97] A. G. Volosniev, H.-W. Hammer, and N. T. Zinner, "Simulation of time-dependent Heisenberg models in one dimension," *Phys. Rev. B*, vol. 93, p. 094414, Mar 2016. 55

[98] L. Yang and H. Pu, "Bose-Fermi mapping and a multibranch spin-chain model for strongly interacting quantum gases in one dimension: Dynamics and collective excitations," *Phys. Rev. A*, vol. 94, p. 033614, Sep 2016. 55

[99] E. Haller, R. Hart, M. J. Mark, J. G. Danzl, L. Reichsollner, M. Gustavsson, M. Dalmonte, G. Pupillo, and H.-C. Nagerl, "Pinning quantum phase transition for a luttinger liquid of strongly interacting bosons," *Nature*, vol. 466, pp. 597–600, Jul 2010. 55

[100] B. Yang, Y.-Y. Chen, Y.-G. Zheng, H. Sun, H.-N. Dai, X.-W. Guan, Z.-S. Yuan, and J.-W. Pan, "Quantum criticality and the Tomonaga-Luttinger liquid in one-dimensional Bose gases," *Phys. Rev. Lett.*, vol. 119, p. 165701, Oct 2017.

[101] M. Lebrat, P. Grišins, D. Husmann, S. Häusler, L. Corman, T. Giamarchi, J.-P. Brantut, and T. Esslinger, "Band and correlated insulators of cold fermions in a mesoscopic lattice," *Phys. Rev. X*, vol. 8, p. 011053, Mar 2018. 55

[102] O. M. Auslaender, H. Steinberg, A. Yacoby, Y. Tserkovnyak, B. I. Halperin, K. W. Baldwin, L. N. Pfeiffer, and K. W. West, "Spin-charge separation and localization in one dimension," *Science*, vol. 308, no. 5718, pp. 88–92, 2005. 55

[103] T. A. Hilker, G. Salomon, F. Grusdt, A. Omran, M. Boll, E. Demler, I. Bloch, and C. Gross, "Revealing hidden antiferromagnetic correlations in doped hubbard chains via string correlators," *Science*, vol. 357, no. 6350, pp. 484–487, 2017. 55

[104] T. L. Yang, P. Grišins, Y. T. Chang, Z. H. Zhao, C. Y. Shih, T. Giamarchi, and R. G. Hulet, "Measurement of the dynamical structure factor of a 1d interacting fermi gas," *Phys. Rev. Lett.*, vol. 121, p. 103001, Sep 2018. 55

[105] I. Titvinidze, A. Privitera, S.-Y. Chang, S. Diehl, M. A. Baranov, A. Daley, and W. Hofstetter, "Magnetism and domain formation in SU(3)-symmetric multi-species Fermi mixtures," *New Journal of Physics*, vol. 13, no. 3, p. 035013, 2011. 56

[106] A. Golubeva, A. Sotnikov, A. Cichy, J. Kuneš, and W. Hofstetter, "Breaking of SU(4) symmetry and interplay between strongly correlated phases in the Hubbard model," *Phys. Rev. B*, vol. 95, p. 125108, Mar 2017. 56

[107] J. C. Pati and A. Salam, "Lepton number as the fourth "color"," *Phys. Rev. D*, vol. 10, pp. 275–289, Jul 1974. 56

[108] R. E. Barfknecht, A. Foerster, and N. T. Zinner, "Signatures of spin-charge separation," 2018. 56

[109] A. Minguzzi and D. M. Gangardt, "Exact coherent states of a harmonically confined Tonks-Girardeau gas," *Phys. Rev. Lett.*, vol. 94, p. 240404, Jun 2005. 59

[110] F. Cartarius, E. Kawasaki, and A. Minguzzi, "Dynamical depinning of a Tonks-Girardeau gas," *Phys. Rev. A*, vol. 92, p. 063605, Dec 2015. 59

[111] K. Singh, K. M. Fujiwara, Z. A. Geiger, E. Q. Simmons, M. Lipatov, A. Cao, P. Dotti, S. V. Rajagopal, R. Senaratne, T. Shimasaki, M. Heyl, A. Eckardt, and D. M. Weld, "Controlling and characterizing Floquet prethermalization in a driven quantum system," *ArXiv e-prints*, Sept. 2018. 59

[112] C. K. Lai, "Lattice gas with nearest-neighbor interaction in one dimension with arbitrary statistics," *Journal of Mathematical Physics*, vol. 15, no. 10, pp. 1675–1676, 1974. 63

[113] B. Sutherland, "Model for a multicomponent quantum system," *Phys. Rev. B*, vol. 12, pp. 3795–3805, Nov 1975. 63

[114] A. Schmitt, K.-H. Mütter, and M. Karbach, "The spin-1 Lai-Sutherland model with external and internal fields: I. the phase diagram," *Journal of Physics A: Mathematical and General*, vol. 29, no. 14, p. 3951, 1996. 63

[115] M. Aguado, M. Asorey, E. Ercolessi, F. Ortolani, and S. Pasini, "Density-matrix renormalization-group simulation of the $SU(3)$ antiferromagnetic heisenberg model," *Phys. Rev. B*, vol. 79, p. 012408, Jan 2009. 63

[116] N. L. Harshman, M. Olshanii, A. S. Dehkharghani, A. G. Volosniev, S. G. Jackson, and N. T. Zinner, "Integrable families of hard-core particles with unequal masses in a one-dimensional harmonic trap," *Phys. Rev. X*, vol. 7, p. 041001, Oct 2017. 64

[117] W. Pfeifer, *The Lie Algebras SU(N): An Introduction*. Birkhäuser Basel, 2003. 64, 113

[118] F. Wilczek, "Quantum time crystals," *Phys. Rev. Lett.*, vol. 109, p. 160401, Oct 2012. 71

[119] A. Shapere and F. Wilczek, "Classical time crystals," *Phys. Rev. Lett.*, vol. 109, p. 160402, Oct 2012. 71

[120] T. Li, Z.-X. Gong, Z.-Q. Yin, H. T. Quan, X. Yin, P. Zhang, L.-M. Duan, and X. Zhang, "Space-time crystals of trapped ions," *Phys. Rev. Lett.*, vol. 109, p. 163001, Oct 2012. 71

[121] P. Bruno, "Comment on "space-time crystals of trapped ions"," *Phys. Rev. Lett.*, vol. 111, p. 029301, Jul 2013. 71

[122] P. Bruno, "Comment on "Quantum time crystals"," *Phys. Rev. Lett.*, vol. 110, p. 118901, Mar 2013. 71

[123] P. Bruno, "Impossibility of spontaneously rotating time crystals: A no-go theorem," *Phys. Rev. Lett.*, vol. 111, p. 070402, Aug 2013. 71

[124] H. Watanabe and M. Oshikawa, "Absence of quantum time crystals," *Phys. Rev. Lett.*, vol. 114, p. 251603, Jun 2015. 71

[125] V. Khemani, A. Lazarides, R. Moessner, and S. L. Sondhi, "Phase structure of driven quantum systems," *Phys. Rev. Lett.*, vol. 116, p. 250401, Jun 2016. 71

[126] D. V. Else, B. Bauer, and C. Nayak, "Floquet time crystals," *Phys. Rev. Lett.*, vol. 117, p. 090402, Aug 2016.

[127] K. Sacha and J. Zakrzewski, "Time crystals: a review," *Reports on Progress in Physics*, vol. 81, no. 1, p. 016401, 2018. 71

[128] C. W. von Keyserlingk, V. Khemani, and S. L. Sondhi, "Absolute stability and spatiotemporal long-range order in floquet systems," *Phys. Rev. B*, vol. 94, p. 085112, Aug 2016. 71

[129] V. Khemani, C. W. von Keyserlingk, and S. L. Sondhi, "Defining time crystals via representation theory," *Phys. Rev. B*, vol. 96, p. 115127, Sep 2017. 71

[130] N. Y. Yao and C. Nayak, "Time crystals in periodically driven systems," *Physics Today*, vol. 71, no. 9, pp. 40–47, 2018. 71

[131] K. Sacha, "Modeling spontaneous breaking of time-translation symmetry," *Phys. Rev. A*, vol. 91, p. 033617, Mar 2015. 71

[132] N. Y. Yao, A. C. Potter, I.-D. Potirniche, and A. Vishwanath, "Discrete time crystals: Rigidity, criticality, and realizations," *Phys. Rev. Lett.*, vol. 118, p. 030401, Jan 2017. 71, 76

[133] S. Choi, J. Choi, R. Landig, G. Kucsko, H. Zhou, J. Isoya, F. Jelezko, S. Onoda, H. Sumiya, V. Khemani, C. von Keyserlingk, N. Y. Yao, E. Demler, and M. D. Lukin, "Observation of discrete time-crystalline order in a disordered dipolar many-body system," *Nature*, vol. 543, pp. 221 EP –, Mar 2017. 72, 74

[134] J. Zhang, P. W. Hess, A. Kyprianidis, P. Becker, A. Lee, J. Smith, G. Pagano, I.-D. Potirniche, A. C. Potter, A. Vishwanath, N. Y. Yao, and C. Monroe, "Observation of a discrete time crystal," *Nature*, vol. 543, pp. 217 EP –, Mar 2017. 72

[135] A. Chandran and S. L. Sondhi, "Interaction-stabilized steady states in the driven $O(N)$ model," *Phys. Rev. B*, vol. 93, p. 174305, May 2016. 72

[136] B. Huang, Y.-H. Wu, and W. V. Liu, "Clean Floquet time crystals: Models and realizations in cold atoms," *Phys. Rev. Lett.*, vol. 120, p. 110603, Mar 2018. 72, 76

[137] S. Pal, N. Nishad, T. S. Mahesh, and G. J. Sreejith, "Temporal order in periodically driven spins in star-shaped clusters," *Phys. Rev. Lett.*, vol. 120, p. 180602, May 2018. 72

[138] J. Rovny, R. L. Blum, and S. E. Barrett, "Observation of discrete-time-crystal signatures in an ordered dipolar many-body system," *Phys. Rev. Lett.*, vol. 120, p. 180603, May 2018. 72

[139] S. Autti, V. B. Eltsov, and G. E. Volovik, "Observation of a time quasicrystal and its transition to a superfluid time crystal," *Phys. Rev. Lett.*, vol. 120, p. 215301, May 2018. 72

[140] G. M. Koutentakis, S. I. Mistakidis, and P. Schmelcher, "Probing Ferromagnetic Order in Few-Fermion Correlated Spin-Flip Dynamics," *ArXiv e-prints*, Apr. 2018. 72

[141] R. E. Barfknecht, S. E. Rasmussen, A. Foerster, and N. T. Zinner, "Realizing a discrete time crystal in a few-body spin chain," 2018. 72

[142] K. Giergiel, A. Kosior, P. Hannaford, and K. Sacha, "Time crystals: analysis of experimental conditions," *ArXiv e-prints*, May 2018. 73, 76

[143] A. Kosior and K. Sacha, "Dynamical quantum phase transitions in discrete time crystals," *Phys. Rev. A*, vol. 97, p. 053621, May 2018. 73

[144] W. W. Ho, S. Choi, M. D. Lukin, and D. A. Abanin, "Critical time crystals in dipolar systems," *Phys. Rev. Lett.*, vol. 119, p. 010602, Jul 2017. 74

[145] A. Russomanno, F. Iemini, M. Dalmonte, and R. Fazio, "Floquet time crystal in the Lipkin-Meshkov-Glick model," *Phys. Rev. B*, vol. 95, p. 214307, Jun 2017. 74

[146] P. Wicke, S. Whitlock, and N. J. van Druten, "Controlling spin motion and interactions in a one-dimensional Bose gas," *ArXiv e-prints*, Oct. 2010. 76

[147] I. Brouzos and P. Schmelcher, "Construction of analytical many-body wave functions for correlated bosons in a harmonic trap," *Phys. Rev. Lett.*, vol. 108, p. 045301, Jan 2012. 81, 82, 89

[148] R. E. Barfknecht, A. S. Dehkharghani, A. Foerster, and N. T. Zinner, "Correlation properties of a three-body bosonic mixture in a harmonic trap," *Journal of Physics B: Atomic, Molecular and Optical Physics*, vol. 49, no. 13, p. 135301, 2016. 81

[149] I. S. Gradshteyn and I. M. Ryzhik, *Table of integrals, series, and products*. Elsevier/Academic Press, Amsterdam, seventh ed., 2007. Translated from the Russian, Translation edited and with a preface by Alan Jeffrey and Daniel Zwillinger, With one CD-ROM (Windows, Macintosh and UNIX). 82

[150] R. E. Barfknecht, I. Brouzos, and A. Foerster, "Contact and static structure factor for bosonic and fermionic mixtures," *Phys. Rev. A*, vol. 91, p. 043640, Apr 2015. 82, 88

[151] S. Tan, "Energetics of a strongly correlated fermi gas," *Annals of Physics*, vol. 323, no. 12, pp. 2952 – 2970, 2008. 87

[152] M. Olshanii and V. Dunjko, "Short-distance correlation properties of the lieb-liniger system and momentum distributions of trapped one-dimensional atomic gases," *Phys. Rev. Lett.*, vol. 91, p. 090401, Aug 2003. 87

[153] P. Vignolo and A. Minguzzi, "Universal contact for a tonks-girardeau gas at finite temperature," *Phys. Rev. Lett.*, vol. 110, p. 020403, Jan 2013. 87

[154] M. T. Batchelor, M. Bortz, X. W. Guan, and N. Oelkers, "Collective dispersion relations for the one-dimensional interacting two-component Bose and Fermi gases," *Journal of Statistical Mechanics: Theory and Experiment*, vol. 2006, no. 03, p. P03016, 2006. 93, 97

[155] P. Muruganandam and S. Adhikari, "Fortran programs for the time-dependent Gross–Pitaevskii equation in a fully anisotropic trap," *Computer Physics Communications*, vol. 180, no. 10, pp. 1888 – 1912, 2009. 94, 100, 109, 111

[156] I. Vidanović, N. J. van Druten, and M. Haque, "Spin modulation instabilities and phase separation dynamics in trapped two-component bose condensates," *New Journal of Physics*, vol. 15, no. 3, p. 035008, 2013. 94

[157] A. Kleine, C. Kollath, I. P. McCulloch, T. Giamarchi, and U. Schollwöck, "Excitations in two-component Bose gases," *New Journal of Physics*, vol. 10, no. 4, p. 045025, 2008. 99

[158] S. Choi, V. Dunjko, Z. D. Zhang, and M. Olshanii, "Monopole excitations of a harmonically trapped one-dimensional Bose gas from the ideal gas to the Tonks-Girardeau regime," *Phys. Rev. Lett.*, vol. 115, p. 115302, Sep 2015. 99

[159] C. Fort, F. S. Cataliotti, L. Fallani, F. Ferlaino, P. Maddaloni, and M. Inguscio, "Collective excitations of a trapped bose-einstein condensate in the presence of a 1d optical lattice," *Phys. Rev. Lett.*, vol. 90, p. 140405, Apr 2003. 99

[160] B. Fang, G. Carleo, A. Johnson, and I. Bouchoule, "Quench-induced breathing mode of one-dimensional Bose gases," *Phys. Rev. Lett.*, vol. 113, p. 035301, Jul 2014. 99

[161] W. Press, S. Teukolsky, W. Vetterling, and B. Flannery, *Numerical Recipes 3rd Edition: The Art of Scientific Computing*. Cambridge University Press, 2007. 109

[162] S. E. Koonin and D. C. Meredith, *Computational Physics: Fortran version*. Addison-Wesley - Reading, 1990. 110

[163] M. L. Wall and L. D. Carr, "Out-of-equilibrium dynamics with matrix product states," *New Journal of Physics*, vol. 14, no. 12, p. 125015, 2012. 112